

**Nd:GLASS LASER-INDUCED DAMAGE TO
THIN FILMS, TWO-PHOTON EXCITED
FLUORESCENCE AND PLASMA STUDIES**

P. RADHAKRISHNAN

**THESIS SUBMITTED
TO
THE UNIVERSITY OF COCHIN
IN PARTIAL FULFILMENT OF THE REQUIREMENTS
FOR THE DEGREE OF
DOCTOR OF PHILOSOPHY**

**LASER DIVISION, DEPARTMENT OF PHYSICS
UNIVERSITY OF COCHIN, COCHIN-682 022**

1985

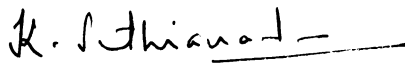
DEDICATED TO

MY LOVING PARENTS & SISTERS

CERTIFICATE

Certified that this thesis is the report of the original work carried out by Mr.P.Radhakrishnan in the Department of Physics, University of Cochin, under my guidance and supervision and that no part thereof has been included in any other thesis submitted previously for the award of any degree.

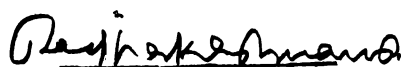
Cochin 682022
April 30, 1985


Dr.K.Sathianandan
Professor of Physics
(Supervising Teacher)

DECLARATION

Certified that the work presented in this thesis is based on the original work done by me under the guidance of Dr.K.Sathianandan, Professor, Department of Physics, University of Cochin, and has not been included in any other thesis submitted previously for the award of any degree.

Cochin 682022
April 30, 1985


P.Radhakrishnan.

ACKNOWLEDGEMENTS

I have great pleasure in expressing my deep sense of gratitude to Prof.K.Sathianandan for his profound interest, constant encouragement and able guidance throughout the period of my research. I am also grateful to him for providing the latest facilities for carrying out investigations in the field of lasers.

I am extremely grateful to all the faculty members of the Physics Department, Cochin University, especially to Dr.V.P.N.Nampoori for helpful discussions at various stages. I also extend my sincere thanks to the members of the library, laboratory and non-teaching staff of the Department of Physics for their kind hearted co-operation during the course of this work.

I express my sincere gratitude to the Principal, Prof.R.V.Kilikar, and to the Head of the Department of Physics, Prof.P.S.Radhakrishnan, of The Cochin College for extending all possible help and encouragement. I am also thankful to the faculty members of the Department of Physics and my well-wisher at The Cochin College for their keen interest in my research work.

I owe a lot to all my colleagues and friends in the laser division, thin film division and other laboratories of the Department of Physics, Cochin University, particularly to Dr.N.Subhash and Mr.T.M.Abdul Rasheed, for their invaluable assistance rendered during the course of this work.

Let me take this opportunity to acknowledge the assistance given by the staff of the University Services and Instrumentation Centre of the Cochin University in the fabrication work.

Special thanks are due to Mr.K.P.Sasidharan for the neat typing of the manuscript. Finally, I thank the DAE for providing a research fellowship during the initial stages of my work.

PREFACE

Laser-induced damage is the principal limiting constraint in the design and operation of high-power laser systems used in fusion and other high-energy laser applications. Therefore, an understanding of the mechanisms which cause the radiation damage to the components employed in building a laser and a knowledge of the damage threshold of these materials are of great importance in designing a laser system and to operate it without appreciable degradation in performance. This thesis, even though covers three distinct problems for investigations using a dye Q-switched multimode Nd:glass laser operating at 1062 nm and emitting 25 ns (FWHM) pulses, lays its main thrust on damage threshold studies on thin films. Using the same glass laser two-photon excited fluorescence in rhodamine 6G and generation and characterisation of a carbon plasma have also been carried out.

The thesis is presented in seven chapters. The first chapter contains a detailed description of the fabrication and output characteristics of the Nd:glass laser which operates both in the conventional and dye Q-switched modes.

Chapter 2 gives a detailed account of the damage mechanisms in materials with particular emphasis on thin films. The first part of the chapter contains the theoretical aspects of laser damage to dielectrics covering the three distinct paths of avalanche ionization, multiphoton ionization and impurity induced damage. The latter part of this chapter, after a brief analysis of the damage in metals, discusses the characteristic features of transparent polymer materials and the various damage mechanisms in them. Of the various mechanisms of laser damage to transparent polymers, a brief outline of a mechanism associated with the viscoelastic properties of these materials has also been given.

The method of preparation, characteristics and laser-induced damage threshold measurement of some transparent-conductive coatings form the subject matter of Chapter 3. The films studied are tin oxide prepared by chemical vapour deposition and spray pyrolysis and indium tin oxide prepared by reactive rf sputtering.

Chapter 4 consists of three sections. The first section deals with the method of preparation and the damage threshold determination of polyacrylonitrile (PAN) films. In

the subsequent sections, the damage threshold measurement of dielectric and metallic coatings with and without an undercoat of PAN is given.

In Chapter 5 the two-photon excited fluorescence studies on rhodamine 6G in methanol at five different concentrations have been reported. A comparative study between one photon and TPE fluorescence has also been presented.

Chapter 6 discusses the experimental layout, production, detection and characterisation of a carbon plasma carried out using the Q-switched Nd:glass laser. Details regarding the fabrication of a vacuum system and a plasma chamber have also been given. Analysis of the laser-produced plasma made using a biased probe has also been presented.

The concluding chapter provides a summary and evaluation of the investigations presented in the earlier chapters. An assessment of the major results achieved during the course of the present studies is also made.

Part of the investigations presented in the thesis has been published/communicated in the form of following papers:

1. Concentration dependence of two-photon excited fluorescence emission in rhodamine 6G,
P.Radhakrishnan, T.M.Abdul Rasheed,
V.P.N.Nampoori and K.Sathianandan, Lasers and applications, ed.H.D.Bist and J.S.Goela,
Tata McGraw-Hill, New Delhi ,p.381 (1984).
2. Laser-induced damage study of polyacrylonitrile films,
P.Radhakrishnan, K.Sathianandan and
C.P.G.Vallabhan, Bulletin of electrochemistry
(in press).
3. Laser-induced damage to spray pyrolysis deposited transparent conducting films,
P.Radhakrishnan, K.Sathianandan and N.Subhash,
(communicated to Journal of Applied Physics).

CONTENTS

		<u>Page</u>
	PREFACE i
	LIST OF FIGURES viii
	LIST OF TABLES xi
Chapter 1	FABRICATION DETAILS AND PERFORMANCE CHARACTERISTICS OF A DYE Q-SWITCHED Nd:GLASS LASER	
1.10	Introduction	.. 1
1.20	Lasing considerations and the Nd:glass laser rod	.. 6
1.30	Glass laser oscillator	.. 8
1.31	Pumping chamber	.. 11
1.32	Laser support table and mirror mounts	.. 15
1.33	Flashlamp drive circuit	.. 17
1.40	Alignment and performance of the laser	.. 26
1.41	Divergence measurement	.. 29
1.50	Dye Q-switched glass laser	.. 29
1.51	Kodak 14015 dye	.. 34
1.60	Q-switched laser performance	.. 35
1.70	Results	.. 36
Chapter 2	LASER DAMAGE MECHANISMS	
2.10	Introduction	.. 42
2.20	Avalanche ionization	.. 47
2.30	Multiphoton ionization	.. 49
2.40	Impurity dominated breakdown	.. 50
2.50	Laser-induced damage to metals	.. 59
2.60	Laser damage to transparent polymers	.. 60

Page

Chapter 3	LASER-INDUCED DAMAGE STUDIES ON TRANSPARENT-CONDUCTIVE COATINGS		
3.10	Introduction	..	70
3.20	Structural, electrical and optical properties	..	73
3.30	Preparation of tin oxide films by chemical vapour deposition method	..	75
3.40	Preparation of tin oxide films by spray pyrolysis method	..	76
3.50	Preparation of indium tin oxide films by rf sputtering method	..	78
3.60	Damage threshold measurement	..	79
3.70	Measurement of refractive index, thickness, absorptance and sheet resistance	..	83
3.80	Results and discussion	..	92
Chapter 4	DAMAGE THRESHOLD MEASUREMENTS ON THIN FILMS OF POLYACRILONITRILE (PAN), DIELECTRIC AND METALLIC FILMS WITH AND WITHOUT AN UNDERCOAT OF PAN		
Section A	Damage Threshold Measurement on Polyacrilonitrile		
4.10	Introduction	..	102
4.11	Preparation of PAN films	..	104
4.12	Damage threshold measurement	..	107
4.13	Results and discussion	..	107
Section B	Damage Threshold Measurement on Di- electric Films with and without an Undercoat of PAN		
4.20	Introduction	..	110
4.21	Preparation of magnesium fluoride and zinc sulphide films	..	114
4.22	Damage threshold measurement	..	116
4.23	Results and discussion	..	117

Section C	Laser-Induced Damage Studies on Gold Coatings with and without an Undercoat of PAN		
4.30	Introduction	..	120
4.31	Damage threshold measurement of Au films	..	123
4.32	Results and discussion	..	123
Chapter 5	TWO-PHOTON EXCITED FLUORESCENCE IN RHODAMINE 6G		
5.10	Introduction	..	129
5.20	Absorption cross section	..	133
5.30	Rhodamine 6G	..	136
5.40	Experimental details	..	139
5.50	One-photon excited fluorescence in rhodamine 6G	..	142
5.60	Results and discussion	..	144
Chapter 6	PRODUCTION, DETECTION AND CHARACTERIZATION OF A LASER-PRODUCED PLASMA		
6.10	Introduction	..	153
6.20	Fabrication of a plasma chamber	..	155
6.30	Fabrication of a vacuum system	..	156
6.40	Plasma production and detection	..	157
6.50	Results	..	162
Chapter 7	CONCLUSIONS	..	167

LIST OF FIGURES

<u>Figure No.</u>	<u>Caption</u>	<u>Page</u>
1.1	Partial energy level diagram of Nd ³⁺ in glass ..	9
1.2A	Conventional pulsed glass laser layout ..	9
1.2B	Conventional mode glass laser resonator ..	13
1.2C	Nd:glass laser system ..	14
1.3A	Cross sectional view of the pumping chamber ..	16
1.3B	The pumping chamber with the flashlamps and the laser rod ..	13
1.4	Mirror mount ..	16
1.5A	Flashlamp drive circuit along with the trigger circuit ..	22
1.5B	Rate generator circuit ..	25
1.6	Flashlamp circuit output pulse shape ..	28
1.7	Set-up for laser alignment ..	27
1.8	Laser energy and pulse width measurement set-up ..	27
1.9	Conventional mode laser output structure ..	28
1.10	Dye Q-switched laser layout ..	31
1.11	Nonlinear transmission of a saturable absorber versus light intensity ..	31
1.12	Molecular formula and structural configuration of Kodak 14015 dye ...	31
1.13A&B	Dye Q-switched output pulses ..	37

<u>Figure No.</u>	<u>Caption</u>	<u>Page</u>
3.1A	Schematic diagram of laser-induced damage threshold measurement	.. 80
3.1B	Laser-induced damage threshold measurement set-up	.. 81
3.2A	Damaged sites on indium tin oxide and tin oxide	.. 84
3.2B	Damaged sites on tin oxide	.. 84
3.3	Experimental set-up to measure refractive index	.. 85
3.4A	Illustration of fringe shift and air wedge	.. 91
3.4B	Experimental set-up to determine the thickness of films	.. 91
3.5A	Absorption spectrum of indium tin oxide	.. 93
3.5B	Absorption spectrum of tin oxide prepared by CVD method	.. 93
3.5C	Absorption spectrum of tin oxide prepared by SPD method	.. 94
4.1	Variation of damage threshold with thickness for MgF ₂ films	.. 118
5.1	Simplified electronic level scheme of rhodamine 6G	.. 138
5.2	Absorption spectrum of rhodamine 6G	.. 138
5.3	Structural formula of rhodamine 6G	.. 138
5.4	Two-photon excited fluorescence--experimental set-up	.. 141
5.5	Two-photon excited fluorescence spectra	.. 141
5.6	One-photon fluorescence--experimental set-up	.. 143

<u>Figure No.</u>	<u>Caption</u>	<u>Page</u>
5.7A,B&C	One-photon fluorescence spectra	.. 143 & 145
5.8	Variation of λ_{\max} with concentration	.. 147
5.9	Plot of log fluorescence intensity vs. log incident intensity	.. 147
6.1	Electrical circuit to detect the plasma	.. 158
6.2A	Schematic diagram for the plasma experiment	.. 158
6.2B	Experimental layout for the plasma experiment..	160
6.3	Current collected by the probe as a function of time	.. 160
6.4	Plot of input laser energy vs. flow velocity	.. 161
6.5	Probe characteristics	.. 164

LIST OF TABLES

<u>Table No.</u>	<u>Caption</u>	<u>Page</u>
1.1	Lasing properties of the laser glass rod LSG -91H	.. 10
1.2A	Optimisation of flashlamp discharge circuit parameters	.. 20
1.2B	-do-	.. 21
3.1	Comparison of the film characteristics of transparent conducting coatings	.. 95
4.1	Threshold values of PAN films	.. 108
4.2A	Threshold values of MgF ₂ and ZnS	.. 119
4.2B	Threshold values of MgF ₂ with an undercoat of PAN	.. 121
4.3	Threshold values of gold coatings with and without an undercoat of PAN	.. 124

Chapter 1

FABRICATION DETAILS AND PERFORMANCE CHARACTERISTICS OF A DYE Q-SWITCHED Nd:GLASS LASER

1.10 Introduction

Glass lasers currently provide the most intense radiant laser sources¹ and are widely used in recent times for laser fusion research programmes. The ions which are made to lase in glass include Nd³⁺, Yb³⁺, Er³⁺, Ho³⁺, Tm³⁺ and Gd³⁺. Of these, trivalent neodymium is perhaps the most important because it can be operated at room temperature with high efficiency². Although neodymium is made to lase in a variety of glasses, the combined requirements of a relatively long fluorescent lifetime, high fluorescent efficiency and high durability are best provided by a glass with an alkali-alkaline earth silicate base³. Laser emission from neodymium doped in barium crown glass is usually at 1060 nm. This was first demonstrated by Snitzer⁴ in 1961. Lasing from neodymium at 1370 nm was achieved by using a dichroic reflector (frequency selector) that has a high reflectivity at 1370 nm but relatively translucent at

1060 nm⁵. Emission solely at 920 nm requires not only an appropriate dichroic reflector but also reduced temperature (77°K)⁶. For operation at different wavelengths many new glass laser systems have been developed using various dopant-host combinations. Snitzer¹ gives a detailed review of the various ions that have been made to lase in different types of glasses and their characteristics.

Typical stimulated emission from a solid state laser occurs as a rapid succession of short, low energy bursts or as a continuous energy flow. Production of high intensity, short duration pulses by Q-switching⁷⁻¹⁰ was the next major step in the development of solid-state lasers. The population is inverted to a very high value when the cavity Q is low. When the population reaches its peak value, the Q of the cavity is restored back to its normal high value. The oscillations are now built up and a high intensity, short duration pulse is emitted. The pulse width depends on the type of Q-switching employed and the cavity length¹¹. Commonly adopted Q-switching techniques are rotating prism, saturable absorbers and electro-optic (E-O) devices.

The rotating prism/mirror technique for the generation of Q-switched pulses involves rotating one of the

two resonant cavity reflectors so that parallelism of the reflectors occurs only for a brief instant of time¹²⁻¹⁵. Pulses upto 15 ns were obtained using this technique¹⁵.

Passive Q-switches using bleachable absorber dyes have been of intense interest since their successful operation in 1964^{16,17}. The dye Q-switch consists of a dye cell which is placed inside the optical resonator between the laser medium and the rear mirror. The absorption of the sample dye varies with the intensity of light incident on it. The laser will start oscillating only when the incident light intensity is sufficient to bleach the dye. For Q-switching ruby lasers, cryptocyanine and pthalocyanine dyes in methanol are used while for Nd:glass lasers Eastman Kodak (9860, 9740 or 14015) dyes in 1,2 dichloroethane are used. The pulse width obtained depends on the particular dye, the solvent and its concentration and is usually in the range 20-250 ns.

The electro-optic Q-switch consists of an E-O element, a crystal or a liquid, which becomes birefringent¹⁸ under the influence of an external field. In the former case it is called a Pockels cell and in the latter a Kerr cell. Pockels cells, which require a lower voltage than Kerr cells, are the

most widely used active devices for Q-switching pulsed lasers. Q-switches are classified into two types: one in which electric field is applied along the direction of the optical beam and the other where the electric field is perpendicular to the direction of the optical beam. The voltage applied on the crystal is determined by the type of crystal used, the wavelength of operation and the operating mode^{19,20}. Crystals of potassium deuterated phosphate (KD*P) and its isomorphs belonging to the point group symmetry $\bar{4}2m$ are commonly used as Q-switches with longitudinal field²¹⁻²³. As these crystals are hygroscopic, they are usually operated in index-matching fluid-filled cells²¹. Transmission losses can be reduced by the use of antireflection coatings on the cell windows. In the case of Pockels cell with transverse fields, a proper choice of crystal geometry permits the use of a lower voltage as compared to longitudinally applied fields. When using transverse fields, lithium niobate crystals are preferred because they are not hygroscopic and can be operated with the light propagation along the optic-axis^{24,25}. The major drawback of lithium niobate is that it is not suitable for high-power-density applications. The peak optical power handling capacity of the crystal is around 10-50 MW/cm² while those of the KD*P family is more than 200 MW/cm². Pulse widths variable upto 600 ns have been

obtained from E-O Q-switched lasers using feedback loops to control the switching of a Pockels cell²⁶.

Ultra short pulses in the picosecond regime can be produced by the mode-locking technique^{27,28}. In this process the longitudinal modes emitted by a laser are forced to maintain a fixed phase relationship to each other and the output as a function of time will vary in a well-defined manner. Mode locked lasers can have high peak powers, because the power contained in the entire output of the uncoupled laser is now contained within the more intense ultrafast pulses. Mode locking is achieved experimentally by placing inside the laser cavity either an externally driven phase modulator or a passive device which exhibits saturable absorption. By mode-locking a Nd:glass laser using a few mm thick dye cell, pulse trains of about 50-200 ns wide containing 5-20 ps pulses were produced²⁹.

Using optical gates external to the oscillator, a simple pulse from the mode locked train can be selected out for further amplification in laser amplifier chains to very high power levels, typically, a few hundred terawatts. Similar systems are being used at the Lawrence Livermore Laboratory, California and other places for fusion experiments and other laser interaction studies³⁰.

The major disadvantage of a glass laser is the low thermal conductivity of the laser rod. This imposes limitations on the diameter that can be used in continuous wave (CW) operation and in high repetition rate applications. The low thermal conductivity leads to cooling difficulties in high power devices. However, CW laser action at 1060 nm has been obtained at room temperature in barium crown glass^{31,32} containing 6.25 wt % of Nd_2O_3 .

In this chapter the fabrication details and performance of a Nd:glass laser is given. In relation to the possible use of this laser for research, it was felt necessary to operate the laser in different modes: conventional, E-O Q-switched and dye Q-switched, so that system flexibility and possibility for modification and expansion are possible for any individual investigator. The present laser is thus built to operate in all these modes; but the experiments reported in the subsequent chapters have been carried out using the laser in the dye Q-switched mode.

1.20 Lasing considerations and the Nd:glass laser rod

Fig.1.1 shows the energy levels involved in laser action in a typical Nd:glass rod. The Nd^{3+} ion in glass

represents a four-level system with laser action taking place at 1060 nm between the lower lying levels of ${}^4F_{3/2}$ and that of ${}^4I_{11/2}$. The lifetime of the upper laser level varies in the range 40-900 μ s depending upon the dopant, the percent of doping and the host material¹. The ${}^4I_{11/2}$ group of levels empties spontaneously by radiationless phonon transition to the ${}^4I_{9/2}$ ground state.

The threshold condition for laser oscillation, assuming a Lorentzian shape for the atomic line, is given by³³

$$n_2 - n_1 \frac{g_2}{g_1} > 4\pi^2 \nu_0^2 \frac{t_{21}}{t_c} c^3 \Delta \nu \quad (1.1)$$

where $\Delta \nu$ is the atomic line width at FWHM. n_1 and n_2 are the population of the lower and upper laser levels and g_1 and g_2 are their degeneracies. ν_0 is the frequency corresponding to the centre of the atomic transition, t_{21} is the lifetime of the upper laser level, t_c is the decay time constant of photons inside the resonator and c is the velocity of light in the medium. Using this relation the threshold population inversion (n_t) can be calculated. If n_i is the initial inversion (atoms/cm³) obtained by pumping the laser rod and V is the laser rod volume (cm³), then the

total energy of the emitted pulse is $n_i h\nu V$, since for an ideal four-level system, $n_1 \approx 0$. This equation enables one to approximately determine the rod volume required for any output energy. In Q-switched lasers, the initial inversion may go up to approximately $5 n_t$ and hence, this value has to be taken for calculation purposes. In the case of a glass rod, thermal conductivity considerations imposes limitations on its diameter. Taking these factors into account, a 152.4 mm long, 6 mm diameter silicate glass laser rod (LSG-91H) manufactured by Hoya Electronics Limited, Japan was chosen for the present laser system. The physical and optical properties of this glass laser rod are given in table 1.1. The threshold population inversion without Q-switch was calculated to be 3×10^{17} atoms/cm³ approximately. The end faces of the laser rod are plane with a surface accuracy of $\lambda/20$ at 1060 nm and the parallelism between the faces is less than 5 arc secs. These faces were antireflection (AR) coated for 1060 nm to facilitate the use of the same rod in different configurations.

1.30 Glass laser oscillator

The laser system is shown in fig.1.2A. The laser rod, which is optically pumped in a pumping chamber using xenon flashlamps, is placed between two dielectric coated

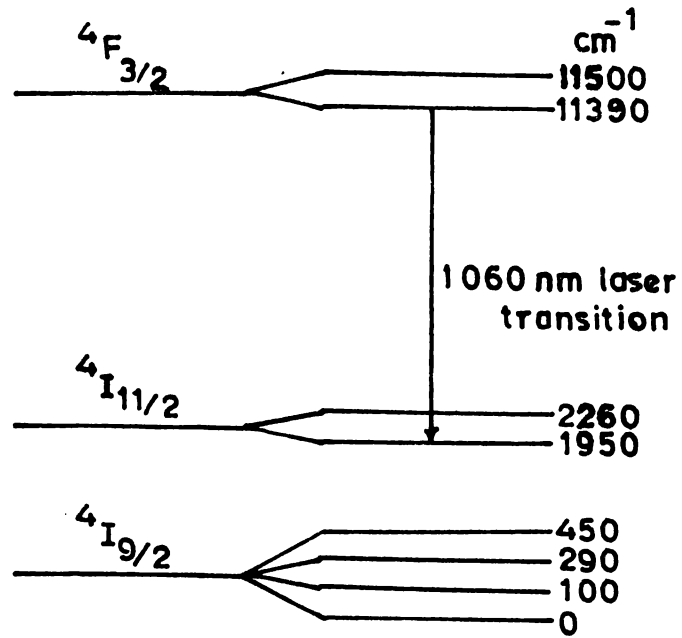


Fig.1.1 Partial energy level diagram of Nd^{3+} in glass.

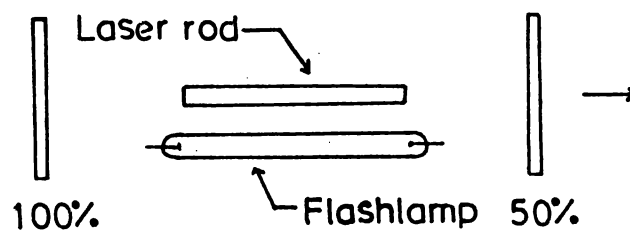


Fig.1.2A Conventional pulsed glass laser layout.

Table 1.1

Lasing properties : Silicate laser glass LSG-91H

Nd ₂ O ₃ (Wt. %)	: 3.1
Nd ³⁺ concentration (10 ²⁰ ions/cm ³)	: 3.04
Cross section for stimulated emission (10 ⁻²⁰ cm ²)	2.7
Life time (μ sec)	: 300
Specific gain (cm ⁻¹ /J/cm ³)	: 0.133
Fluorescence half-line width at 290°K(A°)	: 252
Centre lasing wavelength (μ)	: 1.062
Loss coefficient at 1.055 μ (m ⁻¹)	: 0.1 (1.062 μ)
Relative scattering intensity (6328 A°)	: 1
Slope efficiency (%) (Rod 10 dia.160mm)(R=80%)	: 1.15
Lasing threshold input energy (J) Rod 10 dia. 160 mm, R=80%	: 52
Relative figure of merit σ/n ₂	: 1
Laser damage threshold at 30 nsec pulse (J/cm ²)	: 400 internal : 25 surface

Other properties

Non linear refractive index coefficient n ₂ at peak λ (x 10 ⁻³ esu)	: 1.43
Refractive index at 1.062 μ	: 1.5498
Yield point	: 505°C
Thermal expansion coefficient (100-300°C) (10 ⁻⁷ /°C)	: 105
Thermal conductivity (25°C)(K cal/m.h.°C)	: 0.89
Specific heat (Cal/g.°C)	: 0.15 at 50°C
Density (g/cm ³)	: 2.81
Stress optical coefficient (nm/cm/kg cm ²)	: 2.16

mirrors of which one of them is 100% reflecting while the other is partially reflecting. Xenon is generally chosen as the gas fill for flashlamps because it yields a higher radiation output for a given electrical input energy than other gases. Moreover, for pumping Nd:glass rods xenon filled flashlamps are always used because its emission has a better match with the absorption spectrum of Nd³⁺ ions in glass. The mirrors (99.95% and 50% reflecting) used in the present system (1 inch diameter) were supplied by M/s.Laser Optics, USA. These dielectric coated mirrors had a surface accuracy of $\lambda/20$ and were narrow band coated for 1060 nm. For the partially reflecting mirror, the other face was AR coated for 1060 nm. The mirrors were fitted on mirror mounts specially designed for this purpose. Even though the system developed (figs.1.2B and 1.2C) had provision for operation upto 10 ppm the laser was usually operated in single shot or at low repetition rates (1-2 ppm), hence no cooling jackets were provided. In this mode of operation the output pulse width of the laser depends linearly on the flashlamp pulse duration.

1.31 Pumping chamber

The efficiency in the transfer of radiation from the lamp to the laser material determines to a large extent

the overall efficiency of the laser system. The pump cavity, besides providing good coupling between the lamp and the absorbing active material, is also responsible for the pump density distribution in the laser element which influences the uniformity, divergence and optical distortions of the output beam. Moreover, when high output energies are required or when the laser has to be operated in the Q-switched mode, where the cavity losses are more, more flashlamps are to be used so that one can safely increase the input energy into the system. Taking all these factors into consideration, a double circular pumping chamber which can incorporate two flashlamps was built. The simple closed-coupled double circular cavity (figs.1.3A and 1.3B) has the following dimensions:-

Length of the cavity	= 148 mm
Diameter of the circular reflector	= 30 mm
Separation between lamps	= 20 mm
Distance between the centres of the circular reflector	= 10 mm

The pumping chamber was machined out of extruded aluminium rod. The rod was cut and machined to size and



Fig.1.2B Conventional mode glass laser resonator.

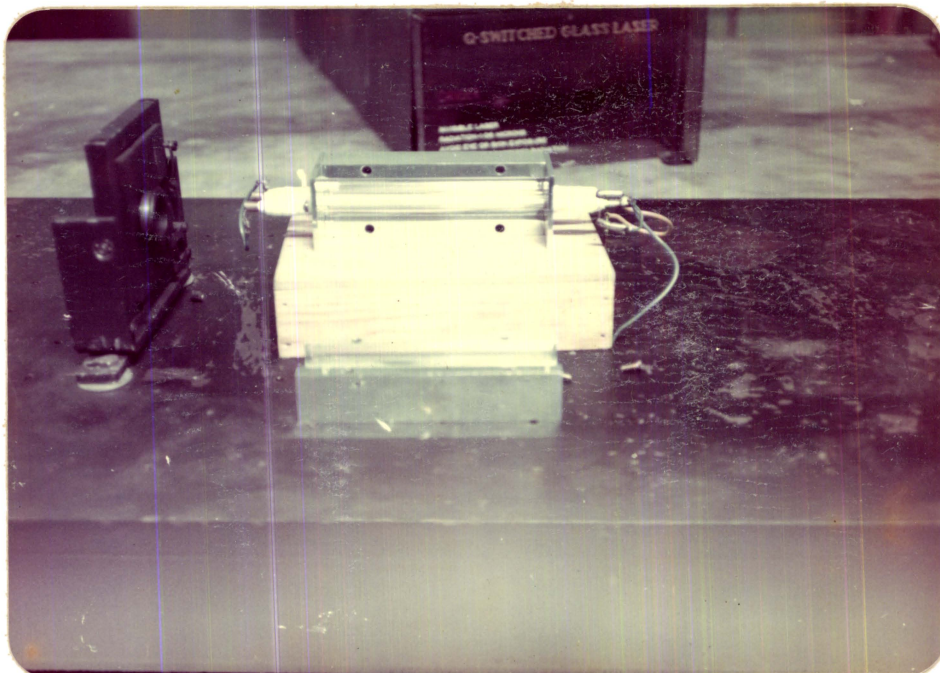


Fig.1.3B The pumping chamber with the flashlamps and the laser rod.



Fig.1.2C Nd:glass laser system.

bolted together. The circular surfaces were made by drilling two 30 mm diameter holes through the 148 mm length block. The inside portion was then finely polished and buffed. The side plates were 4 mm thick and had holes for mounting the flashlamps and the laser rod. For optimum matching with the laser rod the xenon flashlamps had an arc length of 152.4 mm and inner diameter of 6 mm (Model 6F6G ILC Technology, USA). The flashlamps had a quartz-envelope for absorbing the unwanted UV radiations. Care was taken to maximise the rod volume exposed to flashlamp radiation. For maximum pumping efficiency, the centres of the lamp and the rod should be equally separated from the centre of the circular reflector throughout its length. The radiation emanating from the lamp falls on the rod directly or after reflections at the chamber surfaces.

1.32 Laser support table and mirror mounts

A mild steel table (100 cm x 50 cm with a 2.5 cm thick top) forms the support structure for the laser system. The table top had $\frac{1}{4}$ inch tapped holes drilled at a separation of 2 inches on its entire surface. This enables rigid mounting of the optical components and other devices of the system. The support structure was fitted on 4 inch diameter anti-

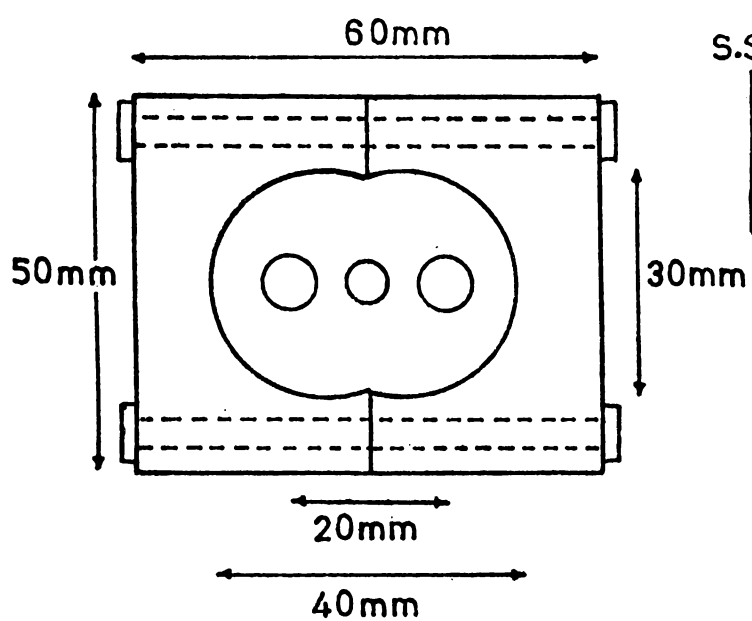


Fig.1.3A Cross sectional view of the pumping chamber.

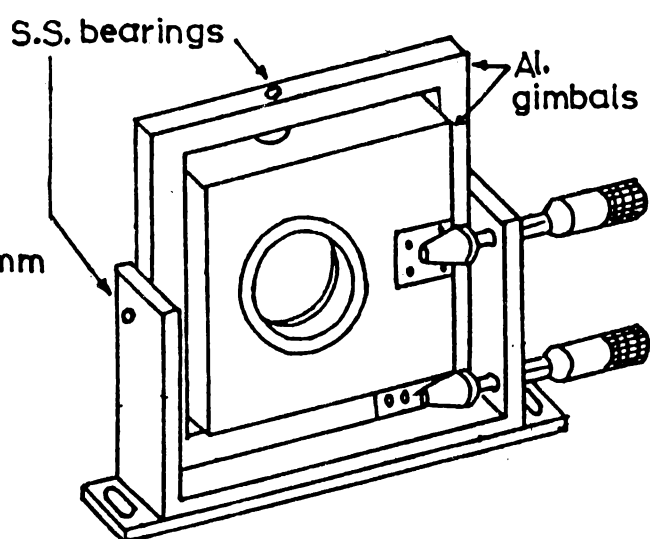


Fig.1.4 Mirror mount.

vibration mounts. The stability of the structure was found to be very good. The mirror mounts (fig.1.4) were similar in design to the one described by Pace and Atkinson³⁴. The gimbal type mount made for 1 inch laser mirrors provided independent orthogonal rotation about the vertical and horizontal axes. By using a conical adapter attached to the end of the two micrometer screws, good angular resolution was achieved.

1.33 Flashlamp drive circuit

The major components of a flashlamp drive circuit are a charging unit, a pulse-forming network (PFN) and a trigger circuit. The charging unit charges the PFN, which is basically an LC network, within a specified time depending on the desired repetition rate and the trigger circuit initiates the discharge of the stored energy into the flashlamps³⁵.

The capacitor-charging source consists of a transformer followed by a rectifier bridge and a current limiting element. The output of a 3 KV, 20 mA step-up transformer rectified by a full wave bridge and smoothed by a series of condensers (50 μ f 350 WV) provide the required DC voltage for the energy storage capacitor. The charging time of

the PFN is decided by the time constant (RC) of the circuit. Flashlamps are usually operated from a single or multiple-mesh LC network. The network stores the discharge energy and delivers it to the lamp in the desired current pulse shape. The lamp input energy, the pulse width and lamp dimensions will be fixed before designing the PFN. These parameters completely describe the network's capacitance and inductance as well as the charging voltage and peak current. For more strict control of the pulse duration and to create light pulses with flat tops, multiple-mesh networks are used.

Since the flashlamp does not follow the linear relationship of a constant resistance, the design procedure developed by Markienicz and Emmett³⁶ has been used for determining the inductance, capacitance and operating voltage for a given type of lamp, energy input, pulse duration and pulse shape factor. The following equations represent their analyses:-

$$C^3 = 2 E_0 \alpha^4 T^2 / K_0^4 \quad (1.2)$$

$$L = T^2 / C \quad (1.3)$$

$$V_0 = (2E_0 / C)^{1/2} \quad (1.4)$$

where C = capacity in farads, E_0 = stored energy in joules, T = one-third of the desired pulse width in seconds, k_0 = the impedance parameter in ohms $(\text{amp})^{\frac{1}{2}}$, L = inductance of the discharge circuit in henries, V_0 = initial voltage on capacitor bank and α = the damping parameter of the discharge circuit ($\alpha = 0.8$ for a critically damped discharge).

Once the desired energy input and pulse width are chosen, C , L and V_0 are found. The equation for the determination of other important parameters like peak current, peak power density, one shot explosion energy, inside wall load and expected life are given in tables 1.2A and 1.2B along with the optimised circuit parameters calculated for the two 6F6G flashlamps connected in series. Usually, in order to achieve a lifetime of 10^6 pulses³⁷, α has to be around 0.8 and E_0/E_x 0.197. As the pulse width determines the single shot explosion energy (E_x), E_0 and other parameters can be found for any desired pulse duration so as to obtain a life in excess of 10^6 shots. The pulse forming network consists of 2 meshes as shown in fig.1.5A. The limitations on the risetime of the current pulse determines the number of meshes (n) required for the network and is calculated using the relation

$$t_r = (LC)^{\frac{1}{2}}/n \quad (1.5)$$

Table 1.2A

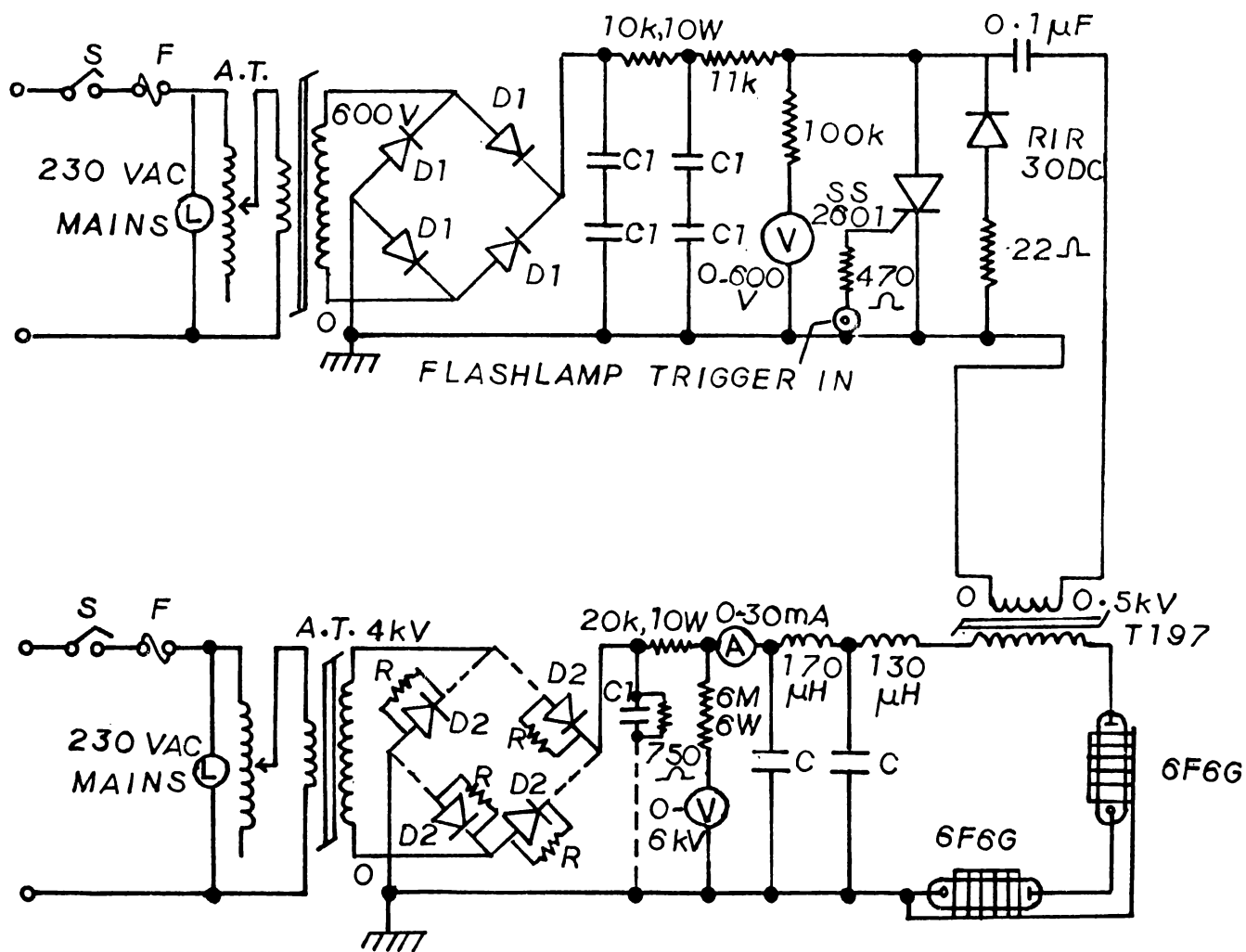
Optimisation of flashlamp discharge circuit
parameters

	Formula	Two lamps in series	Unit
Lamp designation	6F6G		
Bore diameter (d)	6		mm
Arc length (l)	6		inches
Gas	Xenon		
Pressure	450		torr
Inside wall area(s)	Πdl	57.4	sq.cm.
Cross section area (A)	$\Pi d^2/4$	0.28	sq.cm.
Volume (V)	$\Pi d^2 l/4$	8.62	c.c.
Lamp impedance (K_o)	$1.472 l/d$	65	ohm amp ^{1/2}
Input energy (E_o)	$K_o^4 C^3 / 2\alpha^4 T^2$	648.3	joules
Pulse width ($t=3T$)	$3 (LC)^{1/2}$	550	micro sec.
Capacitance (C)	$C^3 = \frac{2E_o \alpha^4 T^2}{K_o^4}$	100	MFD
Pulse Rep.rate (R)		0.1667 (10 ppm)	pulses/sec
Inductance (L)	T^2/C	336.1	μH
Voltage (V_o)	$(2E_o/C)^{1/2}$	3600	volts

Table 1.2B

Optimisation of flashlamp discharge circuit
parameters

	Formula	Two lamps in series	Unit
Circuit impedance (Z_o)	$(L/C)^{\frac{1}{2}}$	1.833	Ohms
Peak current (I_{peak})	$0.497V_o/Z_o$	976.15	Amps
Peak current density	I_{peak}/A	3486.25	Amps/cm ²
RMS current (I_{rms})	$0.707 I_{peak}$ $(3R LC)^{\frac{1}{2}}$	6.6	Amps
Init.Rate current rise	V_o/L	10.7	Amps/ μ s
Peak power (P_{peak})	$E_o/3T$	1178.7	kW
Average power (P_{av})	$E_o R$	108.04	Watts
Peak power density	P_{peak}/V	136.74	kW/cc
Ave. power density	P_{av}/V	12.54	Watts/cc
1 shot explosion energy(E_x)	$K_e T^2$	2978.8	Joules
Fraction of explosion energy (F)	E_o/E_x	0.217	
Expected life	$F^{-8.5}$	0.42×10^6	
Inside wall load	P_{av}/s	1.88	Watts/cm ²
Alpha (α)		0.8	
Pulse width at 70%	$2(LC)^{\frac{1}{2}}$	366.7	μ s



$R-1M, 1W$; $D1-BY127$; $D2-12SM1$; $C1-50\mu F, 350WV$; $C-50\mu F, 5kV$.
 A.T. - AUTO TRANSFORMER

Fig.1.5A Flashlamp drive circuit along with the trigger circuit.

The total inductance and capacitance value divided by n gives the L and C values per section. Inductance per mesh in this circuit was $168 \mu\text{H}$ and capacitance per mesh was $50 \mu\text{f}$. As the trigger transformer secondary winding having an inductance of $40 \mu\text{H}$ comes in the discharge circuit, the inductance required was only $128 \mu\text{H}$. These inductances were made by winding 18 SWG super enamelled copper wire. The number of turns N required for an air core inductor is given by

$$N^2 = L(9a + 10b)/a^2 \quad (1.6)$$

where L = inductance in μH , a and b are respectively the diameter and the length of the tube in inches. A PVC tube with $a = 1.87$ inches was used for making the inductance. The number of turns needed for $170 \mu\text{H}$ and $130 \mu\text{H}$ were 110 and 86 respectively and were wound over a length of 9 inch and 7 inch respectively. The energy storage capacitors were supplied by M/s. Madhav Capacitors, Pune. The saturated inductance ($40 \mu\text{H}$) of the secondary of the series trigger transformer (T 197 ILC model) provides the needed current limitation. When the SCR connected to the primary of T 197 fires, $1 \mu\text{f}$ (600 V) capacitor discharges and a trigger pulse of magnitude determined by the SCR voltage is generated.

T 197 steps up 500 V pulse to 18 kV. For reliable triggering of flashlamps a ground reference, usually in the form of a 20-30 SWG copper wire wound over the lamp envelope, is needed³⁸.

There are two methods of triggering the circuit³⁸ viz., series triggering and external triggering. The present design utilises series triggering scheme as it provides 100% trigger reliability even at low capacitor charging voltages³⁹. The repetition rate of the laser was controlled by a rate generator shown in fig.1.5B. The first NE 555 IC connected for astable operation functions as the rate generator with pulse repetition rates of 1,2,3,4,5 and 10 ppm. The second NE 555 timer operates in the monostable mode. The first monostable multi is triggered by the output of the rate generator or the voltage pulse generated by the microswitch (for single shot operation). The 10 K potentiometer facilitates independent pulse width control for the output pulse. The output of the second timer was used for triggering the SCR in the flashlamp discharge circuit.

Fig.1.6 shows the output pulse shape of the 2 flashlamps connected in series. This was recorded using a Hewlett Packard hp2-4207 photodiode with a 50 ohm load.

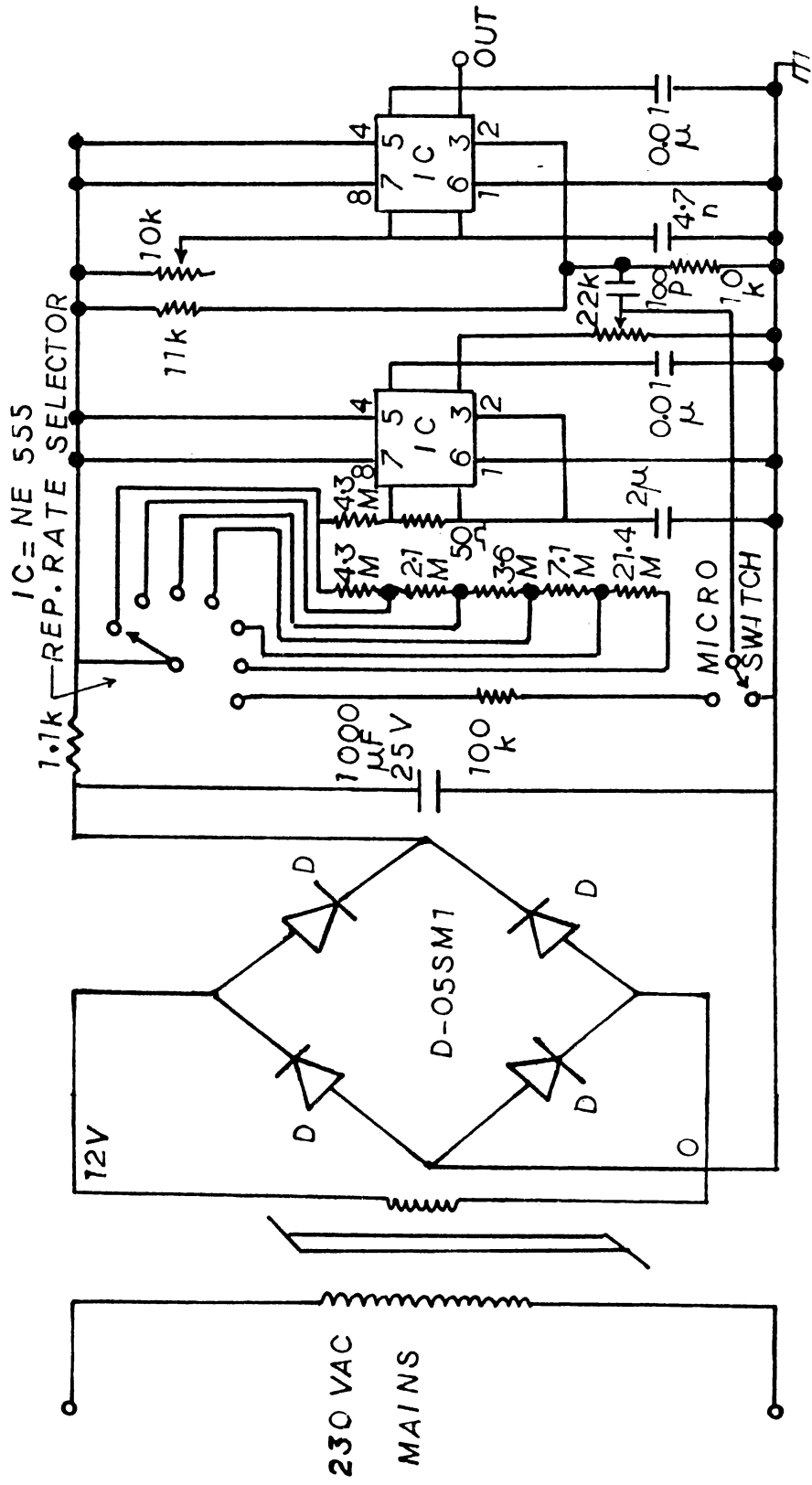


Fig.1.5B Rate generator circuit.

The pulse widths determined is 650 μ s at the base and 300 μ s at the 70% point. The risetime of the current pulse from 10% to 80% level for the PFN is about 100 μ s at 450 joules.

1.40 Alignment and performance of the laser

A high degree of accuracy in alignment of the cavity was needed as plane mirrors were used in the present system. Fig.1.7 shows the alignment technique employed in the present system. The He-Ne laser beams reflected by the rear and front mirrors were made to fall one over the other on the pinhole by slowly adjusting the micrometer screws on the mirror mounts. When the mirrors get exactly aligned the two spots coincide and a circular fringe pattern was observed with the pinhole at the centre.

The set-up for the measurement of the output energy and pulse width of the laser emission is shown in fig.1.8. The energy was measured using a Scientech 1 inch disc calorimeter and a photodiode, (Hewlett Packard model hp2-4207) with a bias voltage of 20 V and a terminal resistance of 50 ohms, was used to measure the pulse width.

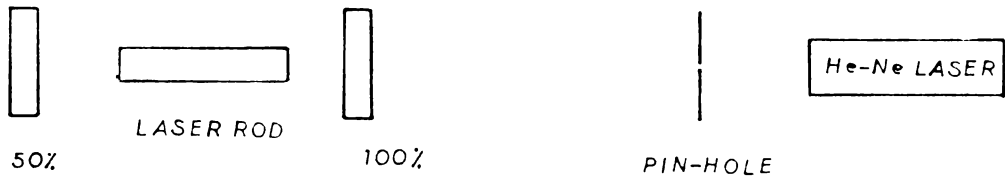


Fig.1.7 Set-up for laser alignment.

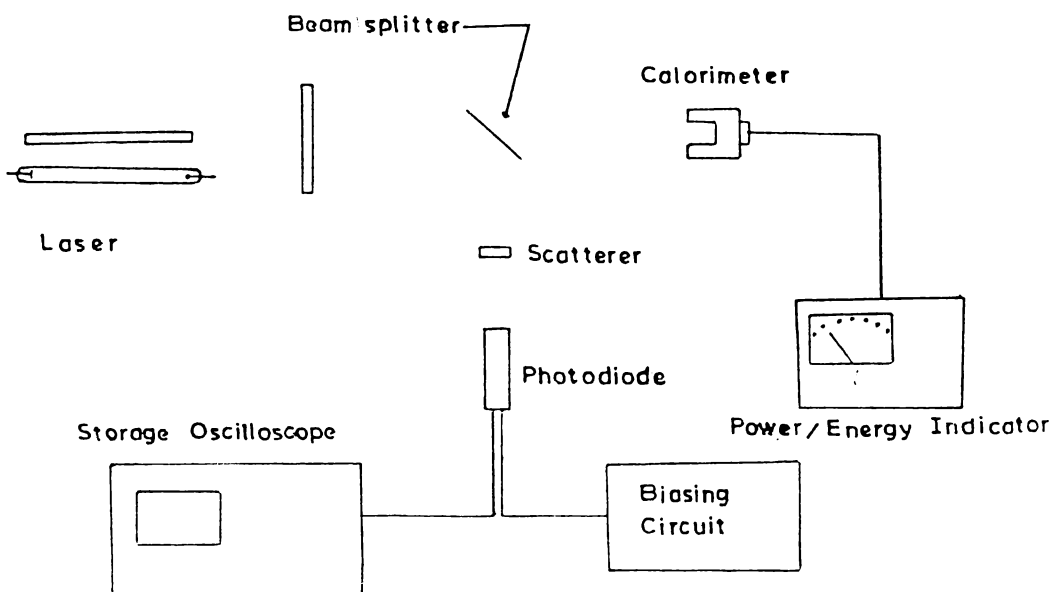


Fig.1.8 Laser energy and pulse width measurement set-up.

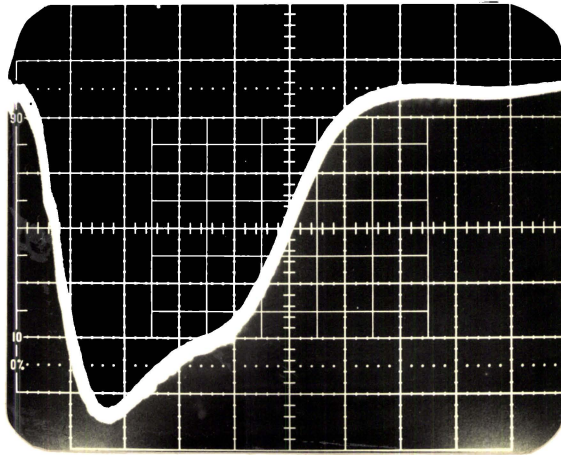


Fig.1.6 Flashlamp circuit output pulse shape with $E_{in} = 450$ J.
Sweep speed: 0.1 ms/div. Gain: 20 mV/div.

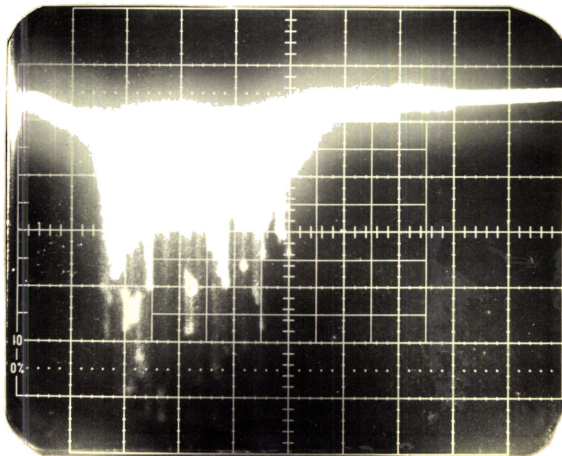


Fig.1.9 Conventional mode laser output structure with $E_{in} = 450$ J.
Sweep speed: 0.1 ms/div. Gain: 10 mV/div.

Typical trace of the pulse recorded with the laser operated in the pulsed (conventional) mode is shown in fig.1.9. The spiking behaviour exhibited is due to the relaxation oscillations taking place inside the cavity.

1.41 Divergence measurement

The divergence of the laser beam was measured by recording the burn patterns on a photographic film at the exit mirror and at a distance of 370 cm from the exit mirror. The beam diameters recorded had diameters of 6 mm and 8 mm at the two points of observations for an input energy of 400 joules. This gives a full angle divergence of 0.54 mrad.

1.50 Dye Q-switched glass laser

Passive Q-switches using organic dyes are of great importance because of its simplicity in design and operation^{16,17,40,41}. Another advantage is that the emission linewidth is very narrow ($0.02 \overset{\circ}{\text{Å}}$, typically). The dye Q-switched laser consists of a dye cell placed inside the optical resonator between the laser medium and the rear mirror as shown in fig.1.10. The dye initially absorbs the laser rod fluorescence emission to the degree

that the rear reflector is optically isolated from the remainder of the laser cavity. When the dye suddenly bleaches, the laser radiation can reach the rear reflector and the laser oscillation occurs. The laser Q-switch located inside the laser resonator, drastically changes the power and temporal characteristics of the beam obtained from the laser oscillator.

The generic name for the type of material which is used in the dye cell is saturable absorber. In these liquids the absorption coefficient decreases readily with increasing light intensity as shown in fig.1.11. Thus, the material becomes more transparent as the light becomes more intense. The increase in transparency of the dye is also frequently called "bleaching" of the dye. The decrease of the absorption coefficient for a saturable absorber or dye is related to the incident light intensity in the following way

$$\gamma = \frac{\gamma_0}{1+(I/I_s)} \quad (1.7)$$

where γ_0 is the absorption coefficient at zero intensity, and I_s is the saturation intensity, the intensity at which γ decreases by one half. The bleaching process

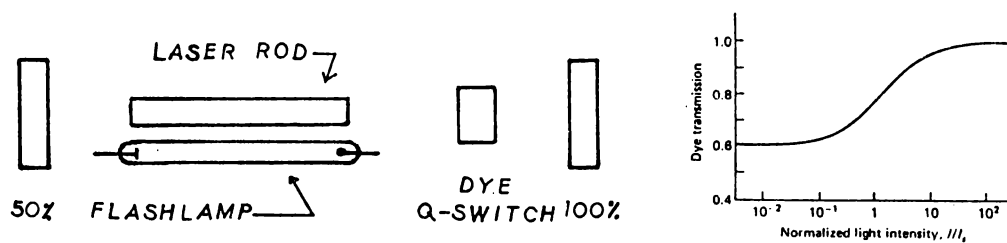


Fig.1.10 Dye Q-switched laser layout

Fig.1.1 Nonlinear transmission of a saturable absorber versus light intensity.

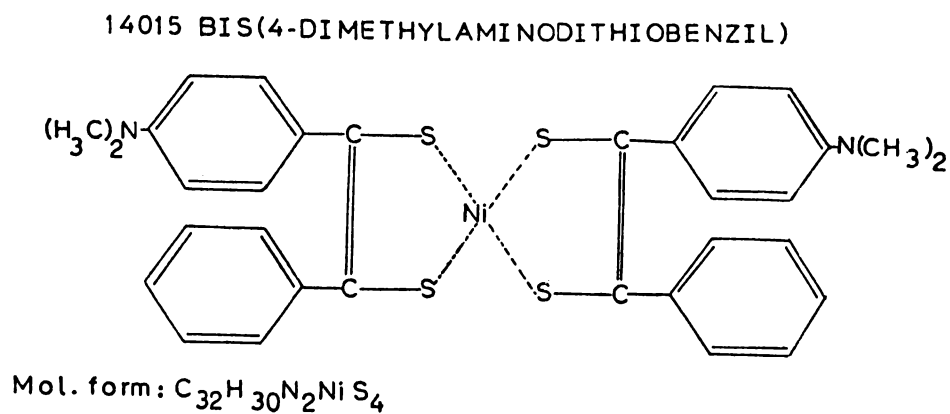


Fig.1.12 Molecular formula and structural configuration of Kodak 14015 dye.

in a saturable absorber is based on saturation of a spectral transition. The dye molecules in the solution absorb photons and are transferred to an excited state from which they return at the end of an average lifetime τ_s to the ground state. When the dye is inserted into the laser cavity, it will look opaque to the laser radiation until the photon flux is large enough to depopulate the ground level. If sufficient number of molecules are excited, the dye becomes completely transparent to the laser radiation. The saturation intensity I_s of an optically thin saturable absorber can be expressed as

$$I_s = h\nu/\sigma_s \tau_s \quad (1.8)$$

where σ_s is the cross section of the absorbing centres, and their effective lifetime in an excited state is τ_s . The response time of a saturable absorber to a step function in light intensity of amplitude I is given by

$$R = \frac{\tau_s}{1+(I/I_s)} \quad (1.9)$$

From these expressions, we see that if a saturable absorber is to be appreciably bleached at reasonable light levels

(between a few kilowatts and a few megawatts per square cm) and at the same time respond quickly, it must have a large cross section and a reasonably short lifetime. For a dye to be effective for Q-switching, the dye cross section σ_s must be much larger than the laser cross section.

Only a few dyes (Eastman Kodak 9860, 9740, 14015 and 14617) have been used with neodymium lasers for Q-switching. The solvents for these dyes are 1,2 dichloroethane, chlorobenzene, iodomethane and methyl sulphoxide. The solvent chosen determines the relaxation time of the dye solution. If the dye has a very short relaxation time, of the order of a few picoseconds, and can follow fast oscillations in the intensity, it will attempt to mode-lock the pulse instead of Q-switching it and produce pulses in the picosecond regime⁴². For efficient Q-switching the relaxation time of the dye has to be greater than or nearly equal to the cavity transit time. In this case, the output energy and pulse width is determined by the dye concentration and the path length of the Q-switch. Since CW pumped solid-state lasers will not generally be able to saturate or bleach the dye, the operation of the dye Q-switch is practically limited to pulsed solid-state lasers.

Passive dye Q-switches usually consist of two glass windows separated by an annular spacer. Common dye cells have path lengths ranging from 1 to 10 mm. The windows are anti-reflection coated to minimise losses. The optimum concentration of the dye will depend on the lamp input energy, resonator length and ambient temperature.

1.51 Kodak 14015 dye

Molecular formula and structural configuration of the Kodak 14015 dye is given in fig.1.12. This dye dissolved in 1,2 dichloroethane, is a photochemically stable transition metal complex for Q-switching Nd:glass lasers. This compound dissolved in the above solution shows a strong absorption band in the near IR. Exposure of the solution to intense near IR radiation for 2 days caused no measurable decrease in absorbance at 1060 nm⁴³. Eastman dye 14015 is much more stable than 9860 and 9740 and yields a longer performance life. This has the interesting property that the recovery time is drastically influenced by the solvent⁴⁴. It was found that the dye dissolved in 1,2 dichloroethane produces Q-switching, but it does not mode-lock the Nd:glass laser. This was attributed to the relatively long lifetime of the dye in its triplet state.

1.60 Q-switched laser performance

In the present system, a quartz cell polished to a high accuracy and having a dimension of 8 mm square is used to contain the Kodak 14015 dye dissolved in 1,2 dichloroethane. The dye cell was then inserted into the resonator and the laser system was aligned. The Nd:glass laser rod was pumped using xenon flashlamps. The laser output pulse shape was monitored with hp2-4207 photodiode coupled to a storage oscilloscope (Tektronix model 466 DM 44). The output energy was simultaneously measured using the Scientech 1 inch disc calorimeter (Model 38-0101).

Dye solution of a suitable concentration was taken in the quartz cell. The input energy into the flashlamp was slowly increased (from a low value) and lasing action was checked. At a particular input energy, threshold energy, determined by the concentration of the dye solution, the system started oscillating and a Q-switched pulse was obtained. If the dye concentration is lower than that corresponding to the threshold energy, bleaching action occurs at very low photon fluxes resulting in spiky output. In such cases, the concentration of

the dye solution had to be increased for observing Q-switched action. When the input energy was slightly increased from the threshold value, the output also increased and at a certain input energy the output was found to consist of two pulses. This is due to a second bleaching action that has taken place after the dye molecules had relaxed to their ground level. At still higher input energies, 3,4 etc. pulses were observed. In the case of a single pulse operation, maximum energy obtained in the present system was around 150 mJ and the output pulse was about 25 ns at FWHM (Figs. 1.13A and 1.13B).

1.70 Results

A laser system operating at 1062 nm was built using a 152.4 mm long, 6 mm diameter Nd:glass laser rod. The system was initially operated in the pulsed mode with a spiky output. The threshold input energy for this laser rod was found to be 110 joules for an output mirror reflectivity of 50%. For an input energy of 450 joules, output pulses of 2.2 joules in 400 μ s was obtained. The full angle divergence was measured to be around 0.54 mrad.

The laser was also operated in the dye Q-switched mode using Kodak 14015 dye dissolved in 1,2 dichloroethane. Output

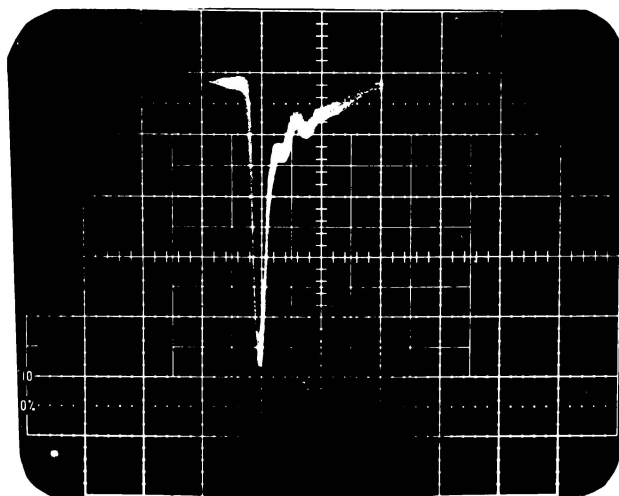


Fig.1.13A Dye Q-switched output pulse.
Sweep speed: 50 ns/div. Gain: 1V/div.

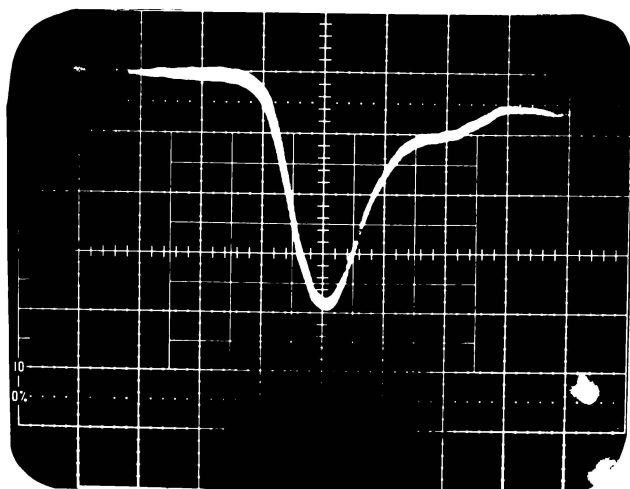


Fig.1.13B Dye Q-switched output pulse.
Sweep speed: 20 ns/div. Gain: 1V/div.

energy of around 150 mJ in 25 ns (FWHM) was obtained in this mode of operation which corresponds to a peak power of 6 MW for an input energy of 450 Joules. In both these configurations, no mode selection technique was utilised and hence the output structure was multimode.

REFERENCES

1. C.G.Young, Laser devices and applications, ed.I.P.Kaminow and A.E.Siegman, IEEE Press, IEEE Inc. New York (1973).
2. E.Snitzer, Proc.IEEE, 54, 1249 (1966).
3. E.Snitzer, Appl.Opt. 5, 1487 (1966).
4. E.Snitzer, Phys.Rev.Lett. 7, 444 (1961).
5. P.B.Mauer, Appl.Opt. 3, 153 (1963).
6. R.D.Maurer, Appl.Opt. 2, 87 (1963).
7. R.W.Hellwarth, Advances in quantum electronics, p.334, Columbia Univ. Press (1961).
8. F.J.Mc Clung and R.W.Hellwarth, J.Appl.Phys. 33, 828 (1962).
9. R.W.Hellwarth, Lasers, Vol.1, p.253, Marcel Dekker (1966).
10. W.G.Wagner and B.A.Lengyel, J.Appl.Phys. 34, 2040 (1962).
11. C.Bowness and C.F.Luck Jr., Laser technology and applications, ed.S.L.Marshall, Ch.IV, p.62, McGraw Hill Book Co. (1968).
12. R.C.Benson and M.R.Mirarchi, IEEE Trans.Milit.Electr. MIL-8, 13 (1964).
13. W.Buchman et al, IEEE J.Quantum Electron, QE-6, 747 (1970).

14. I.W.Mackintosh, Appl.Opt. 8, 1991 (1969).
15. B.A.Davydov et al, Sov.J.Quantum Electron. 4, 1406 (1975).
16. P.Kafalas et al, Appl.Phys. 35, 2349 (1964).
17. B.H.Soffer, J.Appl.Phys. 35, 2551 (1964).
18. M.Born and E.Wolf, Principles of optics, 2nd edn,
Macmillan (1964).
19. B.H.Billings, J.Opt.Soc.Am. 39, 797 (1949).
20. B.H.Billings, J.Opt.Soc.Am. 39, 802 (1949).
21. W.R.Hook and R.P.Hilberg, Appl.Opt. 10, 1179 (1971).
22. D.Milam, Appl.Opt. 12, 602 (1973).
23. L.L.Steinmetz et al, Appl.Opt. 12, 1468 (1973).
24. R.P.Hilberg and W.R.Hook, Appl.Opt. 9, 1939 (1970).
25. W.R.Hook et al, Proc.IEEE, 59, 1126 (1971).
26. R.V.Lovberg et al, IEEE J.Quantum Electron. QE-11, 17 (1975).
27. A.J.De Maria, Proc.IEEE, 57, 2 (1969).
28. D.D.Bhawalkar, Proc.Indian Nat.Sci.Acad.A, 37, 200 (1971).
29. H.Weichel, J.Appl.Phys. 44, 3635 (1973).
30. Lawrence Livermore Laboratory, Laser Program Annual Report
UCRL-50021 (1975-1979).
31. C.G.Young, Appl.Phys.Lett. 2, 151 (1963).

32. O.K.Deutschbein, Rev.Phys.Appl. 2, 29 (1967).
33. W.Koechner, Solid-state laser engineering, Springer Verlag (1976).
34. P.W.Pace and J.B.Atkinson, Rev.Sci.Instrum. 47, 1215 (1976).
35. D.H.Dishington et al, Appl.Opt. 13, 2300 (1974).
36. J.P.Markiewicz and J.L.Emmett, IEEE J.Quantum Electron. QE-2, 707 (1966).
37. ILC Data sheets on flashlamps.
38. W.R.Hook et al, IEEE Trans.on Electron Devices, ED-19, 308 (1972).
39. W.F.Herg and R.C.Lee, IEEE Trans.on Electron Devices, ED-23, 1164 (1976).
40. W.R.Sooy, Appl.Phys.Lett. 7, 36 (1965).
41. B.B.McFarland et al, Nature, 207, 1180 (1965).
42. D.Huppert and P.M.Rentzepis, Appl.Phys.Lett. 32, 241 (1978).
43. Kodak data sheets on dye Q-switches.
44. K.H.Drexhage and G.A.Reynolds, IEEE J.Quantum Electron. QE-10, 720 (1974).

Chapter 2

LASER DAMAGE MECHANISMS

2.10 Introduction

Optically induced damage to laser materials and to components generally determine the limit of the useful performance of high-power solid-state lasers. Therefore, an understanding of the mechanisms which cause radiation damage to optical components and a knowledge of the damage threshold of the materials employed in building a laser are of great importance in designing a laser system. Damage may occur either internally or at the surface of an optical component. Internal damage is caused by particulate inclusions, small inhomogeneities, absorption or self-focusing in the material. Surface damage arises mainly from impurities, imperfections, inclusions or irregularities on the surface of transparent dielectrics¹. Of the two, surface damage is generally more serious because the surface damage thresholds are always found to be 0.3-0.5 times the bulk values.

Laser damage threshold can be defined as the physical appearance of a defect in the material or as a

degradation in the output performance of the laser system. Since it is very difficult to relate an observed damage centre to the degradation in laser performance, damage threshold is defined as the energy or power density at which a change in physical appearance of the test component has been observed. Damage threshold is also specified in terms of the electric field associated with the laser pulse.

High power lasers used in fusion and other high energy systems are required to operate over long periods of time without appreciable degradation in performance. Optical thin film coatings have been the weakest link in such laser systems. These optical coatings greatly influence not only the design but the operation of these systems as well. The onset of even small damage sites within an optical coating can eventually degrade the beam quality sufficiently to prevent optimum laser operation.

In order to develop quality coatings, one needs to understand the fundamental damage processes and how they vary with frequency and pulse length². The three most frequently proposed processes by which laser-induced damage occurs in a dielectric thin film material are avalanche ionization, multiphoton ionization and absorption by

impurities within the films. Avalanche ionization occurs when an electron in the conduction band of a material absorbs enough energy from the electromagnetic field to impact ionize a valence electron. The two electrons can then undergo the same process to produce four conduction electrons and so on. The density of electrons in the conduction band grows exponentially with time until an absorbing plasma is formed. The plasma absorbs energy from the electromagnetic field more efficiently and catastrophic damage to the material occurs from the locally deposited energy³. In the case of multiphoton ionization the electrons are promoted from the valence to the conduction band by direct absorption of two or more photons resulting in a plasma. The number of photons required for each ionization depends on the band gap of the material and the laser wavelength. Impurity dominated damage is a thermal process and takes place when an impurity in the film absorbs enough laser radiation to produce melting or fracture of the host material.

An extensive amount of research has been carried out involving laser-induced breakdown studies as a function of laser wavelength⁴⁻¹⁷, pulse length¹⁸⁻²¹ and film thickness²²⁻²⁶. The frequency dependence of laser damage has frequently been proposed as the main theoretical bench mark

in distinguishing between the competing processes^{4-17,27,28}. This results mainly because avalanche and multiphoton ionization theories predict conflicting laser wavelength dependencies, while theories of impurity dominated damage predict little wavelength dependence. However, if the Mie absorption coefficient³ is included in an impurity model there is no longer a definite distinction between the wavelength predictions of the multiphoton and impurity models. This lack of distinction arises because the films can only be tested at a few discrete available laser wavelengths across the frequency spectrum. Furthermore, both theories predict a general decrease in damage threshold with an increase in laser frequency³.

In general, studies of breakdown as a function of only one parameter cannot be expected to uncover the dominant mechanism of laser damage and often lead to controversial conclusions^{28,29}. It is also not possible to correlate the results of the past research efforts to obtain a multi-parameter study of the breakdown process because each individual experiment will be performed on a different set of films and usually under sufficiently different experimental conditions. The investigated films may vary in their method of substrate preparation, film thickness, quality of starting materials and

deposition technique. These parameters are of vital importance in determining the type, size and distribution of impurities in a film.

Both avalanche and multiphoton ionization calculations on laser-induced damage threshold require complicated parameters such as the material band structure and electron effective mass which are often not available for many of the dielectrics. In the case of impurity model, it requires a detailed knowledge of the type, size and distribution of impurities in the host material. Because of the difficulties in evaluating these parameters, it is impossible to calculate the damage threshold by each of the competing theoretical approaches. Therefore, the only practical way to determine the most appropriate model is to examine their predictive ability in describing the variation of damage with easily controlled experimental or material variables such as pulse width, wavelength and film properties.

In this chapter a brief description of each of the above-mentioned interaction mechanisms is given. This is followed by the damage mechanism in metals where an appreciable thermal absorption of the sample results in the melting of the surface. In the case of polymer materials, a number of

characteristic features are observed which distinguish them from other transparent dielectrics when exposed to high-power nanosecond laser radiation. Out of a number of mechanisms proposed to explain these characteristics, one mechanism based on the sharply pronounced viscoelastic properties of these materials agrees well with the experimental observations. A brief qualitative analysis of this mechanism has also been presented.

The interaction mechanisms leading to damage in dielectrics, metals and polymers given in this chapter form an introduction to the main studies reported in the subsequent two chapters of the thesis.

2.20 Avalanche ionization

According to the avalanche model³⁰ the rate of energy gain of a conduction electron from an alternating electric field $\vec{F} = \vec{F}_0 \cos \omega t$ is given by

$$\left(\frac{dE}{dt}\right)_F = \frac{e^2 F_0^2 \tau_k}{m^* (1 + \omega^2 \tau_k^2)} \quad (2.1)$$

where τ_k is the electron phonon relaxation time for large angle scattering, and m^* is the conduction electron effective

mass. The rate of energy loss to the lattice phonons is

$$\left(\frac{dE}{dt}\right)_L = \frac{\hbar\omega_p}{\tau_L} \quad (2.2)$$

where τ_L is the relaxation time when both large and small angle scatterings are considered and ω_p is the average phonon frequency. If there are n_{co} conduction electrons per unit volume when the laser irradiation is initiated, the conduction electron density at the end of the laser pulse duration of t_p seconds will be

$$n_c = n_{co} 2^{(t_p/t_i)} \quad (2.3)$$

where t_i is the time interval during which a conduction electron starting with zero energy attains an energy equal to the band-gap energy. It has been well established³¹ that when the conduction electron density reaches a value of the order of $10^{18}/\text{cm}^3$, the absorption of the residual laser becomes appreciable, leading to localized heating and subsequent irreversible damage to the optical material. Therefore, the appearance of 10^{18} conduction electrons/ cm^3 is taken as the criterion for laser-induced damage. If we can assume that the ionization of weakly bound sites

such as F-centres, impurities etc. give rise to an initial conduction electron density of $10^9/\text{cm}^3$ equations (2.1) to (2.3) give the following expression for the damaging electric field amplitude in mks units³²:

$$F_{\text{damage}} \simeq \left[\frac{m^* (1 + \omega^2 \tau_k^2)}{e^2 \tau_k} \left(\frac{E_g \ln 10^9}{0.693 t_p} + \frac{\hbar \omega_p}{\tau_L} \right) \right]^{1/2} \quad (2.4)$$

where E_g is the band gap energy of the crystal. This expression gives the electric field amplitude in pure dielectric materials at the onset of damage.

2.30 Multiphoton ionization

Bloembergen³³ postulated that when the photon energy of the incident light was about a third of the band-gap energy (E_g) of the solid, multiphoton absorption could contribute significantly to the breakdown process. Therefore, the damage threshold would decrease when the laser frequency was increased beyond an equivalent photon energy of $\sim E_g/3$.

The analytic difficulties of treating multiphoton absorption in dielectrics is mainly due to the lack of detailed knowledge of the band structures. There are several

treatments of photon absorption to all orders^{34,35} of which the most widely used is that of Keldysh³⁴. The main reason for its wide acceptance is that the final equations are simple enough to obtain numerical results without lengthy and complex computations. Moreover, this theory in most cases affords the best agreement with experiment³⁶ and for higher order multiphoton processes—greater than three—it is the only theory that can be used to obtain sensible numerical results when compared to the available experimental results. Thus, Keldysh formula gives meaningful results for first order as well as higher order photon processes.

According to Keldysh's theory, the dependence of the critical energy per unit area on the pulse width t_p reveals that if $E_g < h\omega$, the breakdown process is independent of time. For very high order photon processes, $E_g \gg h\omega$, and the process depends linearly on time. Also, it can be shown that the multiphoton theory predicts a decrease in the breakdown field with increase in laser frequency.

2.40 Impurity dominated breakdown

There has been a great deal of theoretical work on damage produced by impurities in dielectric host

materials^{37,38}. Even now, the leading damage mechanism in very pure bulk materials is not yet clear. A recent work by Solieu³⁹ supports avalanche ionization for large laser spot sizes. The role of impurity dominated breakdown assumes importance in the case of surfaces, and particularly in thin films. This is because of the large absorption coefficient of most thin films which ranges from 10 cm^{-1} to 1000 cm^{-1} . For the same material in bulk form the range is several orders of magnitude smaller and surface absorption values falls in between. The high absorptivity of thin films is generally attributed to impurities which are included during the deposition process or infiltrate during exposure to the environment. Experimental data indicates that the breakdown threshold can be more than an order of magnitude lower for thin films than for the same materials in bulk form.

The model most frequently employed for impurity damage is that of spherical absorbing particles embedded in a host material. The impurity absorbs the incident radiation and its temperature rises, which ultimately produces melting, vapourisation or stress fracture of the film material around the impurity.

In the case of metallic impurities, the approximate solution of the thermal equation given by Hopper and Uhlmann³⁷ can be used to obtain the temperature in the host film material. The solution is given by

$$\begin{aligned}
 T = \frac{3QI}{2\pi C_p D_h m r} & \left(\frac{1}{q-m} \operatorname{erfc} \frac{r-a}{2\sqrt{D_h t_p}} - \frac{1}{q+m} \operatorname{erfc} \frac{r-a}{2\sqrt{D_h t_p}} \right. \\
 & - \frac{1}{q-m} \exp \left[\frac{(q-m)(r-a)}{2a} + \frac{(q-m)^2 D_h t_p}{4a^2} \right] \operatorname{erfc} \left[\frac{r-a}{2\sqrt{D_h t_p}} + \frac{(q-m)\sqrt{D_h t_p}}{2a} \right] \\
 & + \frac{1}{q+m} \exp \left[\frac{q+m(r-a)}{2a} + \frac{(q+m)^2 D_h t_p}{4a^2} \right] \operatorname{erfc} \left[\frac{r-a}{2\sqrt{D_h t_p}} \right. \\
 & \left. \left. + \frac{(q+m)\sqrt{D_h t_p}}{2a} \right] \right) \quad (2.5)
 \end{aligned}$$

where C_p = volume specific heat density of an impurity of radius 'a'

k_h = thermal conductivity of the host material

D_h = thermal diffusivity of the host material

Q = absorption cross section

I = incident laser intensity

C_h = specific heat density of the host material

t_p = laser pulse length

$q = \frac{3C_h}{C_p}$ and $m = [q(q-4)]^{\frac{1}{2}}$; r = radial distance from the impurity boundary

In the case of impurities such as oxides and other dielectric materials which have a very small coefficient of thermal diffusivity⁴⁰, the above solution of the thermal equation is not valid. For dielectric impurities in the form of a sphere, an exact solution is required to the thermal equation. The solution in this case is given⁴¹ as

$$T = \frac{3QI}{4\pi k_p a} \left(\frac{1}{3} \frac{k_p}{k_h} + \frac{1}{6} \left(1 - \frac{r^2}{a^2} \right) - \frac{2ab}{\pi} \int_0^{\infty} \exp\left(\frac{-y^2 t_p}{\gamma_1}\right) \frac{(\sin y - y \cos y) \sin(ry/a)}{y^2 (c \sin y - y \cos y)^2 + b^2 y^2 \sin^2 y} dy \right) \quad (2.6)$$

where $\gamma_1 = \frac{a^2}{D_p}$; $c = 1 - \left(\frac{k_h}{k_p}\right)$; $b = \frac{k_h}{k_p} \sqrt{\frac{D_p}{D_h}}$

where D_p , D_h , a , k_p , Q , I are as previously defined. This solution is equally applicable even in the case of metallic impurities.

An assumed constant value for Q is only valid if the impurity is much greater in size than the wavelength of the incident radiation. In the case of thin films, the impurity size is usually limited by the thickness of the film, and therefore, the impurity sizes are of the same order as the wavelength of light or smaller. It has also been shown that³ the size of the impurity which is most sensitive to damage is of the same order of magnitude as the wavelength of the laser radiation used. If impurities of this size are the initiating sites for damage, then the energy absorption should be determined by the Mie absorption cross section.

If one assumes a constant value of Q in (2.6), there is no frequency dependence. But, if an asymptotic analytic expression for the Mie absorption cross section for Q is introduced in equation (2.6) a frequency dependence is obtained. Such an expression can be given for the Mie cross section if the real index of refraction (n) is between 1 and 2 and the imaginary index (n') is much less than one.

In the case of dielectric impurities it has been shown that^{42,43} the value of Q is given by

$$Q = \pi a^2 \left[1 + \frac{2e^{-(8\pi n' a/\lambda)}}{8\pi n' a/\lambda} + \frac{e^{-(8\pi n' a/\lambda)} - 1}{(8\pi n' a/\lambda)^2} \right] \quad (2.7)$$

where a = impurity radius and λ = wavelength of light. It is seen that the cross section affords a wavelength dependence as well as an additional impurity radius dependence.

In the case of metallic impurities, the Mie absorption cross section is approximately given by

$$Q = \pi a^2 \left(\frac{A\lambda}{n'a} + B \right) \quad (2.8)$$

where A and B depend on the specific metal.

The greatest difficulty in applying a Mie coefficient in the proposed theory is that the composition of the impurities is not known for most films. In addition, the imaginary index of refraction n' of the impurities is a function of frequency and, as a result, comparison between

experiment and theory can only be relative and not absolute. That is, this impurity model can only predict trends in the breakdown field and not absolute damage thresholds. The breakdown criterion which will be used along with the Mie impurity model will be one of temperature. A fixed critical temperature is set such as the melting temperature of the host material, and the incident energy density is plotted against the impurity size. The minimum energy per unit area required to heat an impurity to the critical temperature is then taken as the damage threshold. It is assumed that once the critical temperature is reached, the damage proceeds catastrophically. The breakdown threshold has been shown to decrease at shorter wavelengths for both oxide and metallic impurities³. This dependence is contained in the Mie absorption coefficient.

Investigations have shown that in the nanosecond time regime the critical energy per area fits closely to a square root of time dependence⁴⁴. Time dependence of damage obtained using equation (2.6) and these experimental values agrees well.

The most noticeable feature unique to the impurity model is the prediction of an increase in damage threshold with a decrease in film thickness. This ensues from the

quite reasonable assumption that the maximum size of an impurity is limited by the film thickness i.e., as the film thickness increases so do the impurity size. This observation is well documented by earlier works³ in which this has been confirmed for many types of optical thin films.

Since the experimental determination of the thermal properties of the inclusion and host is a difficult problem, it will be worthwhile if a theoretical study of the sensitivity of the damage threshold to these quantities is made. Towards this end Lange et al⁴⁵ have developed an approximate method of evaluating the integral in equation (2.6) by assuming that $D_p t_p / a^2 \gg 1$. The radius at which damage first occurs is then given by

$$a_0 = \frac{\sqrt{\pi D_h t_p}}{2} \quad (2.9)$$

and the damage threshold is

$$E_0 = 16T \frac{\sqrt{f_h C_{ph} k_h t_p}}{\pi} \quad (2.10)$$

This equation not only verifies the $\sqrt{t_p}$ dependence previously suggested³ but also predicts that the damage threshold scales

linearly as the temperature at which damage occurs and as the square root of the product of the specific heat and thermal conductivity of the host. In this reasonable approximation, the damage threshold is independent of the properties of the impurity.

It has been shown that neither the avalanche nor the multiphoton model alone can explain all of the experimentally observed features of laser-induced damage. It is suggested that it is more appropriate to combine these two mechanisms into a single formulation so that it offers a better fit to the experimental data. Also, the inclusion of the effect of multiphoton transition on the avalanche ionization frequency can bring the theoretical prediction closer to the experimental results³². Although both the avalanche and multiphoton models, either separately or combined can account for portions of the data, contradictions occur when all of the data is dealt with as a whole. The trends observed in the experimental data are not adequately described by these two models. This conclusion is further substantiated by the fact that neither the avalanche nor the multiphoton theory contains any feature which can account for the observed film thickness dependence³.

In this background, the impurity dominated breakdown model assumes importance. This model has been successful in describing the scaling of damage threshold with respect to the laser pulse duration and the thermal properties of the film for fluoride films.

2.50 Laser-induced damage to metals

When appreciable thermal absorption is present in a sample the damage mechanism may be melting of the surface or cracking due to thermally induced strain. Damage to metal mirrors is principally caused by the absorption of radiation leading to melting of the surface⁴⁶. When a beam of light strikes a metal surface, a small amount of the radiation penetrates the metal to a distance called the skin depth. When the incident radiation is absorbed by free carriers, under certain circumstances, the temperature of the metal surface raises above the melting point and damage occurs⁴⁷. The resulting temperature rise can also be calculated⁴⁸. Damage threshold is found to depend on the absorptivity and the thermal properties of the sample. Theory⁴⁹ shows that the damage threshold energy density E_D is found to depend on the relation

$$E_D \propto \frac{(T_m - T_o) (K\rho C)^{\frac{1}{2}}}{\alpha_o} \quad (2.11)$$

where

T_m = melting temperature ($^{\circ}\text{K}$)

T_o = Ambient temperature ($^{\circ}\text{K}$)

ρ = Density (gm/cm^3)

K = Coefficient of thermal conductivity

c = specific heat ($\text{J}/\text{K}/\text{gm}$)

α_o = absorptivity (at T_o , at $\lambda = 10.6\mu$)

For a mirror with a coating, α_o is the value associated with the coating whereas K , ρ and c refer to the substrate. T_m refers to the material with the lower melting point. Good agreement between this theory and experiment has been reported⁵⁰.

2.60 Laser damage to transparent polymers

When transparent polymers are exposed to high power nanosecond laser radiation, a number of characteristic features are observed which distinguish them from other transparent dielectrics⁵¹. The characteristic features include a low damage threshold compared with that of the

crystals⁵²; a strong dependence of the optical strength on the viscoelastic properties and temperature; a wide range of radiation intensities below the damage threshold in which the cumulative effect is observed; the occurrence of microdamage of dimensions $\geq 10\mu$ which is not accompanied by a bright spark⁵³; formation of highly absorbing products such as soot during the damage process⁵⁴; and a surface strength higher than the bulk strength of the polymers⁵⁵.

In order to explain these characteristics, various mechanisms of laser damage have been proposed. Damage has been explained in terms of multiphoton photo destruction of the polymer chains⁵⁶. Mechanisms based on the formation of highly absorbing products around inclusions (as a result of chemical changes at high temperatures) have also been analysed⁵⁷⁻⁵⁹. The anomalous viscoelastic properties of polymers can lead these materials to damage even when the heating of absorbing inclusions is negligible⁵³. A mechanism of nonlinear absorption of laser radiation associated with a triboprocess in the matrix surrounding the inclusion accompanied by the formation of microcracks in the matrix has also been proposed⁶⁰. This mechanism could explain the formation of visible damage ($> 1\mu$) initiated by small inclusions ($\leq 0.1\mu$). This essentially involves surface electronic states being formed during the microcrack formation process. These states are capable of absorbing the incident

radiation energy efficiently and cause damage. The existence of these states is indicated by the subthreshold luminescence in the visible and near UV due to their radiative deactivation⁶¹.

An analysis of this damage mechanism has been given by Manenkov et al⁵¹. In this analysis a spherically symmetric absorbing defect comprising a region of small dimension ($a < \lambda$) and having an absorption coefficient appreciably higher than that of the surrounding matrix is considered. When the defect absorbs energy from a rectangular laser pulse of duration t_p , thermoelastic stresses which increase with time are induced in the matrix. At a certain time, the stresses reach the microbreaking strength of the material which corresponds to the formation of microcracks. If further radiation energy is absorbed and the thermoelastic stresses are further increased, the concentration of microcracks and thereby the concentration of the electronic states (formed during microcrack formation) capable of efficiently absorbing laser radiation energy increases.

Assuming that the thermoelastic stresses near an inclusion are proportional to its temperature, we can describe the process of nonlinear heating of the medium containing an absorbing defect using a heat conduction equation which describes

the absorption of laser radiation energy by the defect and by the electronic states. The solution of this equation gives an expression for the temperature at the centre of the defect.

The damage threshold can be determined from the condition of loss of stability of the steady-state solution of the equation for the temperature variation with respect to time. This mechanism of laser damage to polymers accurately explains the main characteristics of damage to polymers and determines the threshold condition for the formation of micro-cracks and microdamage.

However, the dominant laser damage mechanism in polymers has not yet been identified and ways of increasing the optical strength of polymers are not yet clear⁶².

REFERENCES

1. N.Bloembergen, Appl.Opt. 12, 661 (1973).
2. A.H.Guenther, Tenth symposium of optical materials for high power lasers - Introduction, NBS Special Publication 541, US GPO Washington, DC (1978).
3. T.W.Walker, Ph.D thesis (1979), Air force Inst.of Techgy., Ohio.
4. A.G.Molchanov, Sov.Phys.Solid State, 12, No.3, 749 (1970).
5. A.S.Epifanov, Sov.Phys.JETP 40, No.5, 897 (1974).
6. W.L.Smith, J.H.Bechtel and N.Bloembergen, Phys.Rev.B,15, No.8, 4039 (1976).
7. A.V.Vinogradov and F.S.Faizullov, Sov.J.Quant.Elect. 7, 650 (1977).
8. A.Schmid, P.Kelly, and P.Braunlich, NBS Special Publication 509, US GPO Washington, DC (1977).
9. A.S.Epifanov, A.A.Manenkov, and A.M.Prokhorov, Sov.Phys. JETP Lett. 21, No.8, 223 (1975).
10. B.G.Gorshkov, Yu K.Danileiko, A.S.Epifanov, V.A.Lobachev, A.A.Manenkov and A.V.Sidorin, Sov.Phys.JETP, 45, No.3, 612 (1977).
11. M.J.Soileau and M.Bass, Appl.Phys.Lett. 35, No.5, 370 (1979).

12. D.W.Fradin and E.Yablonoitch, Laser induced damage in optical materials, NBS Special Publication 372, US GPO Washington, DC (1972).
13. M.Bass and H.H.Barrett, Laser induced damage in optical materials, NBS Special Publication 372, US GPO Washington, DC (1972).
14. J.O.Porteus, M.J.Soileau, H.E.Bennett and M.Bass, Laser induced damage in optical materials, NBS Special Publication 435, US GPO Washington, DC (1975).
15. B.E.Newnam and D.H.Gill, Laser induced damage in optical materials, NBS Special Publication 462, US GPO Washington, DC (1976).
16. J.O.Porteus, T.M.Donovan, J.L.Jernigan and W.N.Faith, Laser induced damage in optical materials, NBS Special Publication 541, US GPO Washington, DC (1978).
17. B.E.Newnam and D.H.Gill, Laser induced damage in optical materials, NBS Special Publication 541, US GPO Washington, DC (1978).
18. J.M.McMahon, Laser induced damage in optical materials, NBS Special Publication 372, US GPO Washington, DC (1972).
19. V.Wang, C.R.Guiliano, and B.Garcia, Laser induced damage in optical materials, NBS Special Publication 435, US GPO Washington, DC (1975).

20. J.R.Bettis, R.A.House II, and A.H.Guenther, Laser induced damage in optical materials, NBS Special Publication 462, US GPO Washington, DC (1976).
21. D.Milam, Laser induced damage in optical materials, NBS Special Publication 541, US GPO Washington, DC (1978).
22. B.E.Newnam, D.H.Gill, and G.Faulkner, Laser induced damage in optical materials, NBS Special Publication 435, US GPO Washington, DC (1975).
23. J.H.Apfel, J.S.Matteucci, B.E.Newnam, and D.H.Gill, Laser induced damage in optical materials, NBS Special Publication 462, US GPO Washington, DC (1976).
24. L.G.DeShazer, B.E.Newnam, and K.M.Leung, Laser induced damage in optical materials, NBS Special Publication 387, US GPO Washington, DC (1973).
25. J.H.Apfel, Laser induced damage in optical materials, NBS Special Publication 509, US GPO Washington, DC (1977).
26. D.H.Gill, B.E.Newnam, and J.McLead, Laser induced damage in optical materials, NBS Special Publication 532, US GPO Washington, DC (1977).
27. A.A.Manenkov, Laser induced damage in optical materials, NBS Special Publication, US GPO Washington, DC (1978).

28. M.J.Soileau, M.Bass, and E.W.Van Stryland, Laser induced damage in optical materials, NBS Special Publication 541, US GPO Washington, DC (1978).
29. I.V.Aleshin, A.A.Doman, and Ya.A.Imas, Sov.Tech.Phys. Lett. 4, No.7 348 (1978).
30. M.Sparks and C.J.Duthler, Theoretical studies of high power ultraviolet and infrared materials, Fifth technical report, Xonics Inc., Van Nuys, CA, June 1975; M.Sparks, Current status of electron-avalanche breakdown theories, Laser-induced damage in optical materials, NBS Special Publication 435, p.331 (1975).
31. N.Bloembergen, Laser-induced electric breakdown in solids, IEEE J.Quantum Electron, QE-10, p.375 (1974).
32. A.Vaidyanathan et al, Laser induced damage in optical materials, NBS Special Publication 568, US GPO Washington, DC (1979).
33. N.Bloembergen, IEEE J.Quant.Elect. QE-10, 375 (1974).
34. L.V.Keldysh, Sov.Phys.JETP 20, No.8, 1307 (1965).
35. H.D.Jones, and H.R.Reiss, Phys.Rev.B 16, No.6, 2466 (1977).
36. F.Adduci, I.M.Catalano, A.Cingolani, and A.Mingfra, Phys.Rev. B 15, No.2, 926 (1977).
37. R.W.Hopper, and D.R.Uhlmann, Appl.Phys.41, No.10, 4023 (1970).
38. D.Milam, R.A.Bradbury, and M.Bass, Appl.Phys.Lett. 23, No.12, 654 (1973).

39. M.J.Solieu, Ph.D Dissertation, University of Southern California (1979).
40. M.Sparks, and C.J.Duthler, Theoretical studies of high power ultraviolet and infrared materials, p.11, Eight Technical Report (1976).
41. H.Goldenberg, and M.A.Tranter, Brit.J.Appl.Phys. No.2, 296 (1952).
42. H.C.Van de Hulst, Light scattering by small particles, John Wiley & Sons, Inc., New York (1957).
43. R.J.Cook, and R.R.Butts, Laser Digest, AFWL-TR-73-273, 69 (1973).
44. D.Milam, Laser induced damage in optical materials, NBS Special Publication 541, US GPO Washington, DC (1978).
45. M.R.Lange, J.K.Mclver, A.H.Guenther and T.W.Walker, Proc.of the Los Alamos Conf. on Optics 1983, SPIE 380, 450 (1983).
46. R.M.Wood, S.K.Sharma and P.Waite, SPIE 369, 84 (1983).
47. J.F.Ready, IEEE J.Quantum Electron, QE-2, 137 (1976).
48. R.Gibbs and R.M.Wood, N.B.S.Special Publication 462, 181 (1976).
49. Ready, J.Appl.Phys. 36, 2, 462 (1965).

50. R.M.Wood, S.K.Sharma and P.Waite, GEC Jnl.of Sci. and Technology, 48, 3, 141 (1982).
51. A.A.Manenkov, V.S.Nechitailo and A.S.Tsaprilov, Sov.J. Quantum Electron. 11 (4), 502 (1981).
52. B.M.Ashkinadze et al. Sov.Phys.JETP, 23, 788 (1966).
53. M.I.Aldoshin et al, Sov.J.Quantum Electron. 9, 1102 (1979).
54. A.I.Akimov et al. Mekh. Polim. No.3, 493 (1967).
55. A.S.Bebchuk et al. Sov.J.Quantum Electron. 6, 986 (1976).
56. M.B.Agranat et al. Sov.Phys.JETP, 33, 944 (1971).
57. A.V.Butenin and B.Ya, Kogan, Sov.J.Quantum Electron. 6, 611 (1976).
58. M.A.Liberman and M.I.Tribel'skií, Sov.Phys.JETP, 47, 99 (1978).
59. A.A.Kovalev et al. Sov.Tech.Phys.Lett. 6, 142 (1980).
60. Yu.K.Danileiko et al. Proc.Fourth All Union Conf. on Nonresonant Interaction between Optical Radiation and Matter, State Optical Institute, Leningrad, p.154 (1978).
61. A.A.Manenkov et al. Izv.Akad.Nauk SSSR Ser.Fiz, 44, 1770 (1980).
62. K.M.Dyumaev et al. Sov.J.Quantum Electron. 13 (4), 503 (1983).

Chapter 3

LASER-INDUCED DAMAGE STUDIES ON TRANSPARENT- CONDUCTIVE COATINGS

3.10 Introduction

Oxides of tin, indium, cadmium, zinc and their various alloys, deposited by numerous techniques exhibit high transmittance in the visible region, high reflectance in the IR and nearly metallic conductivity. The electrical as well as the optical properties of these unusual materials can be tailored by controlling the deposition parameters. Most prominent among them are oxides of indium and tin doped with appropriate dopants.

Transparent conducting films have found major applications in a vast number of active and passive electronic and opto-electronic devices ranging from aircraft window heaters to charge-coupled imaging devices. With increasing sophistication of these devices, the need for improved electrical and optical properties and their understanding was recognized. In the last several years, the deposition techniques have undergone many changes and an understanding

of the solid state physics of these materials has begun to emerge and now it is possible to tailor make various transparent conductors with a wide range of properties by controlling the deposition parameters¹. Transparent-conductive indium tin oxide (ITO) coatings can be used as the electrodes on electro-optic devices employed in high energy lasers to suppress spurious laser radiation or to prevent retro-reflections from damaging the laser². In longitudinal electro-optic (E-O) shutters based on Pockels effect, the electric field on the crystal is maintained parallel to the lasing axis by applying suitable voltage on the circular ring electrodes kept on either side of the crystal. To achieve adequate electric field uniformity over the aperture a crystal length-to-diameter ratio of $\gg 1:1$ is required³. Though crystals with apertures upto 5 cm are available, they are very expensive and difficult to grow. To overcome the field nonuniformity associated with such structures, cylindrical band electrodes are applied to the end of the crystals or transparent conducting coatings are deposited on glass substrates. Because of the high field uniformities attainable, the length to diameter constraint is reduced. Thin disc crystals can now be used thereby reducing the cost of the device. These crystals also reduce the scattering and absorption losses. The films that are usually used on E-O modulators at

1060 nm are stannic oxide or its doped films. These films have relatively high damage thresholds and high transmission at 1060 nm. To date only very little information is available on the damage thresholds of such films. Damage threshold of 5-6 J/cm² was reported for transparent-conductive ITO films^{2,4}. These $\lambda/2$ thick (at 1060 nm) coatings deposited on fused silica by reactive sputtering were tested for damage using 1 ns laser pulses at 1060 nm. Damage studies on stannic oxide films prepared by chemical vapour deposition (CVD) was carried out using 20 ns laser pulses at 1062 nm⁵, and these films were shown to be good substitutes for the ITO films.

Because of their immense technological importance, extensive investigation is being carried out especially in the preparation and characterisation of these films. It is found that the quality of the film obtained depends largely on the method adopted for the preparation. Moreover, even the deposition parameters of a particular method are found to influence largely the characteristics and thereby the damage threshold of these films. These films have been prepared by almost all thin film deposition techniques. They include the post deposition oxidation of metal⁶, reactive evaporation⁷, direct evaporation by thermal⁸ and EBE⁹,

sputtering¹⁰, reactive ion plating¹¹, chemical vapour deposition¹², spray pyrolysis¹³, dip techniques¹⁴, chemical solution growth¹⁵ etc. The film of best quality was that of indium doped tin oxide obtained by spray pyrolysis closely followed by the sputtered film of indium tin oxide¹⁵. Since the electrical and optical transport in these films depend strongly on their microstructure and stoichiometry and the nature of the impurities present, each deposition technique with its associated parameters yields films of different properties. Depending on the deposition technique, even the substrate can have a significant influence on the properties of the films¹⁶.

3.20 Structural, electrical and optical properties

The structural, electrical and optical properties of these transparent-conductive coatings are widely scattered. This is attributable to the diverse nature of the techniques employed and the strong influence of the deposition conditions on the properties of these films. Two parameters which are practical measures of the conductivity and transparency are the sheet resistance R_{sh} and the average visible transmittance T . R_{sh} is related to the resistivity by

$$R_{sh} = \rho(t)/t = 1/\sigma(t)t \quad (3.1)$$

The average transmittance of an unsupported film at any wavelength λ is given by

$$T_{\lambda} = (1-R_{\lambda})^2 \exp(-\alpha_{\lambda}t) \quad (3.2)$$

where R_{λ} is the reflection coefficient, and α_{λ} is the absorption coefficient which in the visible region is primarily due to free carriers.

The phenomena of conductivity and transparency are quite strongly interrelated. The exact nature of this interdependence is determined by the influence of various deposition parameters on the electro-optical properties of these films. However, for films deposited under optimum conditions both R_{λ} and T_{λ} depend significantly on the film thickness¹.

In this chapter the damage threshold studies carried out on some transparent-conductive coatings using the Q-switched Nd:glass laser emitting 25 ns (FWHM) pulses at 1062 nm are reported. The samples studied are tin oxide prepared by chemical vapour deposition and spray pyrolysis and indium tin oxide prepared by reactive rf sputtering. The method of deposition and the deposition parameters which influence the

damage threshold have been given in each case. The indium tin oxide coatings prepared by reactive rf sputtering were supplied by Dr. Abhai Mansingh, Professor, Delhi University.

Preparation of transparent conducting thin films

3.30 Tin oxide films by chemical vapour deposition method

In this method, tin oxide films were prepared by heating commercially available $\text{SnCl}_2 \cdot 2\text{H}_2\text{O}$ in a glass U-tube to about 400°C . Commercial oxygen at a very low pressure was allowed to flow over the sample. The SnCl_2 vapour carried by oxygen was directed onto clean glass substrates kept at about 300°C . The time of deposition was about 15 minutes. The films formed are extremely stable and resistant to chemical etching. Selective etching of tin oxide could be done only by reacting it with nascent hydrogen produced by the reaction of zinc powder with HCl. Adhesion of these films to the glass substrate is also found to be very high. The main control parameters which characterise the film (which determine the electrical and optical properties of the film) are the gas flow, the gas composition, the substrate temperature and the geometry of the deposition apparatus. The deposition rate depends mainly on the gas flow rate and

substrate temperature. The film conductivity is found to decrease with increasing oxygen concentration for the films prepared by this method^{12,17}. Generally the quality of transparent-conductive coatings prepared by this method has been slightly inferior to that of reactively sputtered conductors¹. The uniformity of the film prepared and its electrical characteristics were found to be relatively poor.

3.40 Tin oxide films by spray pyrolysis method

This method yields coatings of very good optical and electrical characteristics with a comparatively simple experimental set up. Further, spray technique is inexpensive and ideally suited for large area substrate applications¹⁸.

In the present case, an aqueous $\text{SnCl}_4 \cdot 5\text{H}_2\text{O}$ solution taken in isopropyl alcohol was sprayed onto a heated glass substrate. The spray strikes the substrates at an oblique angle and the entire process is done in a good stream of air or oxygen. The experimental details are as described elsewhere¹⁹.

The glass substrate to be coated was first cleaned in soap solution and then in chromic acid. It was then placed on a hot plate made of stainless steel which could be heated

upto 500°C. A good stream of air was flown over the hot plate from an electric fan. The spray solution was taken in a special chromatographic sprayer. The spray was produced by blowing compressed air into the sprayer and was controlled by adjusting the air pressure. Spraying was done such that it hits the hot substrate at an angle of about 45°. The air stream and the spray from the nozzle of the sprayer carried away the residual gases which mainly consisted of HCl and alcohol vapour.

Important parameters which determine the quality of the films are the nature and temperature of the substrate, the solution composition, the gas and solution flow rates, the deposition time and the nozzle-to-substrate distance. The optimum substrate temperature within which the optical transmission is practically independent of temperature is within the range 450°C-550°C¹. The size of the droplets and their distribution affect the uniformity of the surface and the transmission of the films²⁰. The typical droplet size is between one and a few microns.

In the present investigations, a number of trials were made with different concentrations of spray solution and with different substrate temperatures. It has been observed

that a saturated solution of $\text{SnCl}_2 \cdot 5\text{H}_2\text{O}$ at room temperature in isopropyl alcohol sprayed on a glass plate kept at about 400°C gave the best films with transmittance ~ 85 percent.

3.50 Indium tin oxide films by rf sputtering method

Sputtering is one of the most extensively used techniques for the deposition of transparent conducting oxide films. Both reactive and non-reactive forms of d.c and rf sputtering are employed. The indium tin oxide coatings used for the present study were deposited as follows²¹.

The glass substrates, after the usual chemical cleaning processes using acetone, trichloroethylene etc. were sputter cleaned at 100 W rf power for 10 minutes. The films were deposited by the reactive rf sputtering technique in an Ar/O_2 atmosphere (80 percent argon and 20 percent oxygen). Metallic alloy of indium tin oxide was used as the target. The substrate was maintained at a temperature of 200°C . An rf biasing voltage of 1400 V applied to the substrate increases the purity of the film by resputtering poorly bonded surface atoms, resulting in improved electrical and optical characteristics²². The deposition rate was $25 \text{ \AA}/\text{minute}$ approximately. The deposited films underwent a post-deposition heat treatment

in a reducing atmosphere at 350°C for 2½ hours in order to obtain the optimum transparent conducting properties²³. The probable film composition is $\text{In}_{2-x}\text{Sn}_x\text{O}_{3-x}$. These films were prepared at Delhi University rf sputtering unit.

3.60 Damage threshold measurement

Though the filamentary hot spots in a multimode laser output has higher energy densities compared to the average energy density, these filamentary structures are focused to spot sizes too small to contribute to damage has established that a TEM_{00} mode laser is not necessary in laser damage studies²⁴. Moreover, real-world lasers are not always operated in the TEM_{00} mode.

Figure 3.1A is a schematic diagram of the damage experiment and the experimental set-up is shown in fig.3.1B. The laser used in this study was the Q-switched Nd:glass laser discussed in Chapter 1. The laser output at 1062 nm had a pulse width of 25 ns at FWHM. The beam structure was multimode and was approximately gaussian in profile with a beam diameter of about 4 mm. The laser output passing through an aperture of 4 mm was focused with a biconvex lens of 20 cm focal length onto the thin film sample. The sample mounted on a rotating platform was

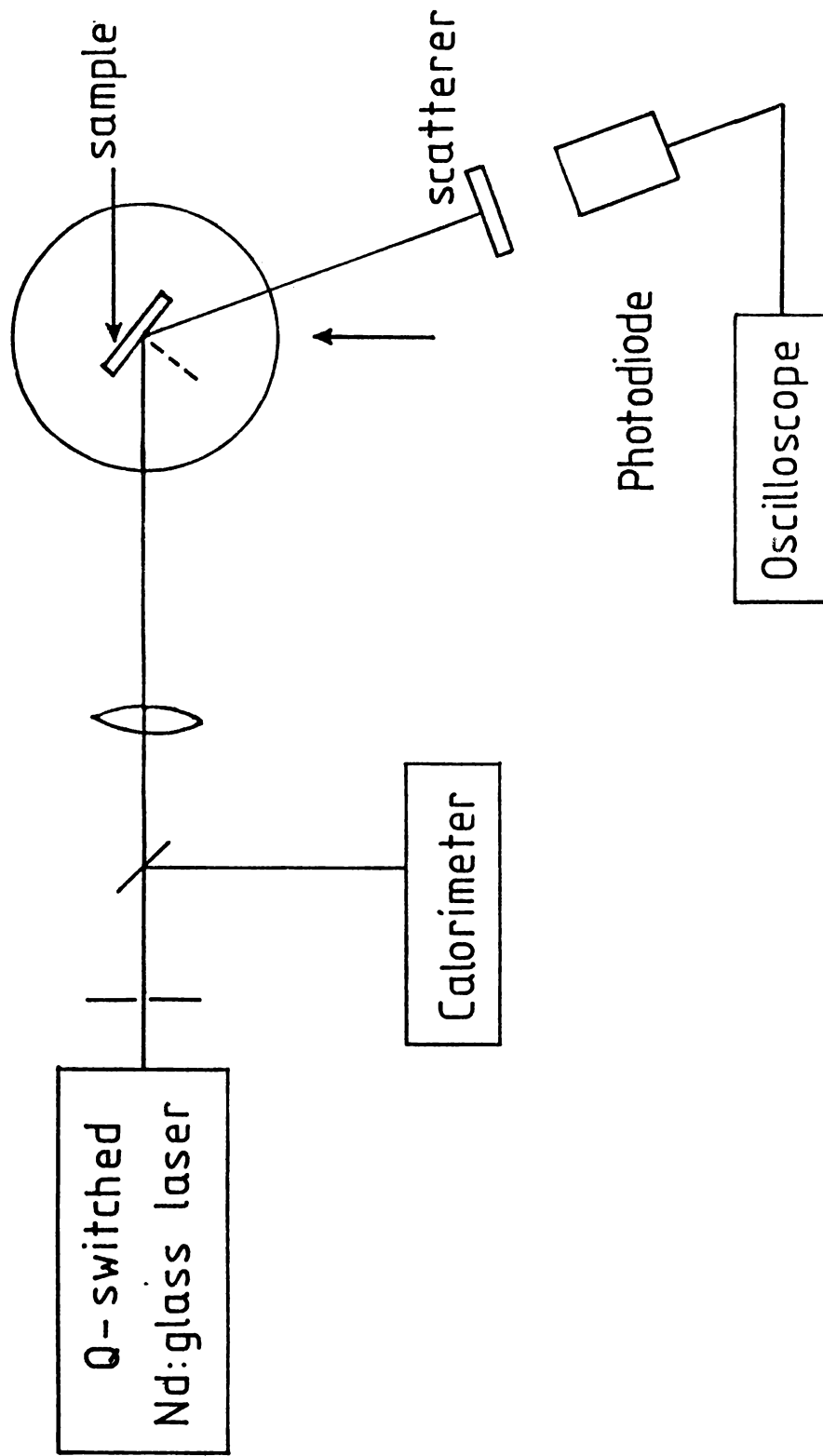


Fig.3.1A Schematic diagram of laser-induced damage threshold measurement.



Fig.3.1B Laser-induced damage threshold measurement set-up.

oriented so that the incident beam makes an angle of 56° with the normal. The large incidence angle was used to avoid multiple beam interference in the glass substrate. The laser pulse width was monitored on a Tektronix storage oscilloscope (Model 466 DM 44) with a Hewlett Packard hp2-4207 photodiode and the energy incident on the sample by a one inch Scientech disc calorimeter (Model 38-0101). Throughout the entire study the laser output energy was kept constant. With the present experimental set up, absolute measurement of the output energy was not possible for every damage attempt. However, an energy calibration was made before and after each set of damage tests. To begin with, the distance between the sample and the lens was adjusted such that the shot impinging on the film damages it. Between successive test shots the thin film sample was pushed in the direction shown by the arrow. This enables the next shot to impinge on a site just near to the previous one. As the film is pushed forward, it moves away from the focus of the lens thereby decreasing the energy density incident on the sample. The film will get just damaged at a particular energy density known as the damage threshold. Once the damage threshold is reached, with subsequent shots there will be no damage at all as the film is pushed forward. When damage is produced on the thin film coatings bright light sparks are observed to be emanating from it. Once the neighbourhood of damage threshold is reached, no such emission is observed.

On completion of a test run, the damage sites were examined in an intense light and the threshold damage location was identified. This was verified using a metallurgical microscope (Carl Zeiss Jena EPY-type:2). Typical photographs of the damage sites observed using this microscope are shown in figs.3.2A and 3.2B. As the laser beam cross section can be assumed to be circular and as the half angle subtended at the lens focus is much less than the angle of incidence (56°), the damage sites will be elliptical in shape. With the help of geometrical considerations, the damaged area can be computed. With the knowledge of the pulse energy, pulse width and the damaged area the threshold energy and power density can be estimated. The values obtained for the tested sample films are given in table 3.1.

3.70 Measurement of refractive index, thickness, absorptance and sheet resistance

Refractive index of the thin film samples were measured by ellipsometric technique. The experimental set up is as shown in fig.3.3. The measurements were made at 435.8 nm. The samples were oriented at 45° to the incident beam direction. When polarised light is incident on a substrate covered by a single film, it gets multiply-reflected inside the film and

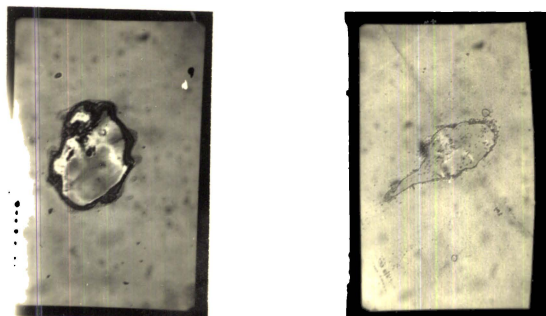


Fig.3.2A Damaged site on indium tin oxide, magnification, $m=25$.
Damaged site on CVD film $m=63$.

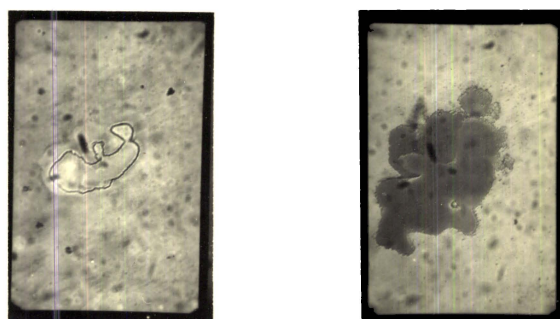


Fig.3.2B Damaged site on SPD film-I, magnification $m=25$.
Damaged site on SPD film-II, magnification $m=63$.

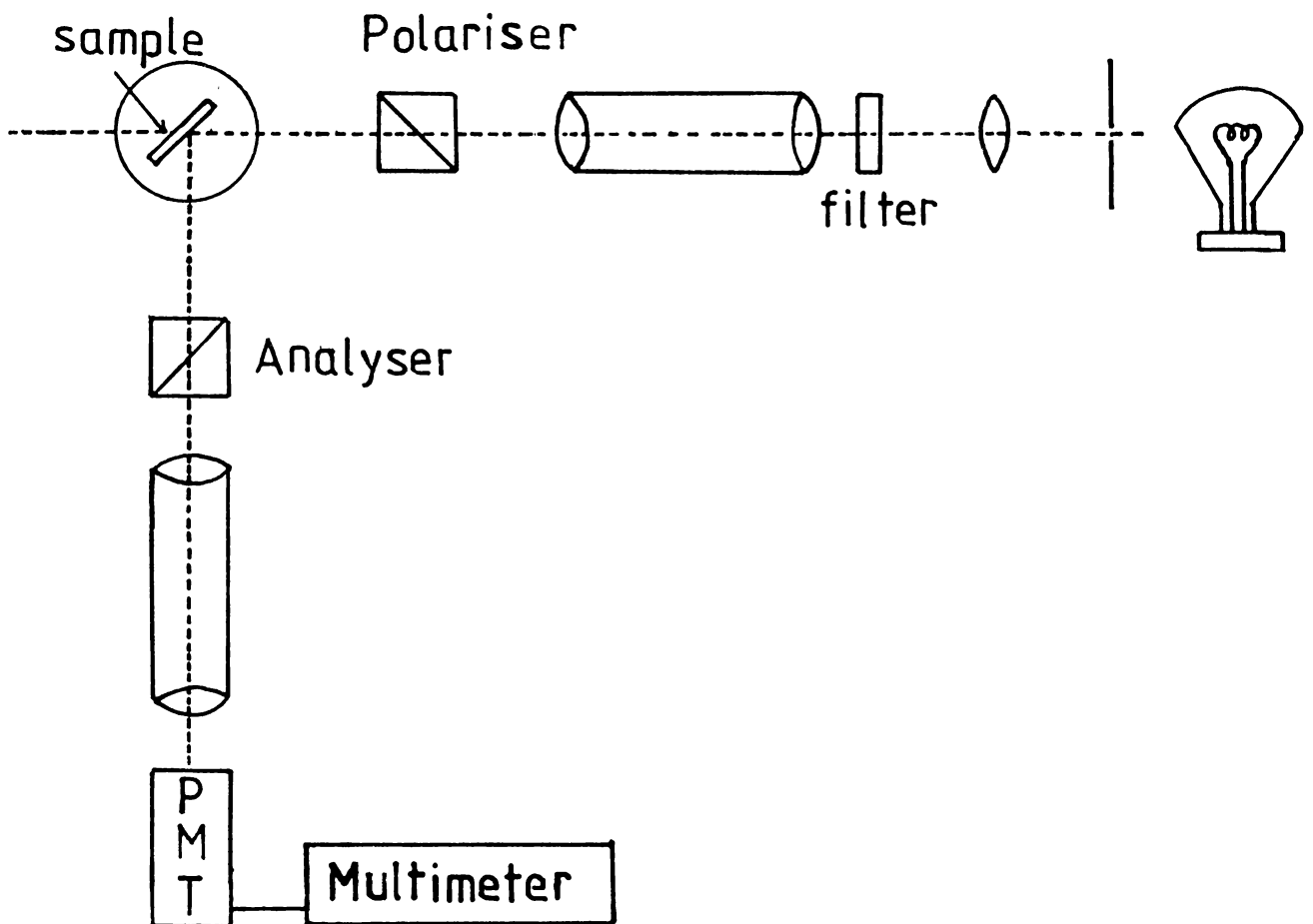


Fig.3.3 Experimental set-up to measure refractive index.

a part of the light is reflected back and part transmitted. In the case of reflection by this ambient-film-substrate system, the overall complex-amplitude reflection coefficient for the p and s polarised incident beams is given by Drude as²⁵

$$R_p = \frac{\gamma_{01p} + \gamma_{12p} e^{-j2\beta}}{1 + \gamma_{01p} \gamma_{12p} e^{-j2\beta}} \quad (3.3)$$

and

$$R_s = \frac{\gamma_{01s} + \gamma_{12s} e^{-j2\beta}}{1 + \gamma_{01s} \gamma_{12s} e^{-j2\beta}} \quad (3.4)$$

where γ_{01s} , γ_{12s} , γ_{01p} , γ_{12p} are the Fresnel reflection coefficients at the ambient-film (0-1) and film-substrate (1-2) interfaces for the s and p polarisations which are defined as follows.

$$\begin{aligned} \gamma_{01p} &= \frac{N_1 \cos \theta_0 - N_0 \cos \theta_1}{N_1 \cos \theta_0 + N_0 \cos \theta_1} \\ \gamma_{12p} &= \frac{N_2 \cos \theta_1 - N_1 \cos \theta_2}{N_2 \cos \theta_1 + N_1 \cos \theta_2} \\ \gamma_{01s} &= \frac{N_0 \cos \theta_0 - N_1 \cos \theta_1}{N_0 \cos \theta_0 + N_1 \cos \theta_1} \\ \gamma_{12s} &= \frac{N_1 \cos \theta_1 - N_2 \cos \theta_2}{N_1 \cos \theta_1 + N_2 \cos \theta_2} \end{aligned} \quad (3.5)$$

β is the phase change experienced by the multiply-reflected beam inside the film on a single traversal between its boundaries and is given by

$$\beta = 2\pi \left(\frac{d_1}{\lambda}\right) (N_1^2 - N_0^2 \sin^2 \phi_0)^{\frac{1}{2}} \quad (3.6)$$

where d_1 is the film thickness and λ the free space wavelength. N_0 , N_1 and N_2 are the complex indices of refraction of the ambient, film and substrate respectively. In most cases, N_0 is real since the medium of incidence is transparent. ϕ_0 , ϕ_1 and ϕ_2 are respectively the angle of incidence in ambient, angle of refraction in the film and at the substrate. These parameters are related by the expression

$$N_0 \sin \phi_0 = N_1 \sin \phi_1 = N_2 \sin \phi_2 \quad (3.7)$$

In order to examine the change of amplitude and phase separately as a plane wave is obliquely reflected from a film covered substrate, the overall complex-amplitude reflection (R_p , R_s) coefficients are written in terms of their absolute values and angles as

$$R_p = |R_p| e^{j\Delta_{rp}} \quad \text{and} \quad R_s = |R_s| e^{j\Delta_{rs}} \quad (3.8)$$

where $|R_p|$, Δ_{rp} represent the amplitude attenuation and phase shift respectively for p-polarised reflected light by the film covered substrate and $|R_s|$, Δ_{rs} the corresponding values for the s polarisation. Thus, in an ambient-film-substrate system, a change of polarisation takes place on reflection due to the difference in amplitude attenuation and phase shift experienced by the p and s components. From measurements of the incident and reflected polarisations, the ratio $\rho_r = R_p/R_s$ of the overall complex-amplitude reflection coefficient of the ambient-film-substrate system for the p and s polarisations is determined. If we express ρ_r in terms of the ellipsometric angles ψ and Δ we have,

$$\tan \psi_r = \left| \frac{R_p}{R_s} \right| \quad \text{and} \quad \Delta_r = \Delta_{rp} - \Delta_{rs} \quad (3.9)$$

ψ_r and Δ_r are also given by²⁶

$$\psi_r = \frac{1}{2} \arccos \left[\frac{(I_{D_1} - 2I_{D_2} + I_{D_3})(I_{D_1} + I_{D_3})}{(I_{D_1} + I_{D_3})^2} \right] \quad (3.10)$$

and

$$\Delta_r = \arccos \left[\frac{(\frac{1}{2} \sin 2\psi)(I_{D_3} - I_{D_1})}{(I_{D_1} + I_{D_3})} \right] \quad (3.11)$$

where I_{D_1} , I_{D_2} and I_{D_3} represent the detected signals at three different sets of polarizer-analyser azimuth angles.

These experimentally determined ψ_r and Δ_r values were correlated with the theoretical values by assigning a suitable value for the unknown film refractive index N_1 in equations (3.3) and (3.4). When the two values match exactly (with minimum deviation between them), that particular value of N_1 has been taken as the refractive index of the film. Matching of the values was checked by using a microcomputer.

Thickness of the films were measured by multiple beam interferometry²⁷. When a partially reflecting surface is placed on a fully reflecting surface to form an air wedge and a monochromatic parallel beam falls on it, interference fringes will be produced. The path difference of the beam from one minimum point to the other is λ where λ is the wavelength of the monochromatic beam. Hence difference in height of the air gap at adjacent minimum points is given by $\lambda/2$. If a step is formed by this film whose thickness is to be measured, the interference fringe pattern will be shifted as shown in fig.3.4A. The thickness of the film can be calculated from the fringe shift 'x' and fringe separation 'y'

using the relation²⁸

$$t = (x/y) \lambda / 2 \quad (3.12)$$

The experimental set up to determine the thickness is presented in fig.3.4B. G is the glass substrate on which the thin film is prepared with a step as shown. In the case of tin oxide films step was made by selective etching process. Since the films are extremely stable and resistant to the usual chemical etching techniques, etching was done by reacting it with nascent hydrogen produced by the reaction of Zn powder with HCl. On the top of this step, a thick aluminium coating was deposited by evaporation method for complete reflection. A partially reflecting glass plate is placed on the substrate to form an air wedge. A mercury lamp with a green filter ($\lambda = 5461\overset{\circ}{\text{A}}$) forms a monochromatic source S. Using a circular aperture A and a lens system L, the beam is made parallel. This beam falls on the wedge G producing a fringe system as shown. The fringes can be clearly seen through a microscope. The fringe separation and fringe shift can be accurately measured with the help of a travelling microscope. By substituting the values in equation (3.12) the thickness of the film can be calculated.

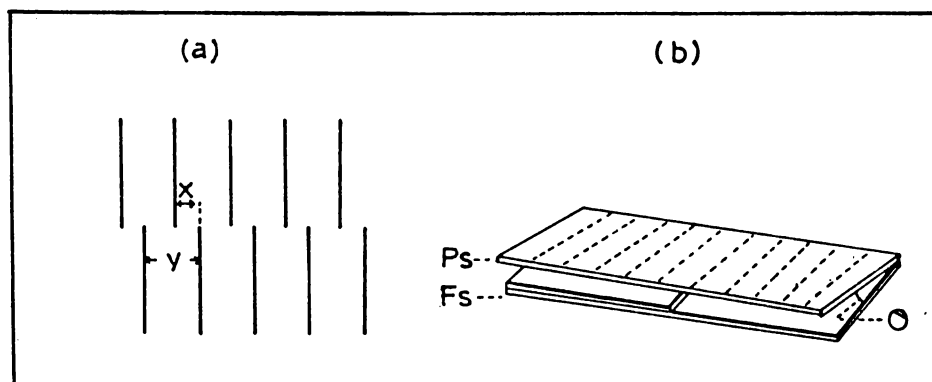


Fig.3.4A

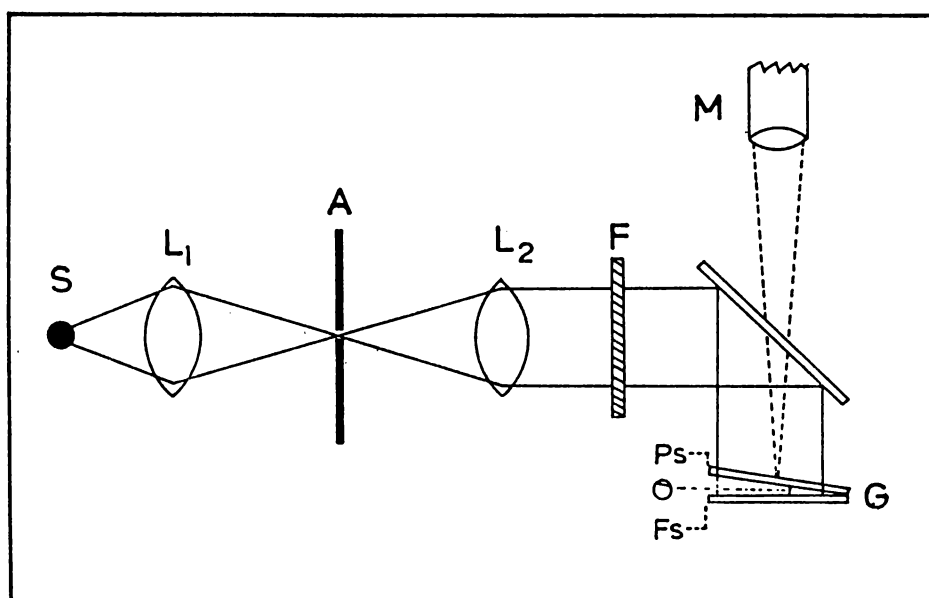


Fig.3.4B

Fig.3.4A Illustration of fringe shift and air wedge.
 x - fringe shift, y - fringe separation,
 PS - partial reflecting surface, FS - fully
 reflecting surface, θ - the wedge angle.

Fig.3.4B Experimental set-up to determine the thickness
 of films.
 S - Hg source, L - lens, F - filter, A - aperture,
 G - glass substrate, M - travelling microscope.

The absorption spectra of these films (figs.3.5A, 3.5B and 3.6C) were recorded using a spectrophotometer (Hitachi Model 330) and the absorbance values at 1060 nm are given in table 3.1. The transmission percentage of three films at 4358A computed using the relation $T_{\lambda} = (1-R_{\lambda})^2 \exp(-\alpha_{\lambda} t)$ is also given. For the other two films, transmission data is not given as these samples were heavily damaged and so absorbance if at all measured would be inaccurate.

By firmly gripping the sample in between two metallic contacts the in-plane resistance R(ohms) of the sample films were measured using a digital multimeter (Tektronix 466 DM 44). The resistivity ρ (ohm cm) was then computed using the relation $\rho = R b d/l$ where b, d and l are the breadth, thickness and length respectively of the thin film samples. Once resistivity is determined, the sheet resistance of these films were calculated using relation $R_{sh} = \text{Resistivity}/\text{thickness of the film}$.

3.80 Results and discussion

The two films prepared by the spray pyrolysis technique reveal variations in their optical and electrical properties brought about by the changes in the deposition parameters. It

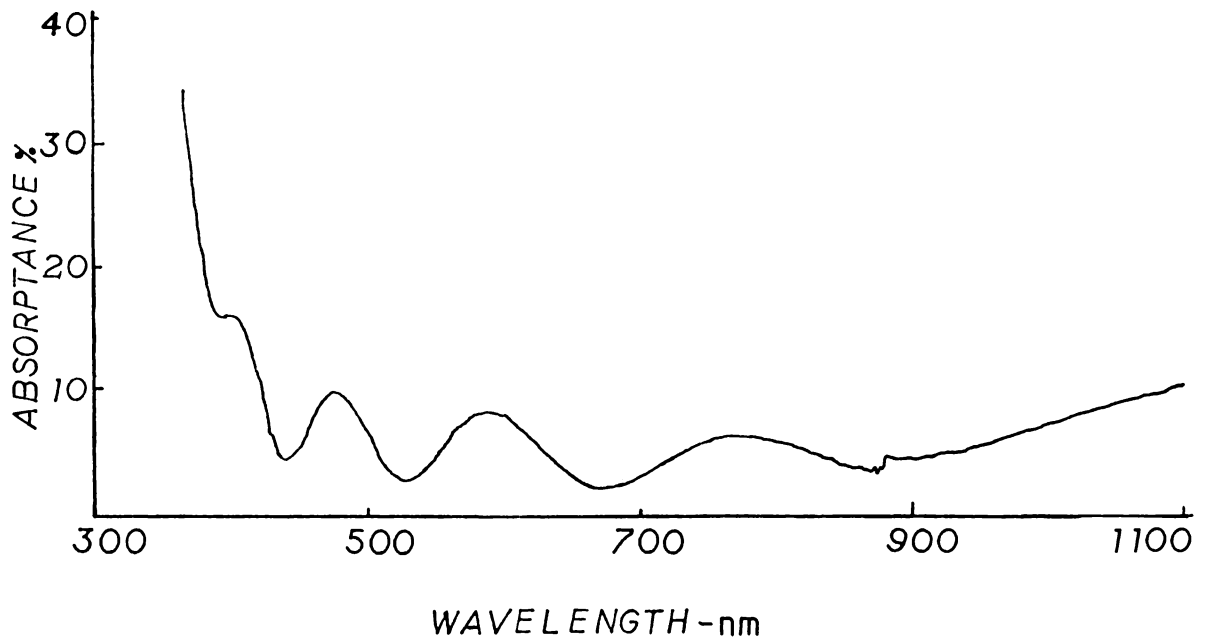


Fig.3.5A Absorption spectrum of indium tin oxide

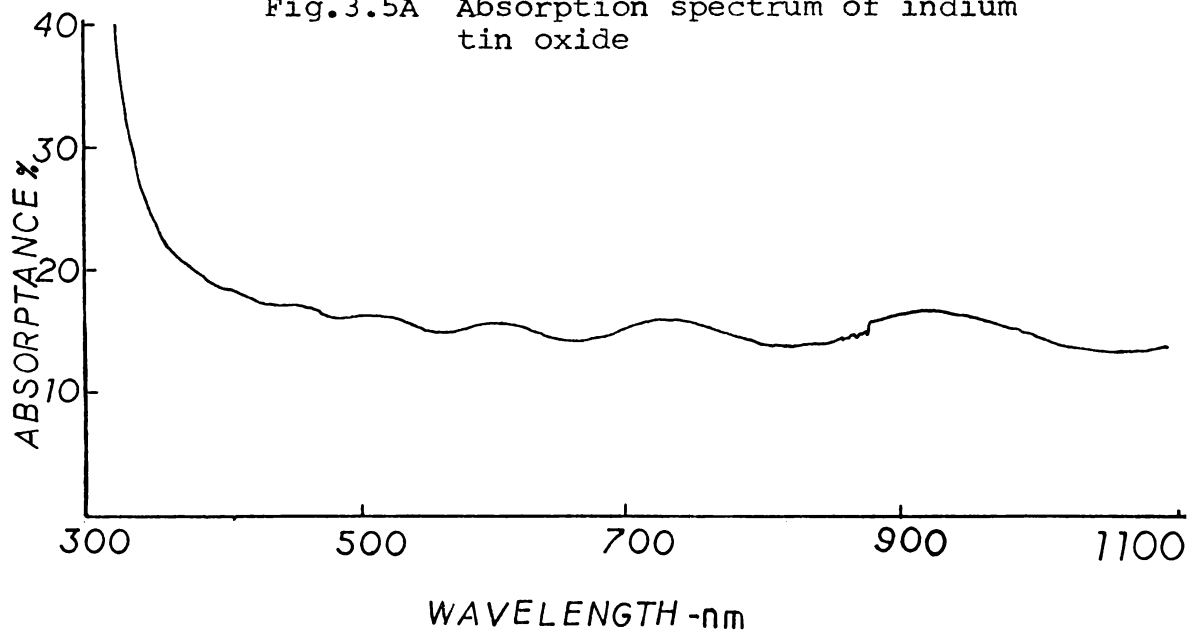


Fig.3.5B Absorption spectrum of tin oxide prepared by CVD method

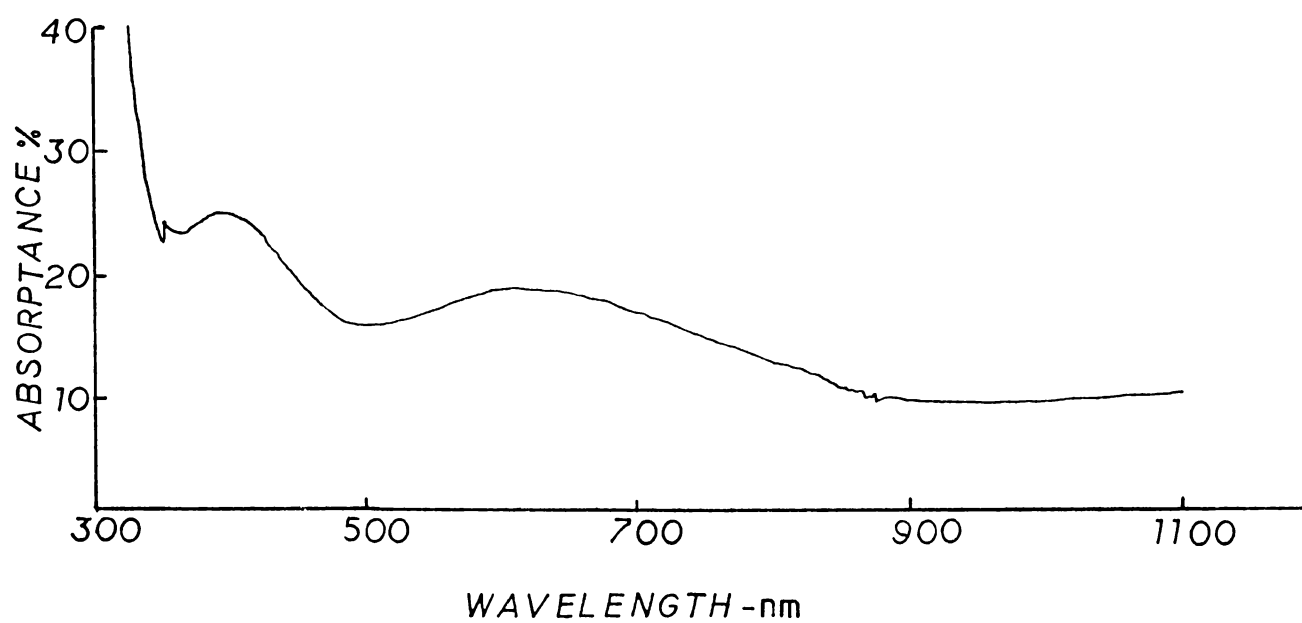


Fig.3.5C Absorption spectrum of tin oxide prepared by SPD method.

Table 3.1 Comparison of the film characteristics of transparent conducting coatings

Film Characteristics	Unit	Tin Oxide		Indium Tin Oxide	
		Coating I ^a	Coating II	Coating I	Coating II
Thickness	nm	151	150	85	200
Resistivity	Ohm cm	0.019	0.007	0.0092	0.00023
Sheet resistance	Ohm/□	1258	467	1082	24.50
Absorptance at 1.06μ	%	--	12.2	4.8	9.0
Absorptance (visible region)	%	10.42 ^b	6.0	14.0	9.0
Refractive index ^c		1.71	1.786	1.7901	1.95 ^d
Damage threshold at normal incidence	J/cm ²	18.2±1.3	14.2±0.6	2.8±0.3	1.29±0.08
Power density at threshold (x 10 ⁹)	W/cm ²	1.21	0.568	0.112	0.052
Laser pulse width	ns	15	25	25	25
Deposition technique		Chemical vapour deposition		Spray pyrolysis method	Reactive rf sputtering
Substrate temperature	°C	400	300	380	200
Transmittance (visible)	%	--	86.2	86.4	--

a data taken from Ref.3

b measured at 435.8 nm

c determined by ellipsometric technique at 435.8 nm

d determined by the position of the interference maxima in R% vs λ spectrum in the visible region.

is observed that an increase in substrate temperature decreases the resistivity as reported by Shanthi et al¹⁸. Coating II has a lower absorptance at 1062 nm which may be attributed to its higher sheet resistance. This in combination with a lower refractive index gives a better damage threshold value. Also, the grain size has been reported to decrease with decrease in deposition temperature¹² and this in turn decreases the refractive index² thereby increasing the threshold value. In this context, a $1/(n^2-1)$ dependence of refractive index on threshold optical electric field has been reported by Bettis et al²⁹ for dielectric coatings and bare dielectrics.

Comparison of ITO films prepared and studied shows that the threshold decreases with absorptance as reported by earlier workers for ITO films⁴ and dielectric films^{30,31,32}. In addition, an inverse dependence of threshold on thickness is also observed as in the case of dielectric films³³.

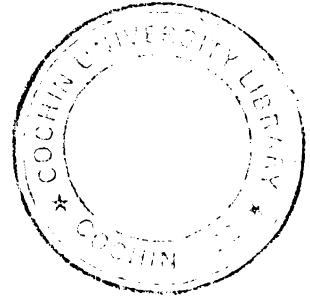
In the case of CVD films, present threshold values are lower than those reported earlier⁵. Even though coatings I and II have the same thickness, the latter has a lower resistivity and hence a lower sheet resistance. It has been pointed out by Pawlewicz et al² that films with lower sheet resistance has a higher absorptance which could lead to a lower damage

threshold. Moreover, an inverse dependence of threshold on refractive index is found to hold good as in the case of films deposited by the spray pyrolysis technique.

Comparison of the coatings reveals that spray pyrolysis is a technique which offers great flexibility in terms of their electrical and optical characteristics depending on deposition parameters. Variation in these characteristics alters the damage threshold of these films. This adaptability in the threshold value permits mutual trade-off between the desired characteristics thereby allowing a proper selection of coatings for low and high power applications. Thus, transparent films with high damage thresholds can be obtained at the expense of conductivity or highly conducting films with lesser transmission can be selected if the damage resistance requirement is lower. Though rf sputtered ITO films provide the best conductivity, they have the lowest thresholds as compared to CVD and SPD films. In the case of CVD films, very high damage thresholds are seen even though their electrical characteristics are not as good as those of ITO films. Also, the uniformity of the CVD films are found to be inferior to those of SPD and rf sputtered films.

An inverse dependence of damage threshold on absorptance and film thickness has been observed for SPD

and rf sputtered films. This agrees well with similar trends observed by earlier workers for ITO films (in the case of absorptance alone) and a number of dielectric coatings and is suggestive of the damage mechanism to be an impurity dominated one.



REFERENCES

1. K.L.Chopra, S.Major and D.K.Pandya, Thin Solid Films, 102, 1 (1983).
2. W.T.Pawlewicz et al, NBS Special Publication 568, Proc. of the symposium on laser-induced damage in optical materials, p.359 (1980).
3. L.L.Steinmetz et al, Appl.Opt. 12, 1468 (1973).
4. W.T.Pawlewicz et al, Appl.Phys.Lett. 34, 196 (1979).
5. N.Subhash and K.Sathianandan, J.Appl.Phys. 54, 424 (1983).
6. T.Nishino and Y.Hamakawa, Japan J.Appl.Phys. 9, 1085 (1970).
7. W.Spence, J.Appl.Phys. 38, 3767 (1967).
8. M.Mizhuhashi, Thin Solid Films, 70, 91 (1980).
9. A.Balasubramonian, M.Radhakrishnan and C.Balasubramanian, Thin Solid Films, 91, 71 (1982).
10. R.R.Mohta and S.F.Vogel, J.Electrochem.Soc. 121, 394 (1974).
11. R.P.Howson, J.N. Avaritsiotis, M.I.Ridge and C.A.Bishop, Thin Solid Films, 63, 163 (1979).
12. T.Muranoi and M.Furunkoshi, Thin Solid Films, 48, 309 (1978).
13. H.S.Soni, S.D.Sathye and A.P.B.Sinha, Indian J.Pure and Appl.Phys. 21, 197 (1983).

14. H.Dislich and E.Hussmann, Thin Solid Films, 77, 129 (1981).
15. Z.Porada, E.Schabowska and T.Piech, Acta Physica Polonica,
A 57, 267 (1980).
16. H.Kenko and K.Miyake, J.Appl.Phys. 53, 3629 (1982).
17. B.J.Baliga and S.K.Ghandi, J.Electrochem.Soc. 123, 941 (1976).
18. E.Shanthi, V.Dutta, A.Banerjee and K.L.Chopra, J.Appl.Phys.
51, 6243 (1980).
19. S.Muraleedharan Pillai, Ph.D.thesis, Cochin University (1984).
20. G.Blandenet et al., Thin Solid Films, 77, 81 (1981).
21. K.Sreenivas, Suderson Rao, Abhai Man Singh and K.Subhash
(To appear in J.Appl.Phys.).
22. O.Caporaletti, Sol.Energy Mater. 7, 65 (1982).
23. W.W.Molzen, J.Vac.Sci.Technol. 12, 99 (1975).
24. N.L.Boling and G.Dube, Damage threshold studies of glass
laser materials, Final Technical Report, Owens-Illinois
Inc. Toledo, Ohio (1974).
25. P.Drude, Ann.Phys.Chem. 39, 481 (1890).
26. R.M.A.Azzam and N.M.Bashara, Ellipsometry and polarised
light, North-Holland Publishing Co. p.256 (1977).
27. S.Tolansky, Surface microtopography, John Wiley & Sons Inc.
New York (1960).

28. Robert W.Berry, Peter M.Hall and M.T.Harris, Thin film technology, Van Nostrand Rheinhold, New York, p.160 (1960).
29. J.R.Bettis, A.H.Guenther and R.A.House II, Opt.Lett. 4, 256 (1979).
30. C.K.Carniglia, J.H.Apfel, T.H.Allen, T.A.Tuttle, W.H.Lowdermilk, D.Milam and F.Rainer, NBS Special Publication 568, Proc.of the Symposium on laser-induced damage in optical materials, p.377 (1980).
31. W.H.Lowdermilk, D.Milam and F.Rainer, NBS Special Publication 568, Proc.of the Symposium on laser-induced damage in optical materials, p.391 (1980).
32. T.W.Walker, A.H.Guenther, C.G.Fry and P.Nielson, NBS Special Publication 568, Proc.of the Symposium on laser-induced damage in optical materials, p.405 (1980).
33. T.W.Walker, Ph.D Thesis, Part II p.21 (1979) , Air Force Institute of Technology, Ohio.

Chapter 4

DAMAGE MEASUREMENTS ON THIN FILMS OF POLYACRILONITRILE (PAN), DIELECTRIC AND METALLIC FILMS WITH AND WITHOUT AN UNDERCOAT OF PAN

Section A - Damage Measurement on Polyacrilonitrile

4.10 Introduction

Polymer materials are becoming important as optical material elements [polymethylmethacrylate (acrylic) and polystyrene] which are frequently used in lens fabrication¹. Extensive use of polymer materials in various branches of technology, including optical instrumentation, makes it desirable to study the possibility of using these materials in lasers too. In particular, various optical components like prisms, lenses and deflectors as well as specific laser components like active elements containing lasing dyes and bleachable filters for Q-switching can be fabricated using transparent polymer materials. Therefore, it would be of considerable interest to investigate the optical strength of polymer materials which, because of their special structure and thermoelastic properties different from those of the

conventional materials such as glasses and crystals, may have some important distinguishing characteristics. One characteristic feature of polymer materials which distinguishes them from the conventional materials is the higher optical strength of the surfaces of polymers compared with their bulk². This is very important from the practical point of view because it is the surface strength of transparent insulators which is usually the limiting factor of their use in laser systems. Another characteristic feature of polymer materials is the existence of a strong accumulation effect so that microdamage and its growth to macroscopic dimensions during successive laser irradiation are observed at intensities much lower than the damage threshold. This is one of the main obstacles to the extensive use of transparent polymers in laser systems. However, it has been shown³ that some of the transparent polymers with an optical strength comparable with that of the crystals and glasses can be highly competitive with these traditional materials in the fabrication of various optical components of lasers. The mechanism of nucleation of microdamage initiated by absorbing defects is dominated by the molecular characteristics of modifying additives present in polymers. Moreover, the growth of

damage from micro level to macroscopic dimensions is influenced greatly by the viscoelastic properties of the polymer matrix³. These ideas about the mechanism of laser damage of transparent polymers are used in suggesting ways of increasing their optical strength.

4.11 Preparation of polyacrylonitrile films

It has been reported that⁴ depending on the methods of preparation, the physical and electrical properties will vary in polymer thin films. Different methods have been suggested to prepare polymer films; among them plasma polymerisation⁵ is one of the popular methods on account of the desirable qualities of these films such as good adhesion to substrates, pin-hole-free nature and excellent electrical and mechanical properties⁶. Also, this method is more economical due to the optimum use of monomer, high efficiency of polymerisation and absence of any type of catalyst. For the preparation of polymers, the plasma of the monomer vapour can be generated by different ways⁷. Low frequency glow discharge using 50 Hz AC is the frequently employed technique among them.

In this method the discharge chamber with the substrate set at its central part is evacuated to 10^{-5} torr.

Then the monomer vapour is introduced into the system from the monomer reservoir in a controlled manner using a needle valve. When a pressure of 10^{-2} torr is obtained the voltage and the pressure are simultaneously adjusted to obtain a discharge condition suitable to the formation of a good polymer film.

The rate of growth of the polymer depends on the amount of the monomer vapour present in the chamber and on the current flowing across the electrodes. The amount of monomer vapour present in the system is proportional to the effective pressure in the polymerisation chamber. For a constant voltage the current across the electrode depends on the monomer vapour pressure. Hence the main parameter for the rate of growth of polymer film is the current across the electrodes. It is also noted that a minimum voltage is required to produce the glow-discharge and the threshold voltage depends on the inter-electrode spacing. Thus, the growth rate of the film increases with the pressure. For a fixed pressure, the thickness of the film is also found to be proportional to the square of the current. Therefore, it can be concluded that the growth rate is proportional to the electrical power transferred to the system. The electrical power is directly

transferred to the monomer molecules to break the bonds which have minimum binding energy. When a voltage is applied to the electrodes, the ions and electrons are accelerated towards the electrodes. The accelerated ions collide with monomer molecules and due to the impact the energy is transferred to the monomer molecules generating the radicals of the monomer. These radicals combine together to form a polymer chain. Certain accelerated ions will collide with the electrodes raising the temperature of the electrodes, thereby dissipating a part of the energy.

In the present investigation, polyacrylonitrile (PAN) films are prepared directly from its monomer vapour by low frequency (50 Hz AC) plasma polymerisation process. The discharge chamber with the clean substrate set at the central part is evacuated to 10^{-2} torr. Then the monomer gas is introduced into the chamber from the monomer reservoir in a controlled manner. When the pressure of the monomer gas rises to 2×10^{-1} torr, the output of a step-up transformer is directly given to the two electrodes. In the present study the electrode current was maintained at 60 mA but the time of deposition varied from 10 to 28

minutes for the three thicknesses studied. The inter-electrode distance was kept 3 cms across which a voltage of 680 V was maintained.

4.12 Damage threshold measurement

The experimental set up and the method of determining the damage threshold of the PAN coatings were the same as described in the previous chapter. Absorption of the films were determined using spectrophotometric method (Hitachi Model 330) and the thickness by the multiple beam interferometric technique.

4.13 Results and discussion

The threshold energy density computed for the three thicknesses are listed in table 4.1. As can be seen from the table, the threshold energy density increases with thickness. Even though the percentage absorptance increases with thickness in the visible region, it remains more or less constant at a low value at the laser irradiation wavelength of 1060 nm. In the case of transparent dielectric films a decrease in threshold value is observed with increase in film thickness⁸. The constant absorptance at 1060 nm

Table 4.1

Threshold values of PAN films

No.	Characteristics	Samples of polyacrylonitrile		
		I	II	III
1	Thickness (nm)	105	200	370
2	Absorptance % at 500 nm	14	27	47
3	Absorptance % at 1060 nm	4	3	3
4	Damage threshold (J/cm ²)	10.71±0.84	14.71±1.30	26.00±2.08

for the PAN films of different thicknesses and the increase in threshold with thickness for these films rule out the role of impurities/defects in initiating breakdown in the PAN films.

One of the characteristic features of a polymer material which distinguishes it from other transparent insulators is the higher optical strength of the surface^{9,10}. This has been explained in terms of the viscoelastic properties and the molecular characteristics of the monomer¹¹. The experimentally obtained high threshold value of $26\text{J}/\text{cm}^2$ for the PAN coating for the maximum thickness studied, and the increase in threshold with thickness can therefore be attributed to the influence of viscoelastic properties of the surface layer of the polymer material and to the molecular characteristics of the monomer.

A low value of absorptance at 1060 nm, an increase in threshold with thickness and very high damage thresholds compared to the dielectric films make the polyacrylonitrile film a good candidate in high energy laser systems. In the case of dielectrics as one goes from lower to higher thickness the damage threshold decreases. This is a serious drawback

when these films having high thicknesses are to be used for high energy applications. From the present studies it can be concluded that PAN films, especially of higher thicknesses, can effectively replace some of the dielectric films in high energy laser systems.

Section B - Damage Threshold Measurement on Dielectric Films with and without an Undercoat of PAN

4.20 Introduction

The reflectance for a quarter-wave film is given by¹²

$$R = \frac{(n_T - n_1)^2}{(n_T + n_1)^2} \quad (4.1)$$

where n_T is the refractive index of substrate and n_1 the refractive index of the film. The reflectance is reduced to zero if $n_1 = \sqrt{n_T}$. Such coatings are termed as antireflection films. Even though magnesium fluoride, with a refractive index of $n_1 = 1.35$, does not exactly satisfy the above requirement for ordinary glass with $n_T \approx 1.5$, the reflectance of glass coated with a quarter-wave layer of this material is reduced

to about one percent, which is one fourth that of uncoated glass. This can result in a considerable saving of light in the case of optical instruments having many elements, such as high-quality camera lenses that may have as many as five or six components, i.e., ten or twelve reflecting surfaces. By using two layers, one of high index and other of low, it is possible to obtain zero reflectance (at one wavelength) with available coating materials. With three suitably chosen layers the reflectance can be reduced to zero for two wavelengths and can be made to average less than 1/4 percent over almost the entire visible spectrum.

Thin film high reflective (HR) coatings consist of an odd number of quarter-wave thick layers, alternating high and low index materials. The first and last layers are the high-index material. High reflector coatings usually have a higher damage threshold than other types of coatings commonly found in high-energy laser systems, such as antireflection (AR) coatings and polarising beam splitters. Further, investigation of the damage characteristics of high reflectors can provide direct information about the damage resistance of the coating and coating materials without the complicating factors arising from the substrate on which the

coating is deposited. In a typical HR design, the laser energy is concentrated in the outermost layers of the coating, with very little energy penetrating to the substrate interface. Thus, the observed laser damage should occur in the outer layers, and should reflect the properties of the coating materials¹³. In contrast, the interface between an AR coating and its substrate receives the full energy of the laser pulse. This interface is a natural weak link in the coating system. It can be affected by the polishing process, the surface finish, the cleaning process and the residual surface contamination before and during the coating process. Thus, whereas damage to HR coatings occur in the outermost layers, AR coating damage usually nucleates at the substrate interface¹⁴. Two additional facts are consistent with the assumption that the interface region has significantly larger absorption than the surrounding coating and substrate material.

1. Although the standing wave electric field peak intensity in AR coatings is less than in HR coatings, AR damage thresholds are less than HR thresholds. This result suggests that the substrate interface, which is irradiated in AR but not in HR coatings, plays an important role.

2. AR coating damage threshold do not depend strongly on the absorption average over the coating thickness. This indicates that absorption is not uniform; rather it is high in some places and low in others.

The low damage threshold of antireflection coatings makes them a limiting factor in the achievement of large laser powers for laser fusion. The damage threshold for AR coating is roughly half that of high reflectors in spite of the fact that the electric field intensities in the two types of coatings indicate that the AR coatings should have a higher damage threshold¹⁵.

It has thus become important to try to find ways of increasing the thresholds of these coatings, which are often the 'Weak Link' in high energy laser systems. Many factors have been studied in relation to ^{the} damage ^{on} coatings for fusion laser systems. These include stress, absorption, index of refraction and electric field distribution within the coatings. Increase in threshold using laser annealing and neutral solution treatment has been reported^{16,17}. However, one simple method of improving the damage resistance of coatings, which has proven to be effective at 1060 nm is the addition of a low-index layer having a half wave optical thickness^{13-15,18-20}.

This technique has been demonstrated to be effective at 248 nm also, the KrF laser wavelength²¹. The additional half wave layer takes two different forms, depending on the coating type. In the case of a high reflector (HR) where the laser energy is concentrated in the outer part of the coating, the layer is an overcoat, added to the top of a standard quarter wave reflector stack^{13,18}. For an AR coating, where the energy penetrates to the substrate, an undercoat barrier layer is added^{14,18}. The effect of these layers on 1060 nm coatings has been to raise the damage threshold by approximately 50 percent for both HRs and ARs¹⁸. In the present investigation, damage threshold studies on ZnS and MgF₂ monolayer films have been carried out. In the case of the latter the investigations have been extended with an undercoat of PAN.

4.21 Preparation of magnesium fluoride (MgF₂) and zinc sulphide (ZnS) films

The vacuum evaporation technique was used for the preparation of magnesium fluoride and zinc sulphide films. During the time of coating, the pressure was always maintained at 2×10^{-5} torr. As usual in the vacuum evaporation technique, this low pressure was achieved in two stages. Using a rotary

pump the pressure was lowered to 10^{-2} torr and later for still lower pressure a diffusion pump was used. When the pressure was brought down (2×10^{-5} torr) the required material was evaporated by heating it suitably. Weighed pellets of these samples obtained from M/s. Balzers were taken in a molybdenum boat. The distance between the heating source and the substrate was kept at about 20 cms. The required thickness of the films was obtained by evaporating calculated quantity of the material. The amount of the sample required was calculated using the expression $m = \pi \rho d^2 t$, considering the material to be a small plane source. In this expression, m is the mass of the material, ρ is the density of the material, d is the distance of the source from the substrate and t is the required thickness. Mass of the material was measured accurately using a chemical balance. The deposition rate was about 250 Å/minute. Among each set of films prepared, one film was made with a sharp edge (obtained by keeping the edge of a mica sheet on the substrate). This film was over-coated with silver or aluminium and the thickness of the step thus formed was measured by the method of multiple beam interferometry as described in Chapter 3. Here, it was found that the thickness variation from the calculated value was always within $\pm 50\text{Å}$. Aluminium or silver was deposited by

the same vacuum evaporation process. In this case the material to be evaporated was taken inside a tungsten helix.

4.22 Damage threshold measurement

Laser damage threshold values are usually specified in terms of incident energy density or power density. However, Crisp et al²² have shown that the correct quantity in specifying the damage threshold in the short pulse regime (picosecond and nanosecond) is the electric field associated with the laser pulse. This was confirmed later by De Shazer et al²³ and Newnam and De Shazer²⁴. The electric field at the surface of an uncoated material with refractive index n_g or for a $\lambda/2$ thick film deposited on it is given by²⁵

$$E \text{ (V/m)} = \frac{38.8 \sqrt{S \text{ (W/m}^2\text{)}}}{n_g + 1} \quad (4.2)$$

for $\lambda/4$ or $3\lambda/4$ thick films of refractive index n_f , the electric field at the film surface is

$$E \text{ (V/m)} = \frac{38.8 n_g \sqrt{S \text{ (W/m}^2\text{)}}}{n_g + n_f^2} \quad (4.3)$$

As $n_f \rightarrow n_g$, the expressions (4.2) and (4.3) coalesce and if the field is indeed the threshold quantity one would expect the variation in threshold power density with film thickness to vanish.

The experimental set up and the method of determining the damage threshold were the same as described in previous sections. The thickness of the films were measured by the multiple beam interferometric technique. Variation of the damage threshold of MgF_2 films with thickness is given in fig.4.1.

4.23 Results and discussion

Damage threshold values obtained in the case of MgF_2 and ZnS are given in table 4.2A. Magnesium fluoride films of three thicknesses were studied. In one case the film was baked at $100^\circ C$ and was then damage tested. Results show that baking of the coating after the deposition has no influence on the damage threshold. The highest threshold value ($37 J/cm^2$) observed is for the $\lambda/4$ (at 1060 nm) thick film. As reported by earlier workers the damage threshold decreases with increase in film thickness in the case of

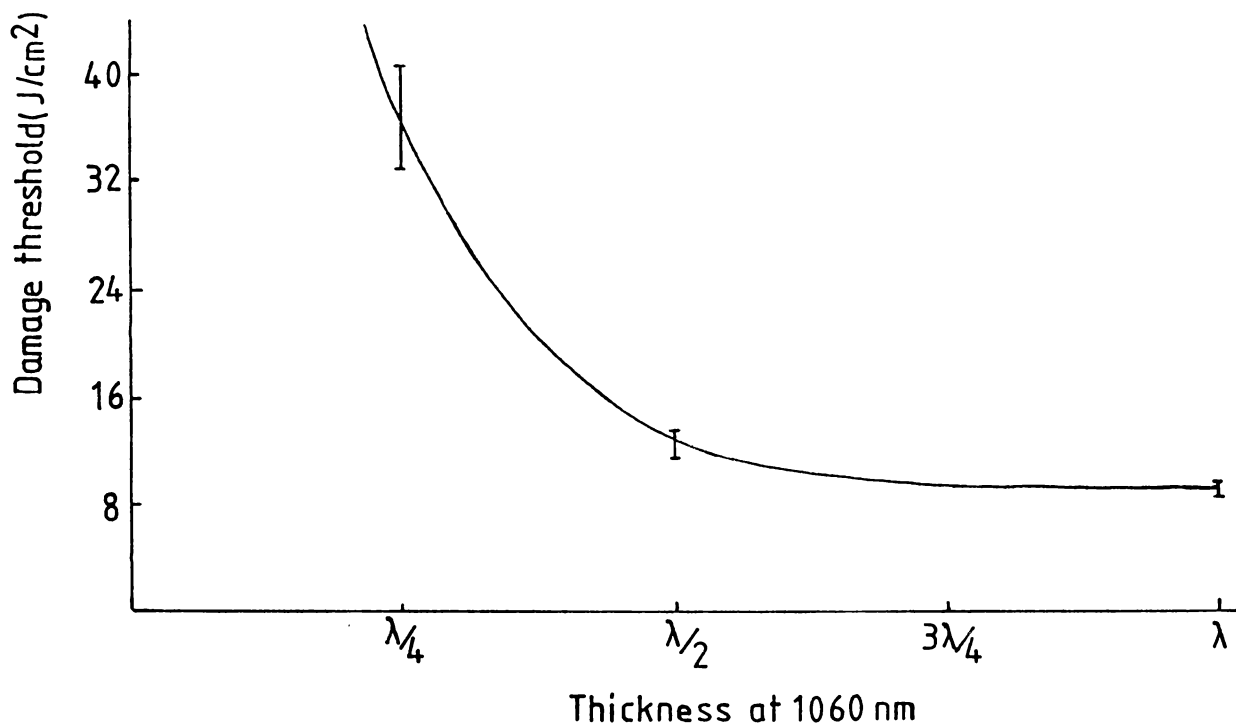


Fig.4.1 Variation of damage threshold with thickness for MgF₂ films.

Table 4.2A
 Threshold values of MgF_2 and ZnS

No.	Sample film	Thickness (nm)	Damage threshold		
			J/cm^2	W/cm^2	MV/cm
1	Magnesium fluoride	273	37.0 ± 4.14	1.48×10^9	0.679
2	Magnesium fluoride	530 ± 5	11.75 ± 0.91	0.47×10^9	0.334
3	Magnesium fluoride (baked)	530 ± 5	11.36 ± 0.97	0.45×10^9	0.327
4	Magnesium fluoride	1060 ± 5	8.95 ± 0.69	0.36×10^9	--
5	Zinc sulphide	400 ± 5	5.4 ± 0.42	0.22×10^9	--

MgF₂ films⁸. This is suggestive of the influence of impurities in initiating the damage in these materials.

Table 4.2B gives the damage threshold values for $\lambda/2$ (at 1060 nm) thick MgF₂ films with PAN as an undercoat. Results show that the threshold of MgF₂ increases by about 50 percent when PAN was given as an undercoat. This enhancement is only observed when the threshold of the PAN undercoat is greater than that of the MgF₂. If the threshold of PAN is less than that of MgF₂, (by a suitable choice of the PAN thickness) a decrease in threshold is observed for the MgF₂ films having an undercoat of PAN. These results confirm the earlier experimental indications about the vulnerability of substrate/coating interface¹⁴. The increase in threshold of MgF₂ with an undercoat of PAN may be because of the better adhesion of MgF₂ coating to PAN film having a high damage threshold. This is further substantiated by the fact that the MgF₂ of the same thickness damages at a low level--even at a lower level than that of MgF₂ alone--when PAN film of lower damage threshold was given as an undercoat.

Section C - Laser-Induced Damage Studies on Gold Coatings with and without an Undercoat of PAN

4.30 Introduction

For a metal to be a good reflector, it must possess

Table 4.2B Threshold values of MgF_2 with an undercoat of PAN

No.	Sample film	Thickness (nm)	Damage threshold J/cm^2
1	Magnesium fluoride	530 ± 5	11.75 ± 0.91
2	Polyacrylonitrile-I	105	10.71 ± 0.84
3	Polyacrylonitrile-III	370	26.00 ± 2.08
4	Magnesium fluoride + Polyacrylonitrile-I	$(530 \pm 5) + 105$	8.84 ± 0.66
5	Magnesium fluoride + Polyacrylonitrile-III	$(530 \pm 5) + 370$	17.20 ± 1.45

An attempt on the damage threshold measurement of quarter-wave thick MgF_2 films with an undercoat of PAN was abandoned because of the difficulties associated with the reproduction of the experiment under the same experimental conditions.

a plasma frequency large compared with the frequency of interest and must not have interband transitions in the region of interest. In the visible spectral region, the plasma frequencies of metals are comparable with the frequency of the light. This leads to a lower reflectance and stronger absorption of the laser radiation than at IR frequencies. As a result, most of the laser damage measurements on metallic reflectors like Cu, Ag and Au have been carried out at 10600 nm (CO₂ laser wavelength)^{26,27}. Some of the damage measurements have also been reported at 1060 nm²⁸ and 492 nm²⁹. It is currently accepted that the best maximum reflectors for 10600 nm are made from uncoated, oxygen-free, high conductivity copper blanks which have been diamond-turned³⁰. This combination usually produces reflectivities of about 99.5 percent and laser-induced damage threshold figures in excess of 10 MW/mm². Due to the oxidation of the copper surface³¹ these mirrors degrade very quickly, causing increased absorptivity which leads to laser damage. For this reason, copper substrates are usually coated to prevent the formation of an oxide layer. Of the various coatings that have been tried, the best is one which is fabricated by plating gold onto diamond-turned copper substrates. This method typically produces mirrors which have reflectivities of 99 percent and laser-induced damage threshold power density figures of about 8 MW/mm² (60 ns).

4.31 Damage threshold measurement of Au films

In the present investigation, damage threshold measurement on gold film deposited on glass substrate is reported. The purpose of the investigation is to compare the relative damage threshold values of the dielectric (MgF_2), polymer (PAN) and metallic (Au) coatings at 1060 nm using the Nd:glass laser emitting 25 ns (FWHM) pulses. In order to check the influence of a polymer base on gold films, damage studies on gold with an undercoat of PAN was also carried out. The experimental set up for these studies were the same as described previously. Gold films were deposited on glass substrates by the vacuum evaporation method and the PAN coatings were made by the plasma polymerisation process. The thickness of the films deposited were determined by the multiple beam interferometric technique.

4.32 Results and discussion

Results of the investigations are presented in table 4.3. Comparison of the results show that gold coating have a low damage threshold value compared to the polymer coatings or dielectric coatings at the laser wavelength of 1060 nm. This can be explained in terms of the high absorption

Table 4.3 Threshold values of gold coatings with and without an undercoat of PAN

No.	Characteristics	Samples		
		Gold	PAN	PAN + Gold
1	Thickness (nm)	270 ± 5	160	$160 + (270 \pm 5)$
2	Damage threshold (J/cm^2)	1.24 ± 0.07	10.16 ± 0.73	1.22 ± 0.07

of gold coatings at this wavelength and the low yield stress of this material. In order to check the influence of a polymer base, gold was damage tested with an undercoat of PAN. Comparison of the threshold of the gold coating with that of gold on a polyacrylonitrile base (having a high damage threshold) does not show any variation in the threshold value. Preliminary studies conducted on the adhesion of gold films on PAN has shown that the adhesion of gold coatings on PAN is poor. Therefore, it is concluded that the results obtained may be because of the poor adhesion of gold films on PAN.

REFERENCES

1. D.Milam, Appl.Opt. 16, 1204 (1977).
2. A.S.Bebchuk, D.A.Gramov and V.S.Nechitailo, Sov.J.Quantum Electron. 6, 986 (1976).
3. K.M.Dyumaev, A.A.Manenkov, A.P.Maslyukov, G.A.Matyushin, V.S.Nechitailo and A.M.Prokhorov, Sov.J.Quantum Electron. 13, 503 (1983).
4. Shinichi Takeda, J.Appl.Phys. 47, 12, 5480 (1976).
5. M.Yesuda, M.O.Bugarner and J.J.Hillman, J.Polym.Sci. 17, 1519 (1973).
6. S.Morita, G.Sawa, T.Mizutani and M.Ieda, J.IEEE (Japan), 92-A, 65 (1972).
7. Suhr, Techniques and applications of plasma chemistry, ed.J.R.Hollahan and A.T.Bell, Wiley Pub.Co. (1974).
8. T.W.Walker, Ph.D.thesis (1979), **Air force Inst.of Techgy., Ohio.**
9. A.A.Manenkov et al., Sov.J.Quantum Electron. 10, 347 (1980).
10. A.S.Bebchuk et al., Sov.J.Quantum Electron. 6, 986 (1976).
11. K.M.Dyumaev et al., Sov.J.Quantum Electron. 13, 503 (1983).
12. G.R.Fowles, Introduction to modern optics, p.86, Holt, Rinehart & Winston Inc., New York (1975).

13. C.K.Carniglia, J.H.Apfel, T.H.Allen, T.A.Tuttle,
W.H.Lowdermilk, D.Milam and F.Rainer, NBS Special
Publication 568, Proc. of the Symposium on laser-
induced damage in optical materials: 1979, p.377
(1980).
14. C.K.Carniglia, J.H.Apfel, G.B.Carrier and D.Milam,
NBS Special Publication 541, Proc. of the Symposium
on laser-induced damage in optical materials: 1978,
p.218 (1978).
15. J.H.Apfel, NBS Special Publication 509, Proc. of the
Symposium on laser-induced damage in optical
materials: 1977, p.251 (1977).
16. J.E.Swain, D.Milam and W.H.Lowdermilk, Appl.Phys.Lett.
41, 782 (1982).
17. L.M.Cook and K.Mader, Laser focus, March 1983.
18. C.K.Carniglia, Thin Solid Films, 77, 225 (1981).
19. F.Rainer, D.Milam and D.Lowdermilk, NBS Special Publication
(1981).
20. C.K.Carniglia and J.H.Apfel, J.Opt.Soc.Am. 70, 523 (1980).
21. T.T.Hart, T.L.Lichtenstein, C.K.Carniglia and F.Rainer,
Lawrence Livermore Laboratory Report UCRL-86711 (1982).

22. M.D.Crisp et al., Appl.Phys.Lett. 21, 364 (1972).
23. L.G.DeShazer et al., Study of laser-irradiated thin films, University of Southern California (1973).
24. B.E.Newnam and L.G.De Shazer, NBS Special Publication 372, p.123 (1972).
25. J.R.Bettis, Laser-induced damage as a function of dielectric properties at 1060 nm, Ph.D. dissertation, Report AFWL-TR-76-61, Kirtland AFB, New Mexico 87117.
26. J.O.Porteus, D.L.Decker, D.J.Grandjean, S.C.Seitel and W.N.Faith, NBS Special Publication 568, Proc. of the Symposium on laser-induced damage in optical materials : 1979, p.175 (1980).
27. J.O.Porteus, D.L.Decker, J.L.Jernigan, W.N.Faith and M.Bass, IEEE J.Quantum Electron, QE-14, 776 (1978).
28. J.O.Porteus, D.L.Decker, W.N.Faith, D.J.Grandjean, S.C.Seitel and M.J.Soileau, IEEE J.Quantum Electron. QE-17, 2078 (1981).
29. C.D.Marrs, W.N.Faith, J.H.Dancy and J.O.Porteus, Appl. Opt. 21, 4063 (1982).
30. S.K.Sharma, R.M.Wood, and R.C.Ward, NBS Special Publication 509, p.183 (1977).
31. J.S.Hartman, Appl.Opt. 20, 4062 (1981).

TWO-PHOTON EXCITED FLUORESCENCE IN RHODAMINE 6G

5.10 Introduction

Two-photon absorption is the simultaneous absorption of two photons of different or the same frequency. This can be thought of as the effect of one of the electromagnetic fields modulating the energy spectrum of matter in such a way that a second photon can be absorbed while the modulation lasts. There are several features of two-photon absorption that make it a very worthwhile tool. It is relatively easy to find the absorption properties in dense matter using two-photon than one-photon spectroscopy. While one is limited to the exploration of a small subset of the energy levels of a system using one-photon spectroscopy, allowed transitions in two-photon absorption cover a much wider range of symmetry types, often those that are inaccessible to allowed one-photon absorption. In one-photon absorption, polarisation studies in gases and liquids are useless because of an averaging out of polarisation effects. But, two-photon spectroscopy in solids, liquids and gases can almost uniquely, identify the symmetry of energy levels of matter in experiments where the

directions of the polarisation vectors of both light beams can be independently varied. Two-photon absorption is different from two-step excitation in which one photon first populates an energy level of a system and a second photon then makes the final step to a higher energy level.

The possibility of two-photon absorption was first outlined theoretically by Goeppert-Mayer in 1931¹. But, the world had to wait until 1961 when Kaiser and Garrett² demonstrated for the first time the experimental feasibility of two-photon absorption using a ruby laser in $\text{CaF}_2:\text{Eu}^{2+}$. They showed that the simultaneous absorption of two red ruby-laser photons by europium impurities in CaF_2 crystals leads to blue fluorescence that could only be populated by two-photon absorption. Almost simultaneously Kleinman³ in 1962 estimated the strength of this process in a theoretical paper. Subsequently the absorption of two fixed laser photons was shown to lead to photoelectric emission, chemical reactions, colour centre production and photoconductivity⁴. Since the advent of lasers, two-photon spectroscopy has emerged as a novel spectroscopic technique⁵. Its importance lies in the fact that one can observe transitions which are forbidden in conventional one-photon spectroscopy. With the development of techniques for generating

picosecond optical pulses⁶, it became important to have means of measuring the properties of very short pulses. Two-photon fluorescence display provides a simple and direct but still quantitative method for studying picosecond pulses⁷⁻⁹. It has been pointed out that two-photon absorption will change the coherence of a transmitted light beam¹⁰. This idea is made use of in the case of nonlinear absorbers which act as power limiting elements inside laser cavities.

As is typical of a new phenomenon, after the initial flurry of experiments on the phenomenon itself with well-understood atomic systems and on the development of different techniques, the field has been invaded by molecular scientists who are exploiting this powerful technique in a systematic way to obtain new information on the energy states of a variety of molecules. This technique is rapidly developing¹¹⁻¹⁵ particularly with regard to spectral investigations of organic compounds in solutions. A recent review lists over hundred molecules whose two-photon spectra had been measured upto 1979¹⁶.

Two different methods are used at present to obtain two-photon spectra. The first method is based on

the direct measurement of the amount of light absorbed due to two-photon absorption¹⁷. But, this method is not very sensitive and necessitates the use of sophisticated apparatus because of the small two-photon absorption cross section. The second method is more sensitive and attractive and is more commonly used with fluorescing compounds at present¹⁸⁻²⁵. The source of light generally used for these studies is a dye laser pumped by a nitrogen laser or harmonics of a Q-switched solid-state laser such as ruby or neodymium. The laser-induced fluorescence recorded as a function of the excitation wavelength gives the two-photon spectra. This method is very sensitive because it is easy to detect fluorescence emission even when the intensity is low. Also, highly resolved spectra may be obtained since the spectral bandwidth of dye laser emission is very narrow ($10^{-3} \text{ \AA}^\circ$).

However, dye lasers have the following limitations in these studies. (1) The spectral emission is in practice limited to wavelengths smaller than 850 nm and consequently it is not possible to investigate large molecules absorbing at wavelengths longer than 425 nm. (2) The pulse duration of the excitation source is usually long (3-30 ns) compared to the lifetime of the fluorescent state which results in spurious contributions in the detected fluorescence. Therefore,

a light excitation source of shorter duration and emitting at wavelengths longer than 850 nm is more suitable for these studies.

In this chapter, the two-photon excited fluorescence spectra of rhodamine 6G in methanol for five different concentrations have been discussed. A dye Q-switched Nd:glass laser emitting 25 ns (FWHM) pulses at 1060 nm was used for the experiment. This wavelength matches well with the two-photon absorption in rhodamine 6G. For a comparative analysis, one-photon fluorescence in rhodamine 6G excited by a pulsed nitrogen laser is also given.

5.20 Absorption cross section

Transition probabilities for an atom or molecule subjected to the electric field of a light wave can be calculated using time dependent perturbation theory. One-photon transition probabilities are treated by a first-order perturbation theory which neglects all but direct transition between the two states. Two-photon transition probabilities makes use of the second order perturbation theory, recognising that there are small coefficients for other states even off resonance, and allowing transitions involving these small coefficients of intermediate states²⁶.

A convenient measure of the transition intensity in a molecule is the absorption cross section which is defined such that the change in intensity dI , of a light beam passing through a thin section of sample of length dx is given by

$$-dI = \sigma I N dx \quad (5.1)$$

where N = number of molecules per unit volume and σ is the molecular cross section at the frequency of the beam ($\text{cm}^2/\text{molecule}$). I is expressed in units of photons per unit area per second and the number of molecules excited per second in the thin section of the sample per unit area will be $-dI$. The quantity which can be easily calculated from a knowledge of molecular wavefunctions is not σ itself but the integrated intensity over a band. Therefore, one-photon absorption in the case of polarised light can be determined by the relation

$$\int \sigma d\bar{\nu} = (2\pi^2\bar{\nu}/hc\epsilon_0) \left| \vec{e} \cdot \vec{\mu}_{ul} \right|^2 \quad (5.2)$$

where $\bar{\nu}$ is the transition wave number, ϵ_0 is the vacuum permittivity, \vec{e} is a unit vector defining the direction of polarisation of the electric vector of the light wave and $\vec{\mu}_{ul}$ is the matrix element of the electric dipole moment between

the upper and lower states.

$$\vec{\mu}_{ul} = \int \psi_u^* \mu \psi_l d\tau \quad (5.3)$$

If the molecules are randomly oriented as in gas or solution (5.2) must be averaged over molecular orientation.

In the case of two-photon absorption from a laser beam, the transition probability is proportional to the square of the light intensity, and we have

$$-dI = \delta I^2 N dx \quad (5.4)$$

where δ = molecular two-photon cross section which can be taken as σ/I and is expressed in $\text{cm}^4 \text{ s/photon/molecule}$. Here, the number of molecules excited per unit area per second is $-dI/2$ since two photons are absorbed per molecule excited. In this case the integrated intensity over a band is

$$\int \delta d\tau = \frac{\pi^2 \bar{\nu}^2}{\epsilon_0^2 c} \left| \sum_i \frac{(\vec{e} \cdot \vec{\mu}_{ui})(\vec{\mu}_{il} \cdot \vec{e})}{E_i - E_l - hc\bar{\nu}} \right|^2 \quad (5.5)$$

To calculate one-photon cross section by equation (5.2), it is only necessary to know the wavefunctions of the initial and final states so as to calculate the transition moment by

equation (5.3). However, to calculate two-photon cross sections by equation (5.5), it is necessary to have the wavefunctions of many excited states of the molecule in order to calculate all the transition moments in the sum.

The difference in selection rules between one-photon and two-photon spectroscopy is clear by comparing equations (5.2) and (5.5). The transition moment integral in equation (5.2) will vanish unless the transition density has the same symmetry as one of the coordinate translations. But equation (5.5) contains a product of two such transition moment integrals, and the selection rules are like those for Raman spectroscopy. In the case of a molecule with a centre of symmetry, only transitions from a gerade ground state to ungerade states can be allowed in one photon spectroscopy while only transition to gerade states can be allowed for two-photon transitions. In such molecules, two-photon spectra permits the study of a completely different set of transitions than those easily seen in one-photon spectra.

5.30 Rhodamine 6G

Rhodamine 6G belongs to the xanthene family which exhibits a large number of conjugated double bonds and

delocalized π -electron orbitals. The broad electron delocalization results in large polarizabilities, strong absorption in the visible region and substantial two-photon absorption at both neodymium and ruby frequencies.

A simplified electronic level scheme of rhodamine 6G is shown in fig.5.1. S_1 and S_2 are the lowest excited singlet levels which can be observed on the absorption curve (fig.5.2). The two main peaks in the one-photon spectrum which correspond respectively to twice the neodymium and ruby energy can be interpreted as resulting from the $S_0 \rightarrow S_1$ and $S_0 \rightarrow S_2$ transitions. In the case of two-photon absorption, the first band is less intense than the second band, contrary to the situation for the single-photon absorption spectra. With the exception of this inversion of the maxima of intensity, the two spectra coincide. This may be understood in terms of the more or less symmetry allowed transitions. The rhodamine molecule in the ground state has practically C_{2v} symmetry (quasi-symmetric) (fig.5.3). The S_0 ground state of the π -electron belongs to the totally symmetric representation A_1 . Due to the lack of symmetry of the molecule, the one and two-photon transitions are always allowed, only the relative magnitude of the two transition moments varies with the approximate state symmetry. The two possible classes of

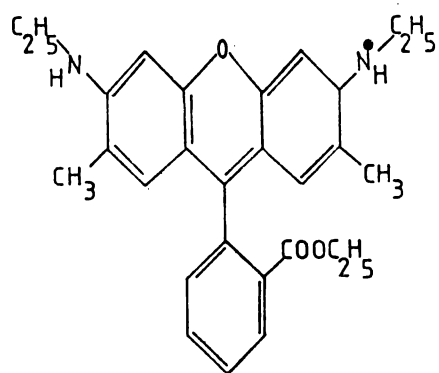


Fig.5.3 Structural formula of rhodamine 6G

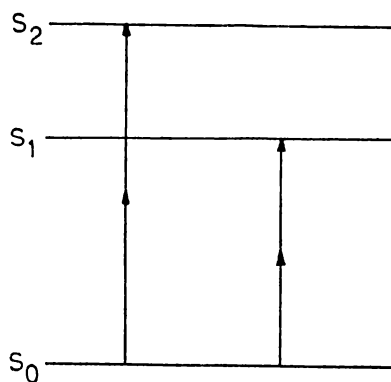


Fig.5.1 Simplified electronic level scheme of rhodamine 6G

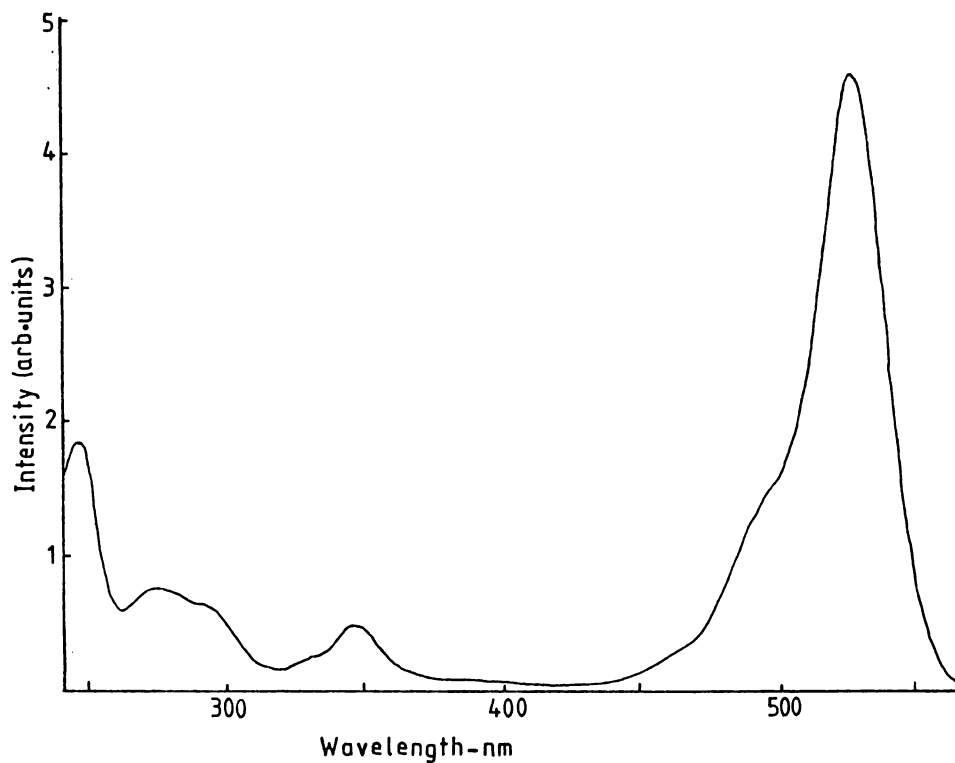


Fig.5.2 Absorption spectrum of rhodamine 6G.

two-photon transitions are both symmetry allowed. Experimental results show that S_1 belongs to B_2 and S_2 to A_1 . When one goes from the $S_0 \rightarrow S_1$ to $S_0 \rightarrow S_2$ transition, a large increase in the two-photon cross section is observed. This can be attributed to two main reasons. Firstly, the $S_0 \rightarrow S_2$ transition occurs between states with the same symmetry and this transition takes full advantage of the π -electron delocalization. Similar considerations show that the situation is reversed for one-photon transition. Secondly, for the $S_0 \rightarrow S_2$ transitions, the contribution of S_1 to the sum over intermediate states is enhanced. This is shown by the continuous increase in δ/σ with frequency. The value of two-photon cross section δ of rhodamine 6G at 690 nm is unusually high. This may be because of the large optical nonlinearities which can be expected in molecules with a large number of conjugate double bonds resulting in broadly delocalized π -orbitals.

5.40 Experimental details

For the present investigations, we used a Nd:glass laser Q-switched by Kodak 14015 dye in 1,2 dichloroethane which gave output pulses of 25 ns (FWHM) at 1060 nm. These pulses were incident on a quartz sample cell, of dimensions 12 mm x 12 mm, which contained the methanol solution of

rhodamine 6G. A portion of the pulse intensity was monitored using a Scientech one inch Disc Calorimeter (Model 38-0101). The power fluctuation in the laser output was not more than $\pm 5\%$ at a constant pump voltage. The average value of the peak power output of the laser was 2 MW at a constant pump voltage of 2.5 kV. The fluorescence emitted from the sample was detected at right angles to the laser beam and was focused by a lens onto the entrance slit of a 0.5 metre Jarrell-Ash Ebert scanning monochromator (Model 82-000) whose slits were adjusted to give a bandwidth resolution of 16 \AA . A photomultiplier (EMI 9683 KQB) detected the fluorescence signal and was recorded on a 100 MHz storage oscilloscope (Tektronix Model 466 DM 44). The schematic diagram of the experimental set up is given in fig.5.4. Scattered light from background sources such as cell windows and other optical components was reduced to tolerable level by this geometry. Experiments were carried out at $22 \pm 1^\circ\text{C}$. The wavelength at the monochromator was altered in steps of 25 \AA each time and the fluorescence output was recorded for a constant input power covering the wavelength region 560 nm to 620 nm. The experiment was repeated for five different concentrations from 1×10^{-4} to 2.5×10^{-2} M and the spectra are presented in fig.5.5.

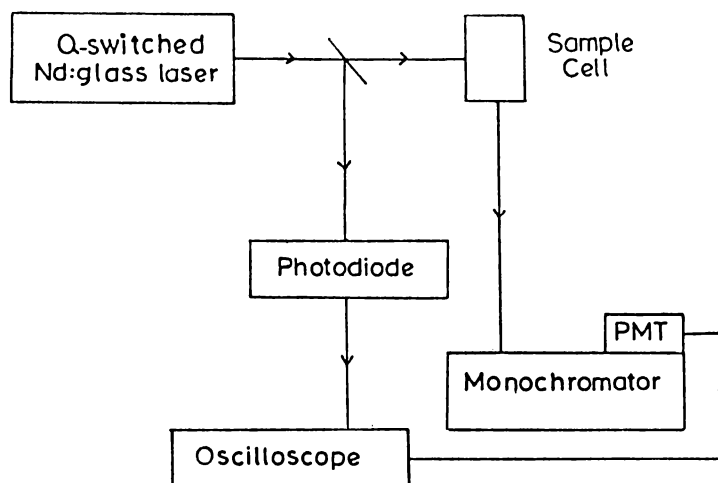


Fig.5.4 Two-photon excited fluorescence-- experimental set-up.

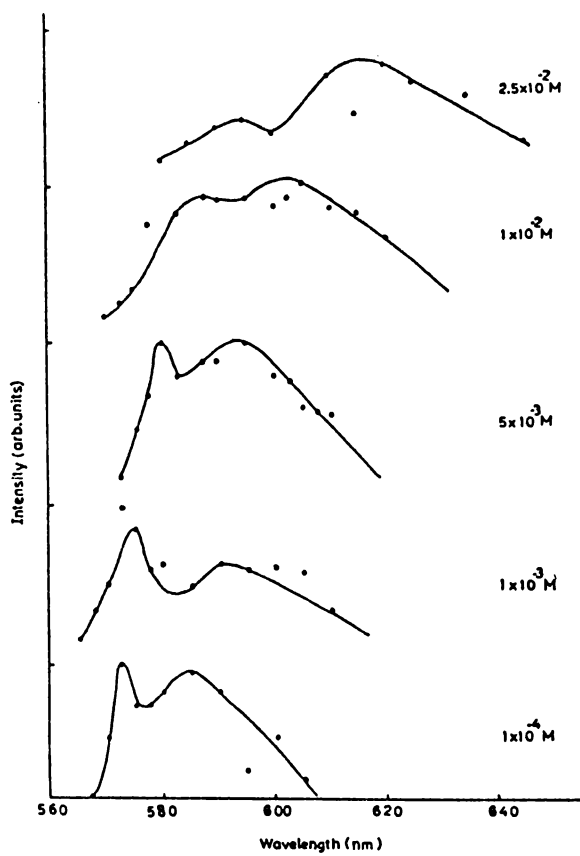


Fig.5.5 Two-photon excited fluorescence spectra.

5.50 One-photon excited fluorescence in rhodamine 6G

One-photon fluorescence spectra of rhodamine 6G were also recorded for comparison. The spectra were recorded at two different concentrations viz., around 10^{-3} M and 10^{-2} M.

For this investigation a nitrogen laser operated at a peak power of about 50 kW which gave output pulses of 10 ns at 3371\AA was used. The fluorescence emitted from the sample was detected at right angles to the laser beam and was focused by a lens onto the entrance slit of a 0.5 metre Jarrell-Ash monochromator. A PMT (EMI 9683 KQB) detected the fluorescence signal and the spectra were recorded using an Omniscribe strip chart recorder (B 5127-11). The experimental set up is as shown in fig.5.6. The slit widths, geometry of experimental set up and the sample cell were the same as those used for the TPE fluorescence experiment. The spectra obtained are given in figs.5.7A and 5.7B.

A spectrum obtained by excluding the front layer fluorescence emission was recorded as follows: The cell side

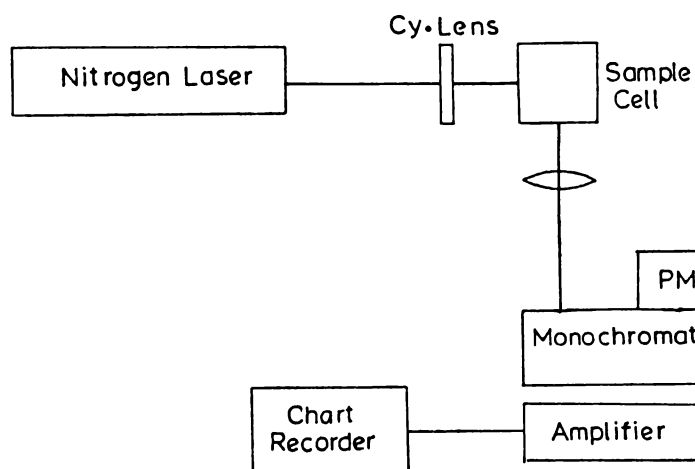


Fig.5.6 One-photon fluorescence-experimental set-up.

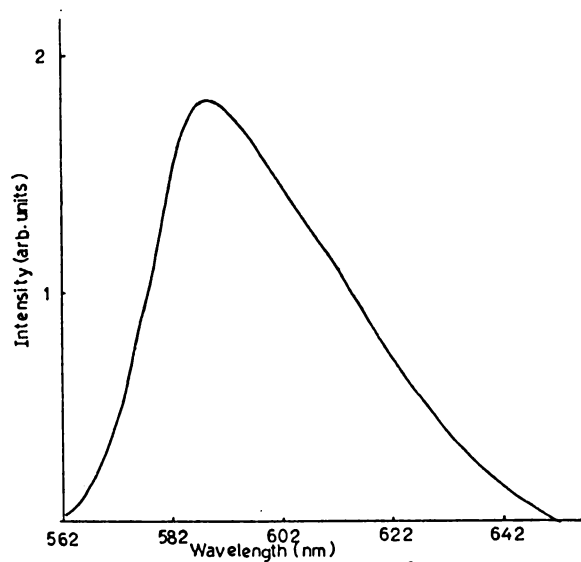


Fig.5.7A One-photon fluorescence spectrum of Rh 6G at a concentration $\sim 10^{-3}$ M.

facing the monochromator had a width of 12 mm of which 3 mm was covered by a strip of black paper so that emission from the front layer could be excluded. The fluorescence emission recorded from the portion of the sample not covered by the black paper is shown in fig.5.7C. Spectra 5.7B and 5.7C were taken at the same concentration. Comparison of figs.5.7B and 5.7C reveals that the shoulder which was observed in fig.5.7B has disappeared from fig.5.7C. This indicates that the shoulder appearing in figs.5.7A and 5.7B is not attributable to any contaminants in the sample or to any instrumental artifacts. Comparison of figs.5.7A and 5.7B shows that the shorter wavelength peak decreases in relative fluorescence intensity with increasing molar concentration which is a clear evidence for re-absorption.

5.60 Results and discussion

The two-photon excited fluorescence spectra exhibit two peaks at all concentrations. As the concentration increases, the spectral peaks are found to shift towards the red and is the usual concentration dependent phenomenon. Variation of the fluorescence with concentration shows two striking characteristics (a) No concentration quenching is observed even at a high concentration of 2.5×10^{-2} M. For a

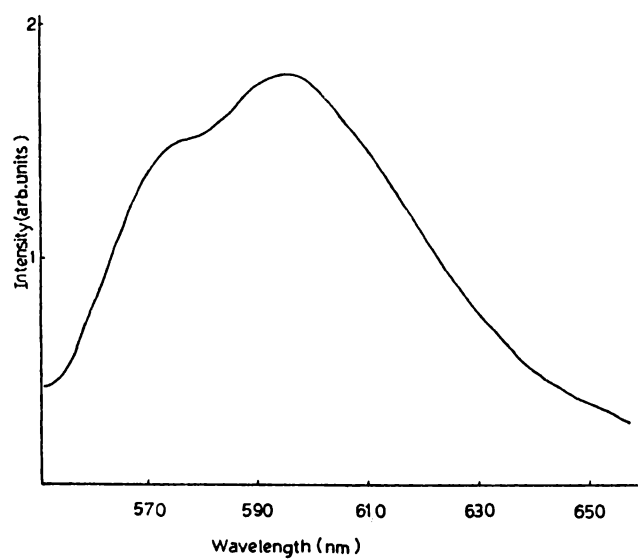


Fig.5.7B One-photon fluorescence spectrum of Rh 6G at a concentration $\sim 10^{-2}$ M.

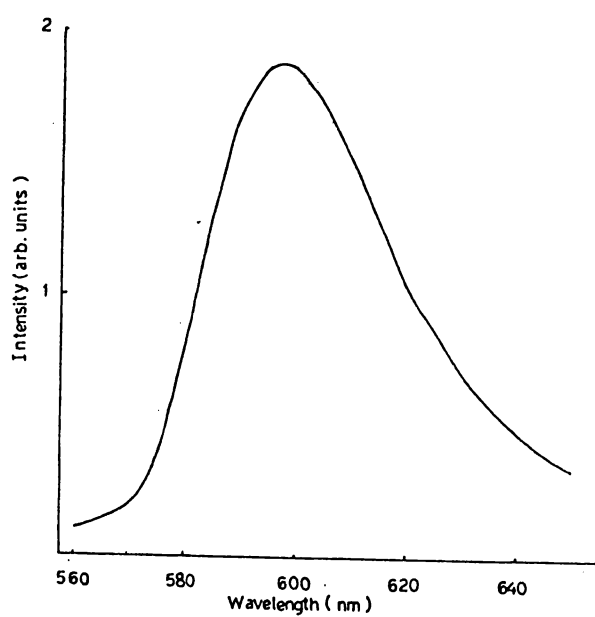


Fig.5.7C One-photon fluorescence spectrum of Rh 6G at a concentration $\sim 10^{-2}$ M excluding front-layer emission.

single photon fluorescence, concentration quenching is expected at this level of concentration²⁷. (b) A graph of one-photon excited fluorescence peak λ_{max} against concentration shows a saturation limit at about $1 \times 10^{-2} \text{M}$ concentration²⁸. But no sign of such saturation is observed even at $2.5 \times 10^{-2} \text{M}$ for the two peaks (fig.5.8).

In order to establish the mechanism of emission, the input laser power was varied and the fluorescence output corresponding to the emission peak was recorded. This was repeated for all concentrations. A log-log plot of laser intensity against fluorescence intensity yielded a straight line of slope two (fig.5.9) except at the two high concentrations. Out of the four possible mechanisms for this fluorescence as suggested by Kobayashi et al²⁴, excitation by the second harmonic is a rare possibility and there is no detectable intensity corresponding to 530 nm. Successive two-step excitation via a lower triplet state is also eliminated by the absence of phosphorescence. This is verified from the absence of time lag between the incident laser pulse and the resulting fluorescence signal as recorded by the oscilloscope. The rate of intersystem crossing from S_1 is very low in xanthene dyes²⁹. Therefore, the delayed fluorescence caused either by triplet singlet crossover or by triplet-triplet

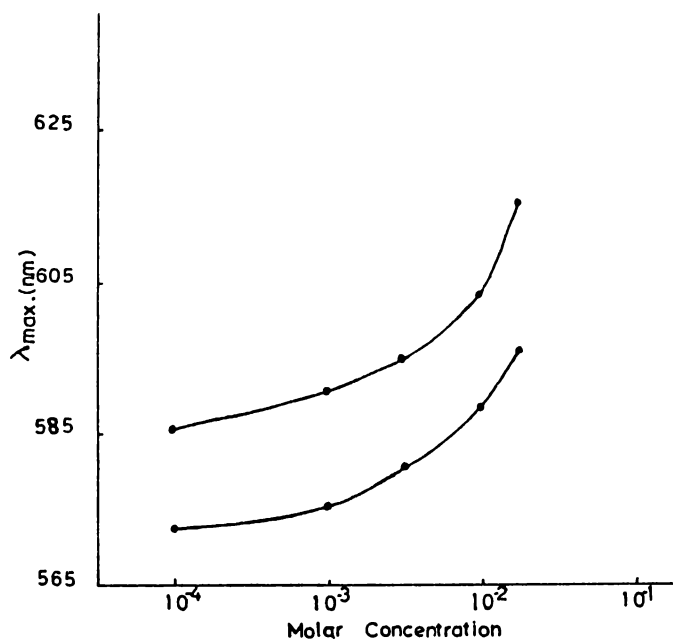


Fig.5.8 Variation of λ_{\max} with concentration

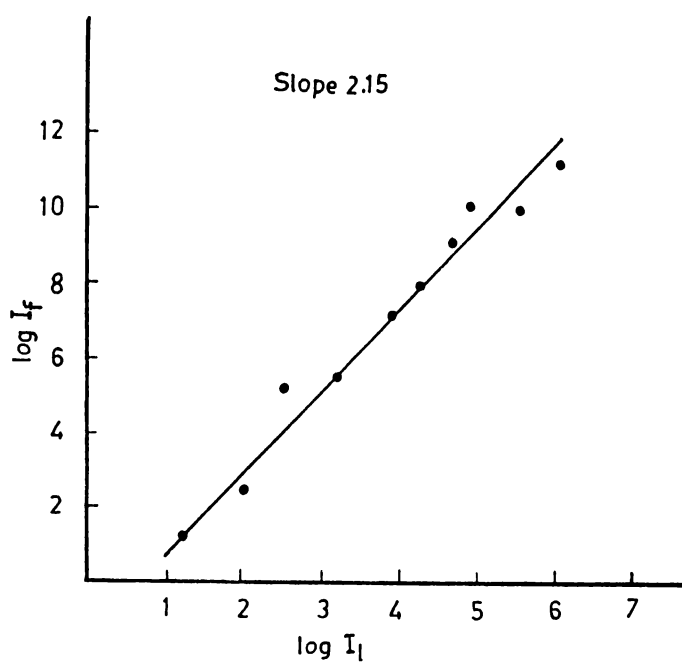


Fig.5.9 Plot of log fluorescence intensity vs. log. incident intensity.

annihilation is a distant possibility. It can therefore be concluded that the fluorescence from rhodamine 6G originates as a result of the excitation to the singlet state S_1 by the simultaneous absorption of two photons corresponding to the laser wavelength of 1060 nm. At higher concentrations, the higher vibrational levels of the lowest singlet state S_0 get populated building increased chances for one-photon excited fluorescence¹⁹ in addition to the TPE fluorescence and this competition brings about reduction in the slope of log-log plot. This gives a concentration limit of $\sim 1 \times 10^{-2}$ M for pure two-photon fluorescence at a peak power of 2 MW.

The two emission peaks observed in TPE spectra cannot be attributed to any contaminants in the sample or instrumental artifacts. This was verified by comparing the two-photon excited fluorescence spectra with the spectra of single photon fluorescence for the same range of concentration. Absence of quenching at higher concentrations and fig.5.8 rule out the formation of complexes like dimer or excimer within the range of concentration studied. Moreover, λ_{\max} shift is very small in the case of emission due to excimer formation³⁰. But the observation of a large shift

in the peak wavelength with concentration also supports the absence of emission due to the formation of excimers. The very low rate of intersystem crossing from S_1 in xanthene dyes sets aside the role of processes involving the triplet state T_1 in explaining the observed peaks. The experimental observation that the shorter wavelength peak decreases in relative fluorescence intensity with increasing molar concentration suggests that the second peak can be attributed to reabsorption within the sample.

REFERENCES

1. M.Goeppert Mayer, *Ann.Physik*, 9, 273 (1931).
2. W.Kaiser and C.G.B.Garrett, *Phys.Rev.Lett.* 7, 229 (1961).
3. D.A.Kleinman, *Phys.Rev.* 125, 87 (1962).
4. H.Mahr, *Quantum electronics*, ed.Herbert Rabin and C.L.Tang, p.285, Academic Press (1975).
5. J.M.Worlock, *Laser handbook*, ed.F.T.Arecchi and E.O.Schulz-Dubois, Vol.2, p.1323, North Holland Pub.Co. (1972).
6. De Maria et al., *Proc.IEEE*, 57, 2 (1969).
7. J.A.Giordmaine et al., *Appl.Phys.Lett.* 11, 216 (1967).
8. P.M.Rentzepis and M.A.Duguay, *Appl.Phys.Lett.* 11, 218 (1967).
9. Klauder et al., *Appl.Phys.Lett.* 13, 174 (1968).
10. Y.R.Shen, *Phys.Rev.* 155, 921 (1967).
11. Claude Rulliere and Philemon Kottis, *Chem.Phys.Lett.* 75, 478 (1980).
12. Monson and McClain, *J.Chem.Phys.* 56, 4817 (1972).
13. J.P.Hermann and J.Ducuing, *Phys.Rev.* A.5, 2557 (1972).
14. P.R.Monson and W.M.McClain, *J.Chem.Phys.* 53, 29 (1970).
15. R.M.Hochstrasser and J.E.Wessel, *Chem.Phys.Lett.* 24, 1 (1974).

16. Friedrich and W.M.McClain, Ann.Rev.Phys.Chem. 31, 559 (1980).
17. A.Penzkofer, W.Falkenstein and W.Kaiser, Appl.Phys.Lett. 28, 319 (1979).
18. F.P.Schafer and W.Schmidt, IEEE J.Quantum Electron. QE-9, 357 (1966).
19. J.P.Hermann and J.Ducuing, Opt.Comm. 6, 101 (1972).
20. R.M.Hochstrasser, H.N.Sung and J.E.Wessel, Chem.Phys.Lett. 24, 7 (1974).
21. N.Mikami and M.Ito, Chem.Phys.Lett. 31, 472 (1975).
22. U.Boesl, H.J.Neusser and E.W.Schlag, Chem.Phys. 15, 167 (1976).
23. T.M.Stachelek, T.A.Pazola, W.M.McClain and R.P.Drucker, J.Chem.Phys. 66, 4540 (1977).
24. T.Kobayashi and S.Nagakura, Chem.Phys.Lett. 13, 217 (1972).
25. H.L.B.Tang, R.J.Thrash and G.E.Luoi, Chem.Phys.Lett. 57, 59 (1978).
26. S.J.Stricklner, Julanna V.Gilbert and J.E.McClanhan, Lasers and applications, ed.H.D.Bist and J.S.Goela, p.351, Tata McGraw-Hill Pub.Co. (1984).
27. K.H.Drexhage, Dye lasers, ed. F.P.Schafer, p.160, Springer-Verlag (1977).

28. P.J.Sebastian and K.Sathianandan, Opt.Comm. 32, 422 (1980).
29. K.H.Drexhage, J.Research of the N.B.S.-A Physics and Chemistry, 80A, 3 (1976).
30. D.M.Friedrich, J.Van Alsten, M.A.Walters and N.L.Schultz, J.Phys.Chem. 85, 1297 (1981).

Chapter 6

PRODUCTION, DETECTION AND CHARACTERISATION OF A LASER-PRODUCED PLASMA

6.10 Introduction

When an intense pulse of light from a laser is focused onto a solid material, a hot plasma is formed. The plasma expands rapidly away from the target surface as its initial thermal energy is converted to directed energy¹. One of the fundamental techniques for measuring the properties of these plasmas is the method of using an electrostatic probe. This technique was developed by Langmuir in 1924 and is consequently referred to as the method of Langmuir probes. Basically the probe is merely a small metallic electrode, usually a wire, inserted into a plasma. The probe is attached to a power supply capable of biasing it at various +ve and -ve voltages relative to the plasma. The current collected by the probe as a function of probe voltage provides information about the conditions in the plasma. These probes, used to diagnose the properties of

stationary and flowing plasmas, have the advantage that they are simple to construct and operate and can give time resolved measurements of local plasma properties without greatly disturbing the plasma^{2,3}. Under a wide range of conditions, the disturbance caused by the presence of the probe is localized and its very presence has no effect on the quantities it is measuring. While almost all other diagnostic techniques give information averaged over a large volume of plasma, this method has the relative advantage that it can make local measurements.

Experimentally, electrostatic probes are extremely simple devices. But, "nature, however, makes us pay a penalty for this simplicity: the theory of probes is extremely complicated". The difficulty stems from the fact that probes are boundaries to a plasma, and near the boundary the equations governing the motion of the plasma change their character. In particular, the condition of quasi-neutrality which exists in the body of the plasma is not valid near a boundary; and a layer called a sheath can form, in which ion and electron densities can differ and hence large electric field can be sustained⁴. Probe theories, depending upon the nature and parameters of the plasma,

relate the measured value of the probe current to the plasma density, electron temperature, floating and plasma potentials and oscillations⁵⁻⁸. The shape and size of the probe depend upon the plasma parameters and the quantity to be determined. Various investigations of laser-produced plasma by cylindrical and plane probes have been reported⁹⁻¹².

Spectroscopic techniques can also be used to characterise the plasma^{13,14}. An attempt was made in this direction and was subsequently abandoned as the emission intensity from the plasma was too weak to produce any appreciable effect on the photographic film used. Therefore, in the present investigations, a carbon plasma produced by the Q-switched Nd:glass laser was analysed using the Langmuir probe technique. The purpose of the experimentation was to study the nature of variation of the flow velocity as a function of the input laser energy and to get an approximate idea of the electron density.

6.20 Fabrication of a plasma chamber

The chamber used for the production of plasma is fabricated from a seamless steel tube of outer diameter 26.5 cm and thickness 1 cm. This chamber is plated with nickel.

In order to produce and detect the plasma from any angle, symmetrically placed eight windows (each of 4 cm diameter) are cut out from the sides of the chamber. These sides are vacuum-sealed with the help of O-rings, glass plates and metallic flanges (7 cm x 7 cm). One window is used for focusing and another for introducing the probe which is used to detect the plasma. The focusing system which can slide within the vacuum across an O-ring carries a short focal length biconvex lens (focal length = 4 cm) on one end and the other end has a quartz window. This system can focus the laser beam onto the target. The top portion of the chamber with an O-ring seat is vacuum-sealed by a $\frac{1}{2}$ inch thick metallic disc with an eccentric 5.5 cm diameter hole. The metallic support that holds the target can slide through this hole across an O-ring. The bottom portion of the chamber presses against a 1.75 cm thick chromium plated mild steel disc with the help of an O-ring. This disc (34.5 cm diameter) has a 9 cm diameter hole at its centre and is firmly seated on the top of the diffusion pump.

6.30 Fabrication of a vacuum system

The chamber within which plasma is to be created must be evacuated to a pressure of less than 10^{-5} torr. This was achieved using a rotary-diffusion combination. Using

the rotary pump with a displacement rate of 200 litre/minute, a vacuum $\sim 10^{-2}$ torr was achieved. Then, for further evacuation to a level better than 10^{-5} torr, a 4 inch diffusion pump was coupled onto this rotary pump. The plasma chamber to be evacuated is placed on the top of this vacuum system. Using a thermocouple gauge the backing pressure was measured. The vacuum within the chamber was measured using a penning gauge. The gauge heads are connected to a pressure indicator which can record both the backing pressure as well as the pressure within the chamber.

6.40 Plasma production and detection

The electrical circuit to detect the laser-produced plasma is as shown in fig.6.1. A copper wire 1 cm long and 2 mm diameter mounted at the centre of a BNC connector is attached to one side of the plasma chamber. The probe was mounted onto the window such that its direction is normal to the direction of the expanding plasma plume. The copper probe is connected to the circuit placed external to the chamber. Various +ve and -ve voltages to the probe can be given using a stabilised power supply. The voltage developing across the 50 ohm resistance is fed onto a 100 MHz storage oscilloscope (Tektronix 466 DM 44).

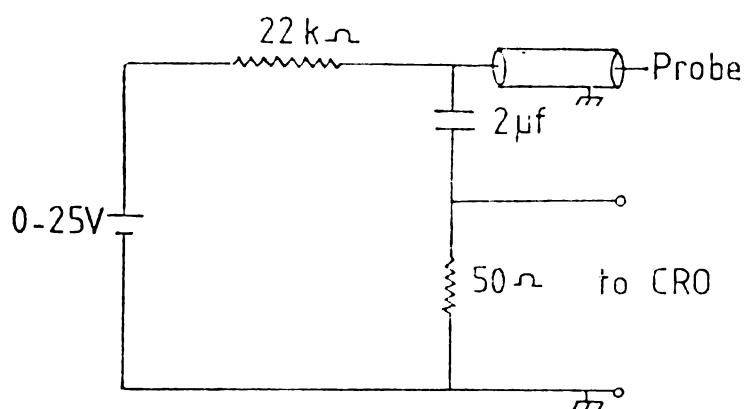


Fig.6.1 Electrical circuit to detect the plasma.

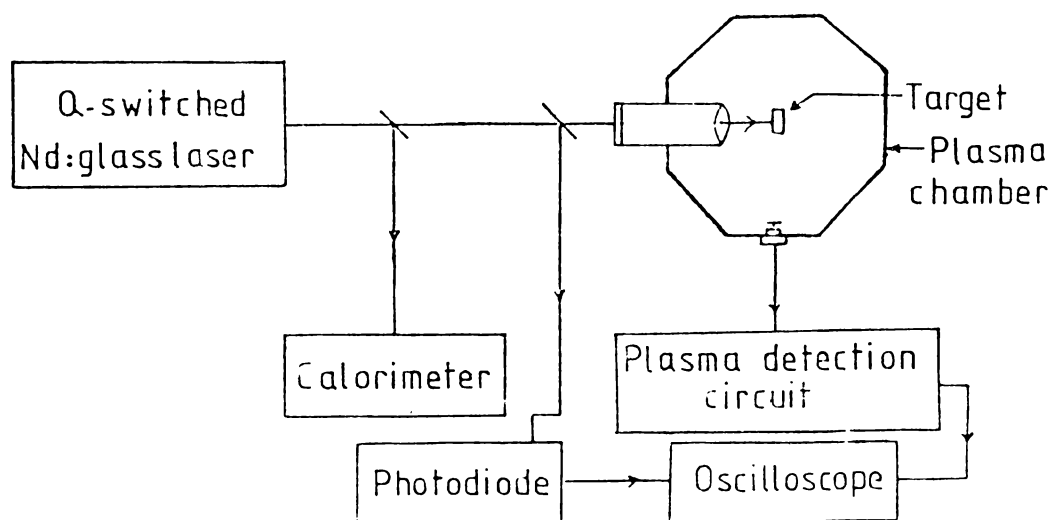


Fig.6.2A Schematic diagram for the plasma experiment.

Two types of investigations were carried out and the experimental layout for these studies are shown in fig.6.2. In the first part of the experimentation, a fixed biasing voltage of +50 V was given to the probe. The plasma chamber is evacuated to a vacuum better than 2×10^{-5} torr. The laser is now fired and focused onto a carbon target (6 mm diameter and 5 mm thick). This results in an expanding plasma. When signals are detected by the probe, the capacitor discharges. The electron current (voltage drop over 50 ohm) drawn by the probe as a function of time is given in fig.6.3. A portion of the laser output intensity was used to trigger the oscilloscope with the help of a photodiode (hp2-4207). Since the firing of the laser initiates the recording of the probe signals, from a knowledge of the time of arrival of the main peak observed and the distance of the probe from the target, one can calculate the flow velocity. As the laser input energy was increased, the time of arrival of the main peak keeps on decreasing, showing that the flow velocity increases. The maximum flow velocity recorded in the experimentation was about 10^7 cm/sec. A graph is drawn with laser input energy vs. flow velocity and is shown in fig.6.4.

In the second part of the experimentation, the laser energy was kept constant and the bias voltage given to

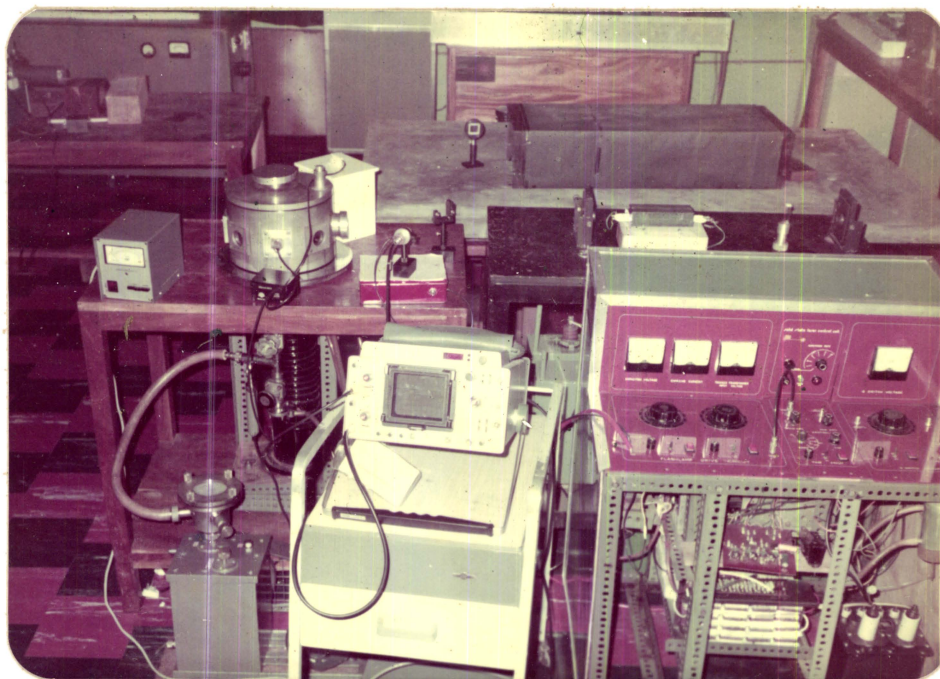


Fig.6.2B Experimental layout for the plasma experiment.

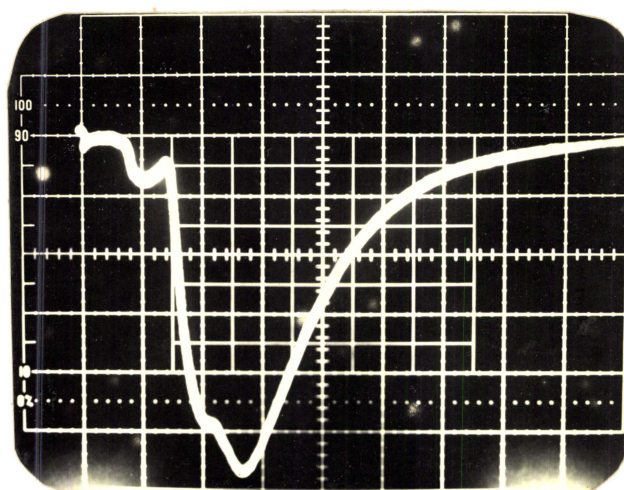


Fig.6.3 Current collected by the probe as a function of time.
Sweep speed: 1 $\mu\text{s}/\text{div}$. Gain: 0.5 V/div.

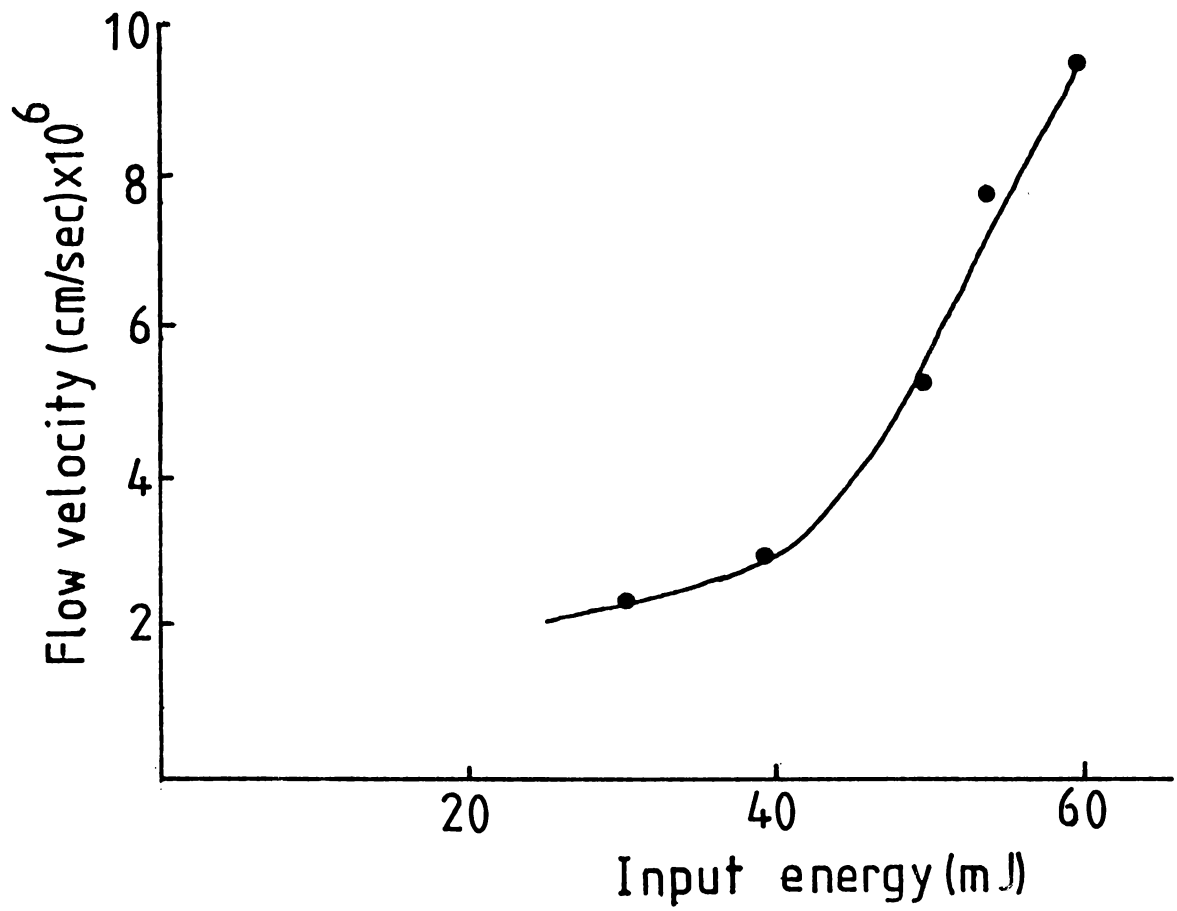


Fig.6.4 Plot of input laser energy vs. flow velocity.

the probe was varied from -25 V to +25 V at intervals of 5 V. It is observed that during the -ve voltages, the current remains more or less constant whereas for +ve voltages the current increases steadily and is shown in fig.6.5.

6.50 Results

The prominent peak observed in fig.6.3 is due to the main plasma produced by the laser-target interaction. An attempt was made to determine the properties and parameters of the main plasma such as flow velocity, probe characteristics, plasma density and electron temperature.

If the distance between the probe and the target is D , the flow velocity U at a particular instant of time t is given by the relation

$$U = D/t \quad (6.1)$$

Variation of flow velocity with laser energy as shown in fig.6.4 is not linear. This is not in agreement with earlier reports^{1,15}. The maximum flow velocity recorded in the present investigation is about 10^7 cm/sec.

Fig.6.5 gives the probe characteristics. The current collected by the probe for higher -ve voltages remains more or less constant at 0.36 mA. This value has been taken as the ion saturation current (I_i). The plasma density was evaluated from the ion saturation current I_i , assuming $\frac{1}{2}m_i U^2 \gg kT_e \gg T_i$, by means of the relation¹

$$I_i = en_e UA \quad (6.2)$$

where e is the electronic charge, A is the probe area, m_i is the average ion mass, T_i is the ion temperature and k is the Boltzmann constant. Using the above relation, the plasma density was calculated and it was found to be $\sim 10^{10} \text{ cm}^{-3}$ for the range of energies studied.

An attempt was made to evaluate the electron temperature using the probe characteristics. But the value obtained was found to differ by an order of magnitude from values reported by earlier workers^{1,16} and therefore has not been presented. Detailed investigations are necessary to establish the value of electron temperature accurately.

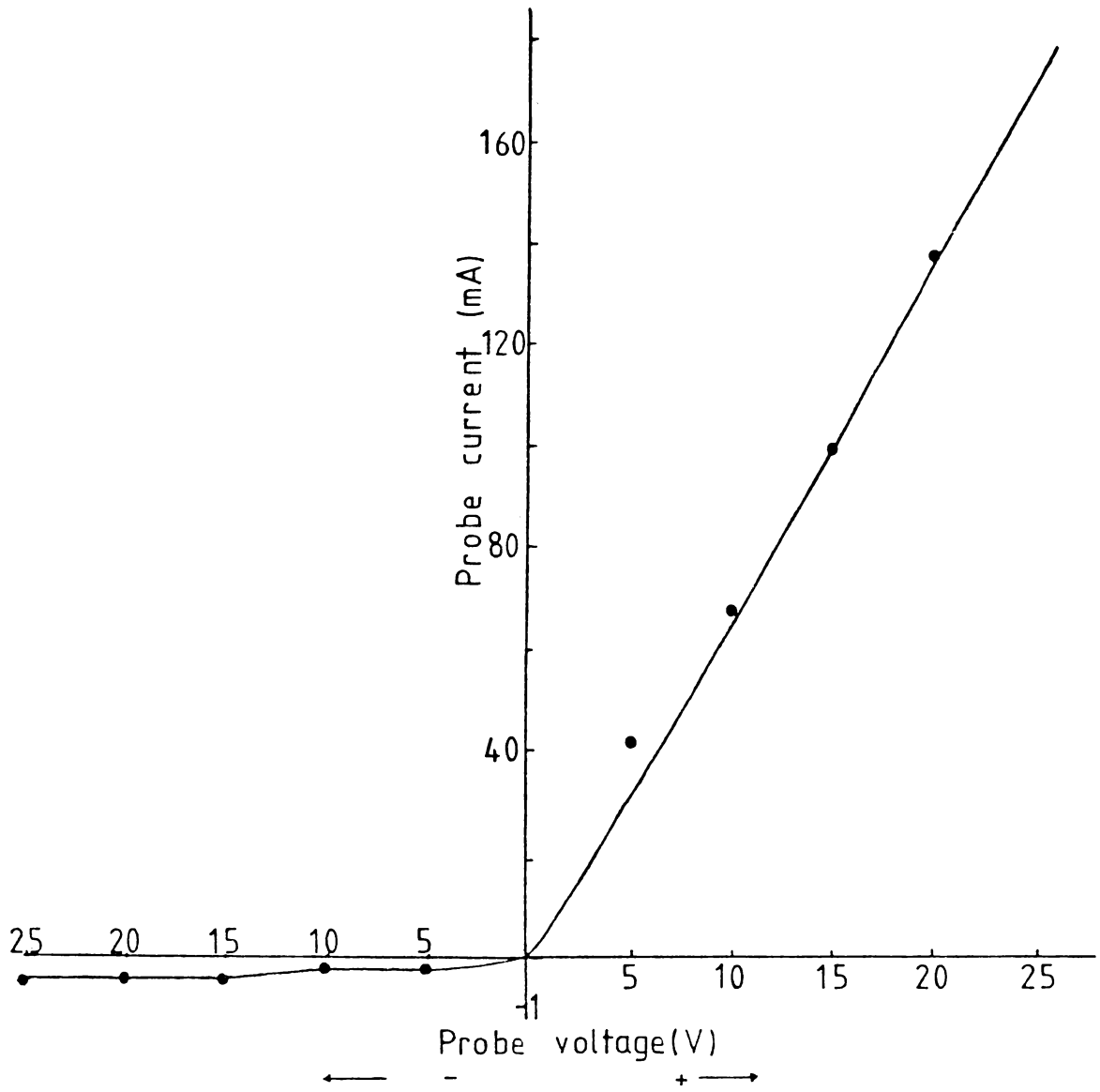


Fig.6.5 Probe characteristics.

REFERENCES

1. C.T.Chang, M.Hashmi and H.C.Pant, Plasma Physics, 19, 1129 (1977).
2. Langmuir, Phys.Rev. 22, 347 (1923).
3. Langmuir, Phys.Rev. 23, 49 (1924).
4. F.F.Chen, Plasma diagnostic techniques, ed. R.H.Huddlestone and S.L.Leonard, p.113, Academic Press (1965).
5. L.Schott, Plasma diagnostics, ed. W.Lochte-Holtgreven, p.668, North Holland (1968).
6. R.L.F.Boyd, Plasma diagnostics, ed. Lochte-Holtgreven, p.732, North Holland (1968).
7. J.D.Swift and M.J.R.Schwar, Electric probes for plasma diagnostics, Iliffe Books (1970).
8. P.M.Chung, L.Talbot and K.J.Touryan, Stationary and flowing plasmas : Theory and application, Springer-Verlag (1969).
9. S.B.Segall and D.W.Koopman, Physics Fluids, 16, 1149 (1973).
10. P.T.Rumsby and J.W.M.Paul, Plasma Physics, 16, 247 (1974).
11. D.W.Koopman, Physics Fluids, 19, 670 (1970).

12. C.T.Chang and M.Hashmi, Physics Fluids, 20, 533 (1977).
13. U.Carretta and U.Tartari, Lettere al Nuovo Cimento, 10, 615 (1974).
14. B.C.Boland, F.E.Irons and R.W.P.Mc Whirter, J.Phys.B: Atom.Molec.Phys.1, 1180 (1968).
15. J.N.Olsen, E.D.Jones and G.W.Gobeli, J.Appl.Phys. 43, 3991 (1972).

Chapter 7

CONCLUSIONS

This chapter presents the conclusions derived from the investigations carried out using the dye Q-switched multimode Nd:glass laser operating at 1062 nm emitting 25 ns (FWHM) pulses. As already pointed out, the main emphasis had been on damage threshold studies of thin films. Two-photon excited fluorescence in rhodamine 6G and plasma studies also figure in the following analysis. The adaptability and suitability of the laser system for the present investigations have been brought forth. Even though the system had the above features, all the experiments have been carried out using the laser in the dye Q-switched mode because of its extreme simplicity in operation and its high peak power output.

The only practical method to determine the most appropriate model of damage in dielectrics is to examine the predictive ability in describing the variation of damage with easily controlled experimental or material variables such as laser pulse width, wavelength and film

properties. But in the present experimental set-up, wavelength and pulse width were maintained constant. Analysis of damage has been mainly carried out as a function of the film properties such as refractive index, absorption and thickness. An inverse dependence on absorption and film thickness observed for SPD and rf sputtered films in the present investigation gives firm support to the impurity dominated damage model. In the case of damage to transparent polymers the viscoelastic properties play a dominant role.

The comparative analysis of the damage threshold measurements carried out in transparent-conductive coatings have established that spray pyrolysis deposited tin oxide films are also equally good competitors with rf sputtered indium tin oxide films and chemical vapour deposited tin oxide films in high power laser systems as electrodes for electro-optic shutters. Moreover, the uniformity of the films have been found to be very good. Spray pyrolysis technique offers the added advantage of greater flexibility in terms of their electrical and optical characteristics depending on the deposition parameters which in turn depends on damage threshold. This permits the investigator to deposit these films as per his application requirements.

Films of high or low damage threshold can be deposited by suitable trade-off between the various characteristic parameters of the film.

A noteworthy feature of this thesis is the identification of polyacrylonitrile (PAN) films of high damage threshold (26 J/cm^2) with very low-level absorption at 1060 nm. Another interesting feature associated with these films is that the damage threshold of these films increases with increase in thickness unlike in the case of dielectrics. This makes these films, especially those of higher thicknesses, very good candidates for high energy laser applications and may replace the dielectric films in high energy applications. These features are attributed to the viscoelastic properties of the surface layer of the polymer material and to the molecular characteristic of the monomer.

Various types of attempts are being made to increase the threshold of AR coatings since they are the weakest link in any high power laser system. In the present investigation the threshold of a half-wave layer of MgF_2 film has been shown to increase by about 50% when PAN film having

a high threshold was given as an undercoat. The result obtained has been attributed either to the change in the chemical environment or to better adhesion of the MgF_2 films on PAN.

In the case of investigation on MgF_2 films, the threshold is shown to decrease with film thickness as reported by earlier workers. Low damage threshold obtained in the case of gold films has been explained in terms of the low yield stress of the material and its high absorptance at 1060 nm. Gold coating with an undercoat of PAN does not show any variation in the damage threshold value which is attributed to the poor adhesion of gold on PAN.

Another important result that has emerged out of the present investigations is the determination of the concentration limit of two-photon excited fluorescence in rhodamine 6G. Results obtained in the case of two-photon excited fluorescence have been confirmed as due to re-absorption by a comparative study made with one photon excited fluorescence.

Laser-produced plasma studies carried out on carbon give the important properties and parameters of the

- G 3511 -

171

plasma. The electron density has been evaluated to be around 10^{10} cm^{-3} and the maximum flow velocity recorded is $\sim 10^7 \text{ cm/sec}$.

